Title
Heat Conduction in Complicated Nanostructures: Experiments and Theory

Author
Wehmeyer, Geoff Paul

Publication Date
2018

Peer reviewed|Thesis/dissertation

Heat Conduction in Complicated Nanostructures: Experiments and Theory

By

Geoffrey Wehmeyer

A dissertation submitted in partial satisfaction of the

requirements for the degree of

Doctor of Philosophy

in

Engineering – Mechanical Engineering

in the

Graduate Division

of the

University of California, Berkeley

Committee in charge:

Professor Christopher Dames, Chair
Professor Costas Grigoropoulos
Professor Andrew Minor

Summer 2018

Heat Conduction in Complicated Nanostructures: Experiments and Theory

By Geoffrey Wehmeyer

Abstract

Heat Conduction in Complicated Nanostructures: Experiments and Theory

by

Geoffrey Wehmeyer

Doctor of Philosophy in Engineering – Mechanical Engineering

University of California, Berkeley

Professor Christopher Dames, Chair

The thermal conductivity (k) of a semiconducting nanostructure is dramatically reduced from the bulk value due to boundary and interfacial scattering of energy carriers (phonons). The theoretical understanding of such nanoscale thermal phenomena is based on measurements of relatively simple nanostructures, such as thin films or nanowires. However, qualitatively new heat transfer mechanisms may emerge in more complicated nanostructures such as etched silicon nanomeshes or arbitrarily anisotropic thin films. New theoretical tools are needed to predict k of these nanostructures, and new experimental nanoscale temperature mapping tools would resolve questions about the dominant nanoscale mechanisms. In addition, nanothermometry techniques could be used to improve the thermal performance of technologies utilizing complicated nanostructures, which range from data storage devices to light-emitting diodes and microelectronics.

In this dissertation, I develop experimental, computational, and analytical tools to answer fundamental questions about heat transfer in complicated nanostructures. I begin by demonstrating two nanothermometry techniques in the scanning transmission electron microscope (STEM) utilizing temperature-dependent thermal diffuse scattering. Temperature mapping of a Joule-heated silicon carbide device in the STEM shows the path forward towards ultrahigh spatial resolution temperature mapping of complicated nanostructures. Then, I describe how phonon ray tracing simulations quantify the boundary scattering reduction of k in complicated nanostructures. Comparing these simulation results with collaborator's k measurements reveals that thermal phonons behave like incoherent particles rather than like coherent waves in silicon nanomeshes, which are membranes with periodically etched holes. Lastly, I derive solutions of the Boltzmann transport equation for phonon transport in arbitrarily aligned anisotropic thin films, and use these solutions to extend a well-known bulk Onsager relation for anisotropic heat conduction into the boundary scattering regime. In summary, further research using these experimental and theoretical techniques can answer long-standing fundamental thermal questions and can be leveraged in the design of energy-efficient lighting technologies and improved data storage devices.

Dedicated to my parents and to Lauren.

Table of Contents

List of Figures

Acknowledgements

I have been very fortunate to be surrounded by caring, intelligent, and motivated individuals in my life. These acknowledgements can only hint at the thanks that are owed to so many.

My five years at Berkeley have been a rewarding experience, full of intellectual and personal growth. I am thankful for the funding support which allowed me to pursue my studies here and to take advantage of the opportunities on campus.

I am grateful to the many teachers and professors who have challenged and encouraged me. I would particularly like to thank Helen Hardgree for all of her work at Oxford and BVNW. At UT Austin, Carlos Hidrovo inspired me in the classroom and got me hooked on research in the lab. Many thanks go to him and my MTFL labmates, especially Collier Miers, Arnav Chhabra, and Brian Carroll. I am also grateful to Ofodike Ezekoye, Philip Schmidt, and Alan McGaughey for their guidance, enthusiasm, and support when I was at Texas.

I have benefited tremendously from collaborations at Berkeley. Particular thanks go to Karen Bustillo, Junqiao Wu, Hwan Sung Choe, Jaeho Lee, Woochul Lee, and Will Chang. Their hard work and encouragement kept research exciting and fresh for me. I would also like to thank my qualifying exam committee: Costas Grigoropoulos, Van Carey, Andrew Minor, and Mary Scott.

Many thanks go to my labmates at Berkeley: Zhen Chen, Peter (Fan) Yang, Sean Lubner, Imran Khan, Christian Monachon, Vivek Mishra, Wyatt Hodges, Jake Kilbane, Xiaodong Zhao, Mitch Westwood, Menglong Hao, Andrea Pickel, Josh Wilbur, Tomohide Yabuki, Jason Wu, Daniel Hsieh, Chenhan Liu, and Pengyu Yuan. I have learned more than I can say from this remarkable collection of engineers, scientists, and friends. I would also like to thank all of the SEED volunteers, and my good friends Quentin Smith, Adam Phillips, and Julien Caubel.

I can't imagine having a better Ph.D. advisor than Chris Dames. Chris' scientific creativity, hard work, and genuine care for his students and colleagues has made my five years in the lab a great experience. Chris has been a true mentor and advocate for me, and I hope to emulate his example in the future.

My parents, brother, and family have encouraged, supported, and loved me at every stage of my life. I love and appreciate them very much.

Finally, to Lauren, who makes my life brighter every day. I'm so glad we are on this journey together.

Chapter 1 : Complex thermal nanostructures

The fundamental equation of macroscopic heat conduction in isotropic solids is Fourier's law, $q" = -k\nabla T$. Fourier's law states that the magnitude of the heat flux vector $q"$ is linearly proportional to the magnitude of the temperature gradient ∇T, and introduces the thermal conductivity k as the material-dependent constant of proportionality. Like all *macroscopic* transport properties, k is intimately related to the *atomic* and *microscopic* structure of the material. Heat conduction research aims to understand this connection between the atomic, microscopic, and macroscopic length scales, and to use this knowledge to design materials with desirable thermal properties. One of the best ways to investigate the link between length scales is to measure how k changes when the characteristic size of the material is reduced down to the nanoscale. Understanding why the thermal properties of nanostructures differ from the bulk provides new insight into the fundamental mechanisms of heat transport, and leads to new opportunities in the design of thermal systems. Moreover, the ability to accurately predict and measure heat transfer rates in nanostructured systems is of critical importance in the performance of electronic and optoelectronic devices, new lighting and data storage technologies, and energy conversion systems.

This dissertation is concerned with heat conduction in complicated nanostructures. In this context, "complicated" refers to a nanoscale thermal system which has an irregular geometry, consists of heterogeneous materials, or displays strongly anisotropic properties. In this introductory chapter, I will describe the scientific and technological motivation for studying heat transfer in these complicated nanostructures, and illustrate the need for new experimental, numerical, and analytical techniques to deal with the enhanced complexity. We begin by reviewing thermal transport in bulk materials.

1.1 Thermal conductivity of macroscopic materials

The results of thermal conductivity measurements are often interpreted using a theoretical framework known as the Boltzmann Transport Equation (BTE) [1]. The BTE formalism, which is similar to the classic kinetic theory of gases[2], treats the fundamental microscopic energy carriers as individual particles transporting the heat via random motion. In metals, free electrons carry the heat; in semiconductors and dielectrics, the heat is predominantly carried by phonons, which are the quanta of atomic vibrations. We will primarily focus on phonon-dominated k in this dissertation, since many nanostructures of experimental interest are semiconductors.

The simplest BTE prediction for k of a bulk, homogeneous, isotropic material is

$$k = \frac{1}{3} \mathrm{Cv}\Lambda. \qquad (1)$$

Here, C is the specific heat per unit volume, v is the velocity of energy propagation (known in wave mechanics as the group velocity), and Λ is the mean free path, which is related to the average distance between scattering events. Eq. (1) is rarely

quantitatively accurate for real materials because the derivation assumes that phonons of different energies have the same group velocity and undergo the same scattering, which is typically untrue [3]. In addition, even thermally isotropic materials such as silicon do not possess true acoustic isotropy, where the phonons travel with the same speeds in all directions. If we wish to relax these assumptions, we can consider the most general case of anisotropic bulk materials, in which Fourier's law generalizes to $q"_\alpha = -k_{\alpha\beta}(\nabla T)_\beta$. Here, $k_{\alpha\beta}$ is the component of the thermal conductivity tensor that relates the heat flux in the α direction $q"_\alpha$ to the temperature gradient in the β direction $(\nabla T)_\beta$. The BTE prediction for this complicated scenario is $k_{\alpha\beta} = \sum_j \mathrm{C_j}\, \mathrm{v_{j,\alpha}} \Lambda_{\mathrm{j},\beta}$, where the index j labels the phonon mode, $\mathrm{C_j}$, $\mathrm{v_j}$, and Λ_j are all mode-specific quantities, and the subscript α or β indicates a projection of a vector along that particular direction.

Overall, however, Eq. (1) remains the most conceptually useful result of the BTE theory because it concisely demonstrates how the bulk thermal conductivity is related to the atomic properties of the material. Calculating C and v requires knowledge of the phonon dispersion relation, which relates the phonon's energy to its wavelength. This phonon dispersion relation is characteristic of the atomic bonding and configuration. In the idealized scenario of an impurity-free infinite crystal, phonon-phonon scattering dominates Λ. This phonon-phonon scattering is also essentially an atomic property; however, impurity atoms, dislocations, or grain boundaries can also scatter phonons, meaning that Λ and therefore k can be reduced below the idealized values due to this microstructure-dependent scattering. Crucially, nanostructuring can also reduce Λ due to the boundary scattering, as we shall now see.

1.2 Scientific motivation for studying thermally complex nanostructures

As illustrated in the top panel of Figure 1-1, a homogeneous, isotropic thin film of thickness t is an example of a simple nanostructure. The temperature profile $T(x)$ due to an imposed temperature difference $(T_h - T_c)$ in the x direction is linear, and the heat flux $q"$ is also aligned along the x direction. k, however, is reduced from the bulk value due to phonon scattering off the surfaces of the film. The BTE can be solved analytically in this scenario to quantify the thin-film boundary scattering effect on k. The general shape of the resulting analytical Fuchs-Sondheimer solution[4], [5] to the BTE for in-plane transport in isotropic thin films is sketched in Figure 1-1. When the film thickness t decreases below the bulk mean free path Λ, the phonon transport is impeded by the scattering off the film boundaries, and k is reduced. The magnitude of the reduction depends on the nature of phonon scattering off the film surfaces; smooth surfaces reflect the phonons specularly and do not impede in-plane heat flow in thin films, while rough surfaces backscatter phonons and provide resistance to the heat transfer. Finally, because the film thickness t is much larger than the dominant phonon wavelengths λ (which are comparable to the lattice constant for most materials at room temperature), the thin film has the same C and v as the bulk material.

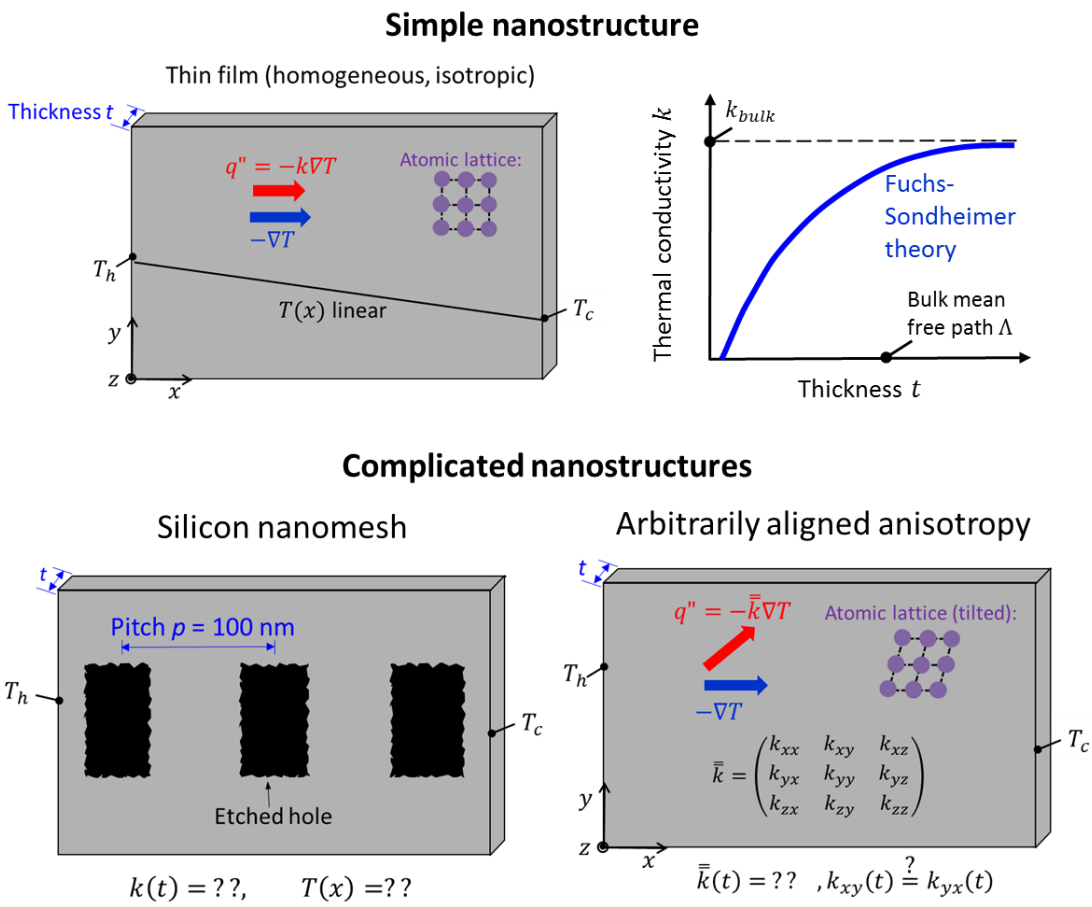

Figure 1-1 : Illustration of simple and complicated nanostructures. This dissertation develops new experimental, numerical, and analytical tools to understand heat conduction in complicated geometries and anisotropic nanostructures.

From an experimental perspective, various optical[6], [7] and electrothermal [8], [9] techniques have been developed to measure k of thin films in the in-plane or cross-plane directions. Because the sample is homogeneous, isotropic, and has a simple geometry, the heat conduction equations for the experimental scenario can be solved and k can be extracted from measured temperature rises and power inputs. The BTE predictions and measured values of k are in generally good agreement (at the ~10-20% level) for simple nanostructures such as silicon thin films or silicon nanowires [3], [10].

The bottom panel of Figure 1-1 illustrates two examples of the complicated nanostructures considered in this dissertation. The silicon nanomesh (bottom left) is a thin silicon film with an array of etched holes with characteristic hole-to-hole pitches of ~100 nm. Some measurements[11]–[13] have been interpreted as indications that BTE theory breaks down in these silicon nanomeshes due to phonon wave interference or "coherent phonon" effects arising from the periodicity of the holes (see Section 1.2.1 below for discussion of coherence effects). However, it is difficult to test whether or not the assumptions of the BTE theory apply in this case, because even obtaining a BTE prediction for the silicon nanomesh geometry is challenging; there are no analytical

solutions to the BTE that can quantify the boundary scattering reduction of k. This absence of a boundary scattering theory has impeded the understanding of heat transfer mechanisms in these complicated nanostructures.

The complexity of the arbitrarily aligned anisotropic thin film (bottom right of Figure 1-1) lies not in the geometry, but rather in the underlying atomic structure. Crystals of sufficiently low symmetry can display anisotropic thermal properties, in which the heat transfer rates depend on the orientation of the temperature gradient to the crystal lattice. In the most general scenario of arbitrary anisotropy, q" is no longer even anti-parallel to ∇T, an effect which is described mathematically by "off-diagonal" components (*e.g.* k_{xy}) in the second-rank thermal conductivity tensor $\bar{\bar{k}}$. BTE solutions for the arbitrarily aligned thin films would enable improved thermal modeling of arbitrarily aligned anisotropic nanostructures of current interest, which range from possible thermoelectric energy conversion materials such as tin selenide[14] to phase-change materials such as vanadium dioxide [15] and layered materials such as black phosphorus[16]. Even the fundamental symmetry requirements of $\bar{\bar{k}}$ in thin films are not known. In bulk materials, a well-known Onsager reciprocity relation [17] mandates that $\bar{\bar{k}}$ is a symmetric tensor (*e.g.* $k_{xy} = k_{yx}$), but it is not known whether a similar reciprocity relation still applies in thin films.

In both examples from Figure 1-1, we see that enhanced complexity brings the possibility of qualitatively new thermal phenomena. For silicon nanomeshes, the geometric complexity of the repeated holes introduces the potential for phonon wave coherence effects that are not present in simpler nanostuctures. In the case of arbitrarily aligned anisotropic films, there may be as many as nine independent components of the $\bar{\bar{k}}$ tensor if the bulk Onsager relation does not extend to thin films. With this rising complexity comes the need for new thermal metrology tools to provide more detailed information about the sample than simply measuring k. I will now discuss how experimental nanothermometry tools could bring new insight into heat transfer in complicated nanostructures.

1.2.1 Nanothermometry motivation

This section motivates the development of nanothermometry tools using several examples from fundamental heat transfer research.

Being able to obtain a full experimental temperature profile $T(x)$ of the superlattice illustrated in Figure 1-2 would provide new insight into heat transfer physics. The superlattice, like the silicon nanomesh, has interfaces between materials (here labeled A and B) where incident phonon energy carriers with wavelengths λ can be reflected. The most interesting regime occurs when the superlattice pitch p is comparable to λ, but is much smaller than the mean free path Λ. Constructive and destructive phonon wave interference occurs if the phonon's phase is coherently persevered over multiple interfacial reflections. These wave effects are referred to as a "coherent phonon" effects, and are analogous to Bragg reflections in thin-film optics.

Once the coherent constructive interference pattern is built up, the phonons do not experience any resistance to heat transfer due to the interfaces, and the temperature is continuous across the interface (Figure 1-2, bottom). However, if the phonon's phase is not preserved over multiple reflections, then the phonon travels incoherently (in a particle-like manner) through the superlattice. In the incoherent case, there is a temperature drop at the interface due to the interfacial boundary resistance[18].

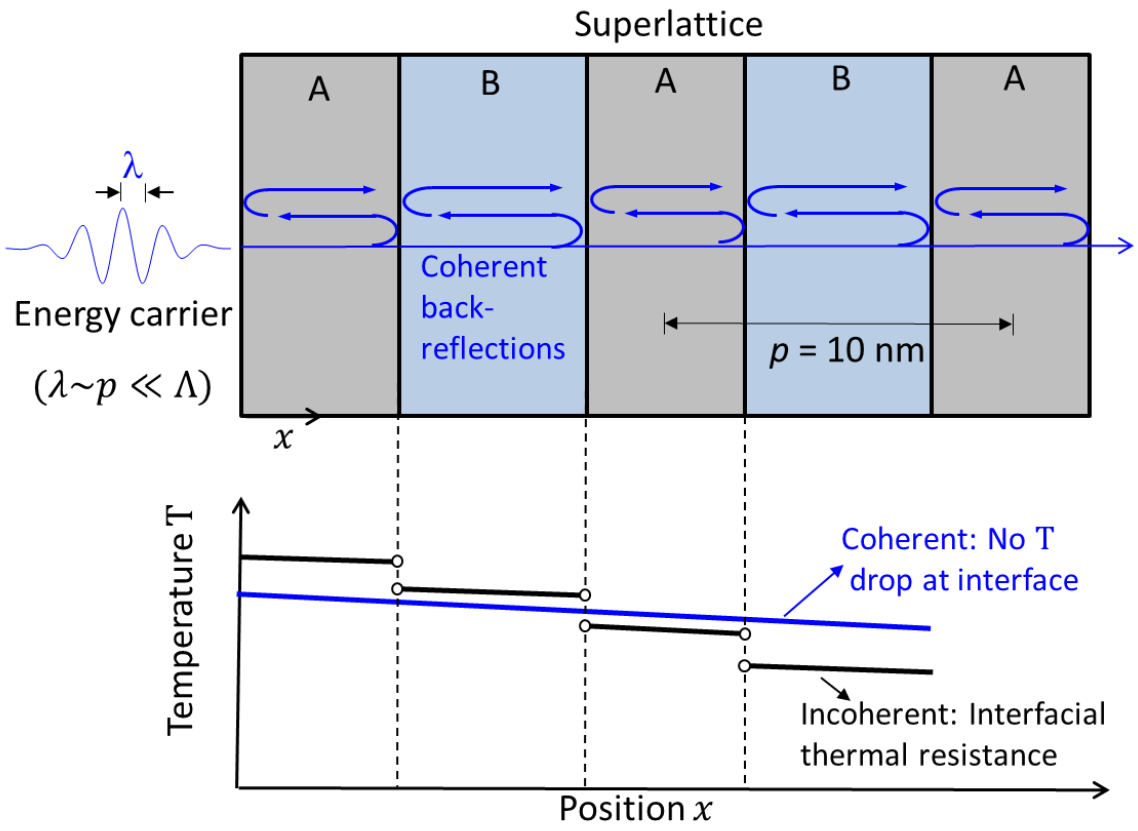

Figure 1-2 : Coherent and incoherent transport in superlattices. If the energy carrier (*e.g.* phonon) undergoes constructive wave interference due to phase-coherent back reflections off of the superlattice interfaces between material A and B, then the phonon travels through the superlattice unimpeded by the interfaces and there is no temperature drop across the interface. However, if the phonon is reflected incoherently, then the interfacial thermal resistance would cause a temperature jump at the interfaces. No current experimental nanothermometry technique can measure this T profile to determine whether phonon transport is coherent or incoherent.

It is difficult to determine whether phonon transport is coherent or incoherent based only on the measured superlattice k. For example, a k that increases linearly with length L [19] can be explained by both coherent and incoherent models for phonon transport. Instead, a direct experimental measurement of $T(x)$ through the superlattice would reveal the degree of phonon coherence by quantifying whether or not the interfaces impede phonon transport. Atomistic simulations have demonstrated that $T(x)$ profiles can be used to distinguish coherent and incoherent phonon transfer in superlattices [20]; unfortunately, no current experimental technique has the sufficient

spatial resolution to obtain this $T(x)$ map in a superlattice. (We will review these current state-of-the-art nanothermometry techniques in Chapter 2.1).

Nanothermometry would also enable new studies of coupled electrothermal processes. Figure 1-3**a** illustrates the coupled Joule heating and electrical biasing in vanadium dioxide (VO_2) thin films. VO_2 undergoes an insulator-to-metal phase transition, which can be initiated either by an increase in T or by an electric field [21], [22]. However, applying the electric field also causes Joule heating and increase the local T, which can lead to nanoscale metallic filament formation[23]. The detailed phase diagram of Figure 1-3**b** is therefore inaccessible to experiment because the local temperature profile $T(x,y)$ is unknown. Nanothermometry experiments that can quantify and map the temperature rise at the VO_2 filament would provide new insight into the fundamental mechanisms of the metal-insulator phase change.

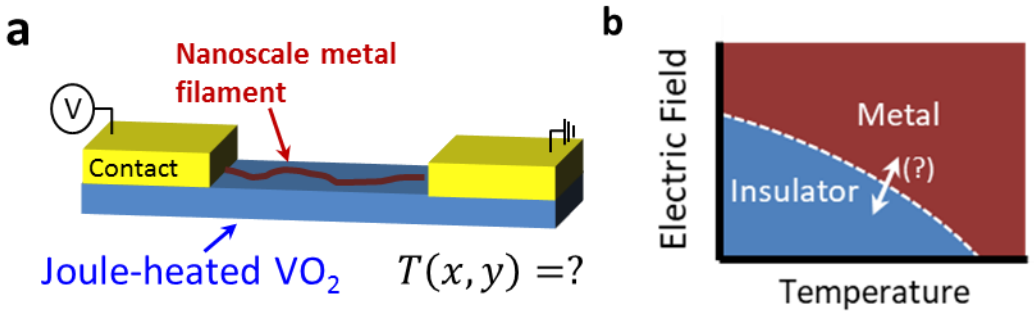

Figure 1-3 : Nanoscale electrothermal coupling in vanadium dioxide (VO_2). **a** Applying a bias voltage to the phase change material VO_2 causes a metal-insulator transition. However, the details of the phase diagram in **b** are not known because the nanothermometry techniques are required to measure the local $T(x,y)$ profile due to the localized Joule heating at the nanoscale metallic filament.

Figure 1-2 and Figure 1-3 displayed examples of fundamental motivations for developing nanothermometry techniques of complicated nanostructures. In the next section, I discuss several applications which would also benefit from advanced nanothermometry techniques.

1.3 Technological motivation

Nanostructures play an important role in information technologies, microelectronics, optoelectronics, solid-state lighting, data storage devices, electromechanical sensors, and solid-state energy conversion devices [24]–[27]. Experimentally measuring the temperature profile of these devices during operation to quantify hotspots and understand local heat dissipation would enable improved thermal design and performance, as we now illustrate with several examples.

Figure 1-4 shows the thermal problems affecting a hard drive data storage technology known as Heat-Assisted Magnetic Recording (HAMR) [28]. The HAMR technology relies upon creating a nanoscale hotspot in the magnetic recording media

(typical magnetic media layer thickness <20 nm). Locally increasing the material's temperature by ~400^{o}C allows the magnetic data to be written in the hotspot using relatively small magnetic fields. When the hotspot cools, the magnetic state is frozen in and the data is stored. The heat is delivered to the medium using a laser beam impinging on a gold near-field transducer (NFT) [29] , which transmits heat to the medium using an NFT peg with a characteristic lateral size of ~25 nm.

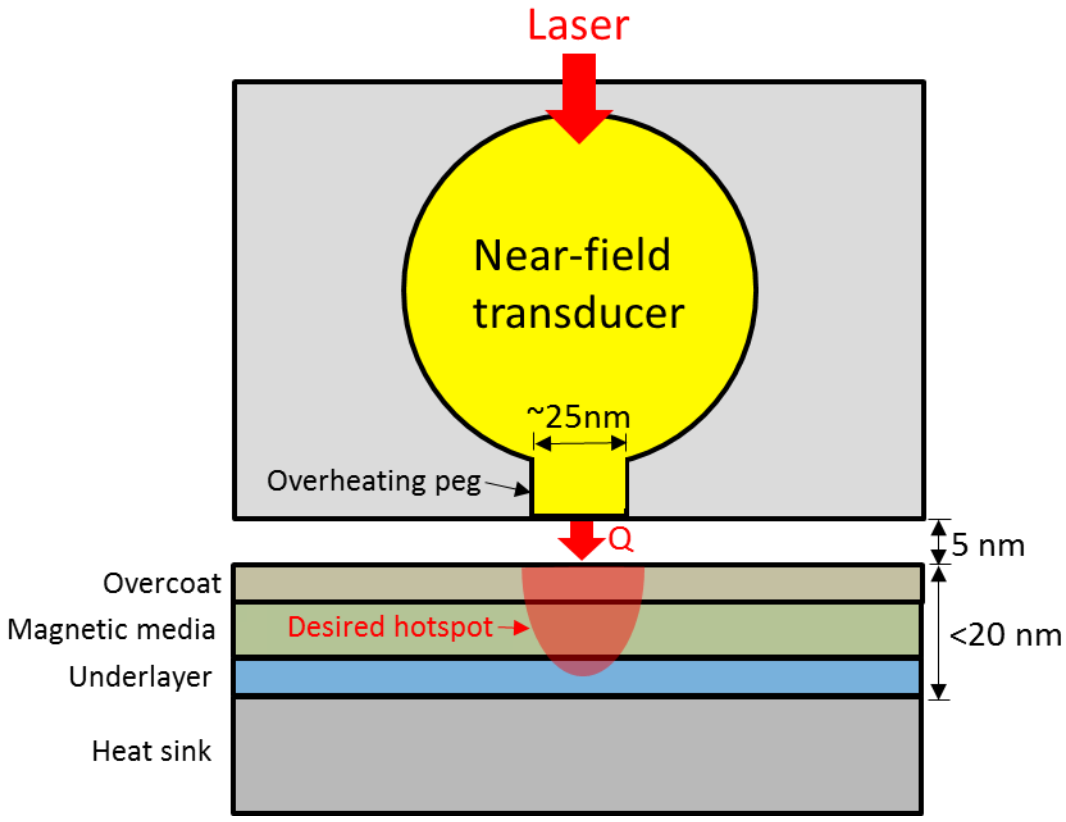

Figure 1-4 : Heat assisted magnetic recording (HAMR) device. The goal of HAMR is to create a nanoscale hotspot in the magnetic media. A magnetic field (not shown) writes the magnetic data in this hotspot. Unfortunately, device failure occurs due to the ~25 nm diameter peg overheating. Nanoscale temperature mapping would assist in the thermal design of HAMR by diagnosing temperature rises and identifying thermal bottlenecks. Figure adapted with permission from Figure 1 of Shi et al., *Nanoscale and Microscale Thermophysical Engineering* 19.2 (2015), p. 127-165 [24].

Clearly, the ability to quantify thermal transport in this geometrically intricate and heterogeneous nanostructure is crucial for the performance of HAMR, since temperature rises are not an unwanted byproduct but rather a desirable feature of the technology. However, a number of thermal issues plague the HAMR device, reducing the reliability and lifetime. A major failure mechanism is overheating of the NFT peg due to optical losses and poor heat dissipation via conduction to the surrounding dielectric. This overheating can lead to mechanical failures as surface diffusion alters the gold transducer shape [24]. Undesirable heat spreading in the magnetic media also reduces the areal density of data storage. New nanothermometry experiments to measure the

temperature rise at the NFT peg and map the temperature inside the magnetic recording medium would enable improved thermal design of the NFT designs and recording media [30], [31].

Another example of a heterogeneous nanostructure is a light-emitting diode (LED). Figure 1-5 illustrates a representative structure of a green/blue gallium nitride (GaN)-based LED [32]. The active region of this LED consists of a silicon carbide (SiC) substrate with thin films of aluminum nitride (AlN), GaN, indium gallium nitride (InGaN), and the light-emitting multiple quantum well (MQW), which itself is composed of alternating InGaN and GaN layers. In the active region, some electrons combine with holes to emit the desired visible light, while other carriers undergo non-radiative decay and deposit their energy as heat. If this heat not removed from the LED, the increased junction temperature reduces the lifetime of the device and can even lead to thermal shock failure [33]. Temperature maps with nanoscale spatial resolution in the LED would help to identify the regions of largest heat generation and thermal resistance in the device, complimenting thermal property measurements [32].

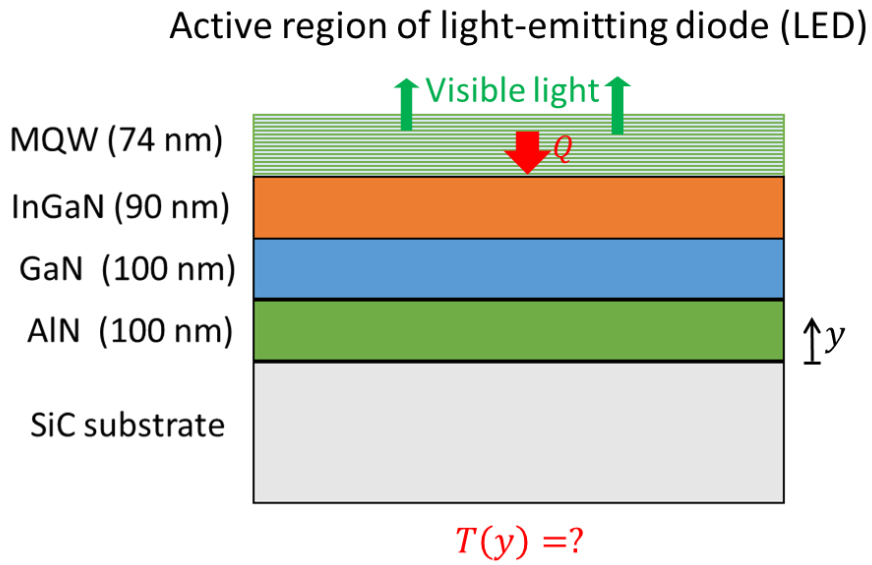

Figure 1-5: Heat transfer in light-emitting diodes (LEDs). The active region of the LED consists of a nanoscale multiple quantum well (MQW) and layers of nitride materials. The electrical bias applied to the LED causes the desired light emission, but also causes heat which must be removed from the LED. Measuring the temperature profile across the interfaces in the LED can help improve the thermal design and enhance the device lifetime. Figure adapted with permission from Su et al., *Applied Physics Letters* 100.20 (2012): 201106 [32].

Microelectronics is a final application motivating the study of heat conduction in complicated nanostructures. The high heat fluxes associated with increased transistor densities and power dissipation rates have motivated many changes in the microelectronics industry, including the move to multicore technologies[27]. However, the temperature profile due to heat dissipation in a single operating transistor remains inaccessible to experiment due to the nanoscale dimensions of the transistor. Indeed,

even numerically simulating the temperature profile near an operating transistor using the BTE is difficult due to the heterogeneous structure and complicated geometry[34]. New nanothermometry techniques, numerical simulations, and theoretical results which could more accurately quantify heat transfer in complicated nanostructures could enable improved design of these microelectronic devices.

1.4 Outline of this dissertation

This dissertation develops experimental, computational, and analytical tools to study heat conduction in complicated nanostructures. The outline of the work is as follows:

- Chapter 2 describes a new nanothermometry technique using temperature-dependent electron diffraction patterns in the scanning transmission electron microscope (STEM). I discuss the current state-of-the-art in nanothermometry, and describe previous thermometry techniques in electron microscopes before demonstrating T −dependent diffuse scattering measurements.
- Chapter 3 continues the theme of experimental nanothermometry by developing a second technique based on the annular dark field (ADF) signal in the STEM. I calibrate T −dependent ADF signals and use these signals to map temperature gradients in a Joule-heated silicon carbide membrane. Chapters 2 and 3 are a first step towards achieving ultrahigh spatial resolution temperature mapping of complicated nanostructures.
- Chapter 4 marks a shift in the dissertation from experiments to theory. In this chapter, I discuss ray simulations of incoherent phonon transport in silicon nanomeshes. These ray tracing simulations quantify the boundary scattering effects in complicated nanostructures. Comparing these boundary scattering simulations with experiments reveals that thermal phonons in silicon nanomeshes travel as incoherent particles, not as coherent waves.
- Chapter 5 presents analytical solutions of the BTE for arbitrarily aligned anisotropic thin films. These solutions quantify the boundary scattering effect on the entire thermal conductivity tensor. Using the BTE, I show that the thermal conductivity tensor of thin films remains symmetric from the bulk through the boundary scattering regimes, reducing the number of independent components of the tensor from nine to six. This example illustrates how analytical results can simplify experimental measurements and analysis of complicated nanostructures.
- Chapter 6 summarizes the work and provides directions for future study.

Chapter 2 : Electron diffraction pattern nanothermometry

A journal publication based on Chapters 2 and 3 in currently in preparation. The electron microscopy was performed at the Molecular Foundry of Lawrence Berkeley National Lab. I would like to acknowledge and thank Karen Bustillo and Andrew Minor for their scientific contributions to this work, and to thank Christoph Gammer for developing the 4D-STEM code.

In this chapter, I survey experimental techniques for mapping temperature at the nanoscale, and proceed to develop a new nanothermometry technique utilizing temperature-dependent thermal diffuse scattering in the scanning transmission electron microscope. I use this diffraction pattern technique to measure temperature-dependent diffuse scattering from a single-crystal gold sample. I conclude by noting challenges with the technique and possible future directions.

2.1 State-of-the-art nanothermometry techniques

Nanoscale temperature mapping capabilities would enable improved thermal design of microelectronics, optoelectronics, and data storage technologies, and would also give new insight regarding fundamental heat transport in nanostructures and across interfaces[24], [26]. However, common microscopic thermometry techniques using far-field optics or resistance thermometry are diffraction and lithography limited, respectively, and cannot achieve nanoscale temperature (T) mapping. These limitations have motivated researchers to develop T mapping techniques with <100 nm spatial resolution [35]–[37], most notably using scanning probe methods such as scanning thermal microscopy [38]–[40], scanning Joule expansion microscopy[41], near-field optical thermometry[42]–[44], scanning noise microscopy[45], or scanning cryogenic thermal sensing[46], [47]. Understanding the parasitic heat transfer pathways between the probe and the sample is critical in interpreting these contact or near-field measurements. Several non-contact nanothermometry techniques have also been demonstrated. Far-field optical techniques can obtain single-point nanoscale T measurements by measuring the light emitted by a single nanoparticle within the diffraction-limited beam[48]–[50], and cathodoluminescence can be used to measure T of semiconducting nanostructures in the scanning electron microscope (SEM) [51].

The possibility of non-contact nanoscale temperature mapping has prompted recent interest in transmission electron microscope (TEM) or scanning transmission electron microscope (STEM) nanothermometry. TEM or STEM techniques would also be useful for measuring the local T during *in-situ* electrical, chemical, and mechanical experiments in the electron microscope, or for quantifying beam heating. Some of these thermometry techniques utilize phase change indicators, such as melted indium islands [52], [53], evaporated gold nanoparticles[54], or vanadium dioxide nanowires[55], as binary thermometers. Phase-change techniques cannot provide continuous T measurements and require phase-change thermometers. Other techniques leverage the mechanism of thermal expansion. Thermal strain maps have been acquired by measuring the strain-dependent plasmon peak shift using electron energy loss spectroscopy (EELS)[56]–[59], or by measuring the lattice parameter from diffraction patterns[60]–[63]. In the scenario of free thermal expansion, local strain maps can be

directly converted into local T maps using the thermal expansion coefficient (typically <30 parts per million (ppm)/K). However, strain arising from fixed mechanical boundary conditions or heterogeneous samples present challenges in data interpretation, since the local strain depends on the boundary conditions and T field in a non-local manner. These challenges can be addressed by depositing freely expanding thermometers such as nanoparticles to measure the local T [59], [64]. Local STEM EELS T measurements have been very recently demonstrated using phonon energy loss and gain spectroscopy[65]. Currently, most electron monochromators do not possess the energy resolution required to distinguish the phonon energy losses or gains from the zero-loss peak.

2.2 Thermal diffuse scattering concept

Thermal diffuse scattering (TDS) is a different T -dependent mechanism affecting signals in the TEM and STEM[66], [67]. At low T when TDS is relatively weak, electrons primarily undergo elastic Bragg scattering, as shown in Figure 1**a**. At higher T, the enhanced atomic vibrations (*i.e.* larger phonon occupation statistics) cause an increase in TDS. In crystals, TDS scattering at higher temperatures reduces the intensity in the elastic Bragg peaks and increases the intensity at other scattering angles, as quantified by T -dependent Debye-Waller factors and illustrated in Figure 1**b**.

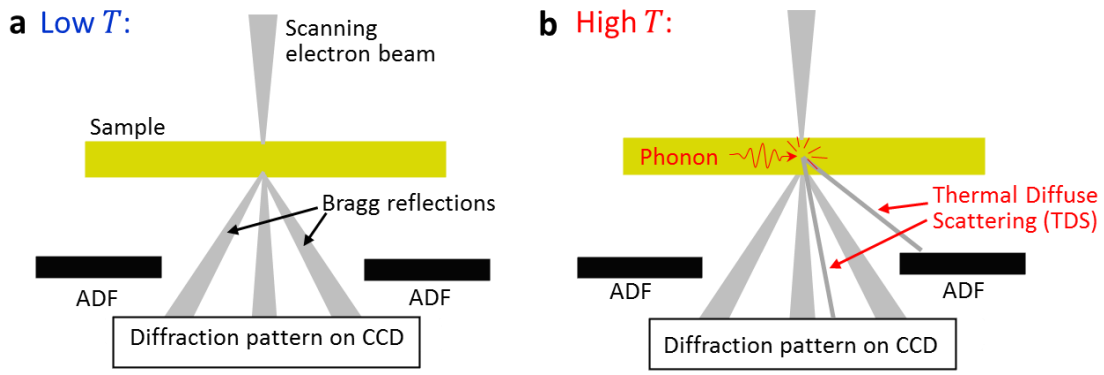

Figure 2-1: Measuring thermal diffuse scattering (TDS) in the scanning transmission electron microscope (STEM). **a** At low temperatures T, the TDS is weak and the electron diffraction pattern displays elastic Bragg peaks. **b** At higher T, the TDS increases due to the enhanced electron-phonon scattering rates. TDS redistributes electrons from the Bragg peaks into the diffuse background of the diffraction pattern or onto the annular dark field (ADF) detector. Here, we develop STEM nanothermometry techniques to measure T –dependent TDS in both diffraction patterns and in ADF signals.

TDS is a potentially promising nanothermometry mechanism because the atomic vibration amplitude is an inherently local T indicator, and is only weakly dependent on strain due to second-order anharmonic effects. In addition, materials of all chemical compositions and microstructures display T -dependent TDS, with the largest temperature coefficients occurring at T larger than or comparable to the Debye temperature of the material. Therefore, local TDS nanothermometry could potentially be performed for many different samples at room temperature and above without requiring additional thermometers to be deposited. Temperature-dependent TDS has

been previously demonstrated in the TEM by measuring the total electron transmission[68], [69], performing EELS of TDS-scattered electrons[70], and acquiring temperature-dependent electron diffraction patterns[71]–[74]. These TEM techniques, however, are not amenable for acquiring the TDS signal as a function of position, as is required for nanoscale T mapping. In contrast, there are several reports of T-dependent TDS measured as a function of position in the STEM[75]–[77] using the annular dark field (ADF) detector, which measures electrons scattered to high angles. These ADF signals have not been calibrated and used to measure or map T.

In this dissertation, I describe the development of two non-contact nanothermometry techniques in the STEM using T-dependent TDS. In this chapter, we demonstrate STEM diffraction pattern thermometry by obtaining a diffraction pattern at different regions of an isothermal sample and calculating the diffuse counts in post-processing using virtual apertures[78]. By comparing the diffuse counts from a gold foil at $\mathrm{T} = 300\ \mathrm{K}$ and $\mathrm{T} = 100\ \mathrm{K}$, we find a position-averaged TDS temperature coefficient of 2400 ± 400 ppm/K. This diffraction pattern technique is most easily applied for single crystal materials. In the next chapter, we measure T-dependent ADF signals and use these signals to map the temperature of a heterogeneous Joule-heated microstructure.

2.3 Acquiring scanning electron diffraction patterns

In scanning electron diffraction experiments (Figure 2-2), diffraction patterns from different beam locations (x, y) are acquired serially by rastering the electron beam. Virtual apertures or masks can then be applied to the diffraction patterns in post-processing to extract information about the local sample microstructure [78] or map the local strain[79], [80]; this procedure is analogous to forming a dark-field image using a physical aperture at the microscope. The virtual aperture approach is more flexible than classic dark-field imaging techniques because the virtual aperture can take any arbitrary shape, and multiple different aperture sets can be applied to the same stack of diffraction patterns. Here, we use virtual apertures to measure the effects of TDS on convergent beam electron diffraction (CBED) patterns. Previous work has shown that corrupting thermal tilt effects can overwhelm the desired TDS changes to the Bragg peak intensity in single crystal diffraction patterns,[60], while the diffuse background counts are less sensitive to tilt artifacts[74]. Therefore, we use virtual apertures to quantify the T −dependent diffuse counts in the background of the diffraction pattern in between Bragg spots.

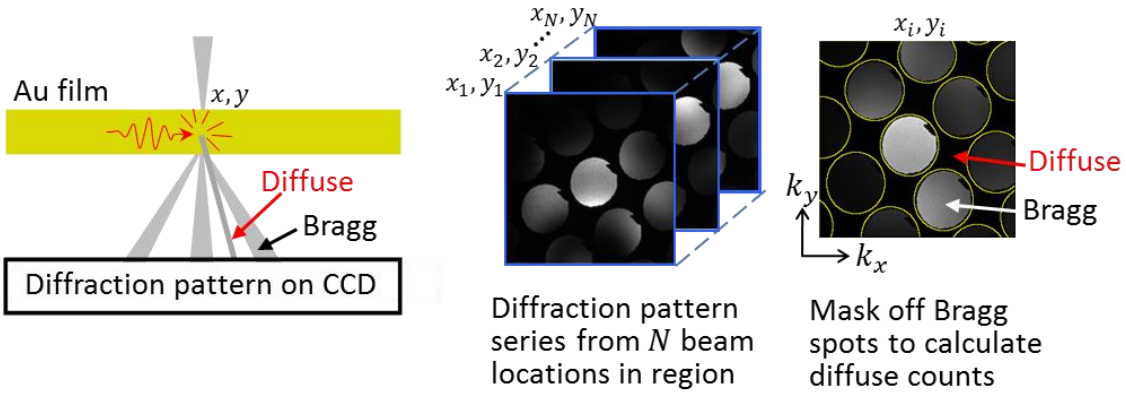

Figure 2-2: Scanning electron diffraction experiments. We acquire energy-filtered diffraction patterns at each beam location of an isothermal gold film. In post-processing, we use virtual apertures to sum the background diffuse counts in between the elastic Bragg spots, and use this diffuse signal for thermometry.

We demonstrate STEM diffraction pattern thermometry using an oriented single crystal gold sample (Ted Pella product #646) with a thickness of 11 nm. This sample was chosen so we could easily isolate the T-dependence of diffuse scattering from confounding effects such as variations in the thickness or microstructure at different positions. We acquire CBED patterns using a Zeiss Libra FEG STEM at 200 kV equipped with a Gatan Ultrascan 1000 camera. We use a convergence angle of $\gamma = 5$ milliradians (mrads), which causes the Bragg peaks to appear as discs in the diffraction pattern (Fig. 2a; the dark notch on the otherwise circular Bragg discs is due to contamination on the condenser aperture). This choice of γ optimizes the diffuse counts signal by enabling relatively long acquisition times (here, 1.5 seconds with 8 by 8 pixel binning) without saturating the CCD with the high intensities in the Bragg discs.

We use an in-column Omega energy filter of 10 eV centered on the zero-loss peak to acquire energy-filtered diffraction patterns[81]. Energy filtering eliminates T-independent diffuse scattering with relatively high electron energy losses (such as electron-plasmon scattering, with typical energy losses around 15 eV) to enhance the fraction of diffuse counts from TDS-scattered electrons, which have much smaller energy losses (<0.1 eV) and are therefore unaffected by the energy filter.

Figure 2-3**a** shows an example room-temperature diffraction pattern from the gold foil. Although the diffuse regions of the CBED pattern appear dark to the naked eye in Figure 2-3**a**, the number of diffuse counts per pixel is at least an order of magnitude larger than the noise floor of the CCD detector. We quantify this noise by inserting the annular dark field detector to shadow the diffraction pattern, as seen in Figure 2-3**a**. Since no electrons can land on the CCD in this shadow, all counts are due to the noise floor of the CCD. In Figure 2-3**b**, we plot the intensity as a function of position along the linecut indicated in **a**. When viewed on this logarithmic scale, it is clear that the number of diffuse counts per pixel between the Bragg spots is more than a factor of 10 larger

that the noise. Therefore, our choice of imaging conditions has enabled diffuse count measurements that are not dominated by the experimental noise.

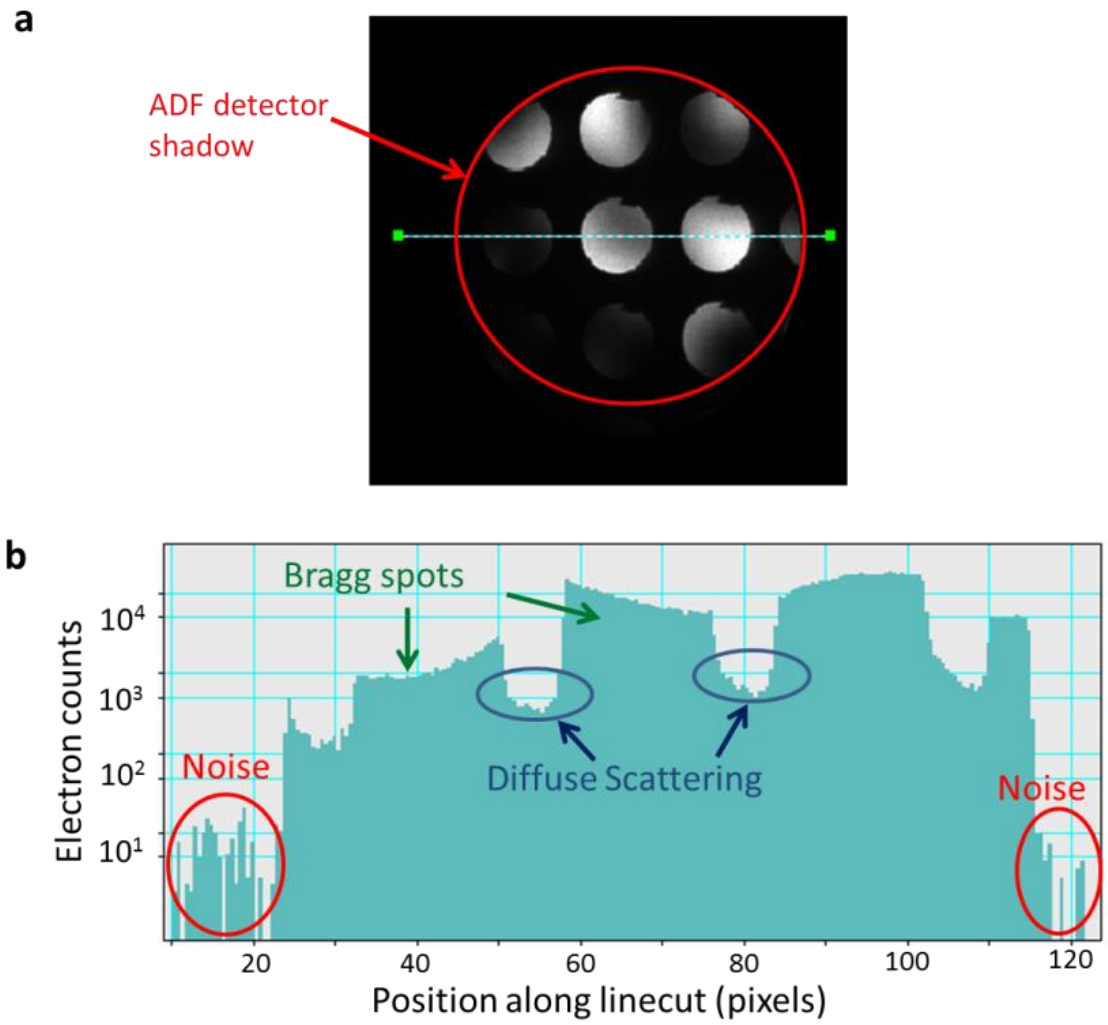

Figure 2-3: Diffuse scattering and experimental noise in diffraction patterns. **a** Room-temperature diffraction pattern of the oriented (100) gold film in the [001] zone axis. We use an annular dark field (ADF) detector to block electrons from hitting the CCD detector outside of the red circle; to the naked eye, both the regions between the bright Bragg spots and the shadowed region of the CCD appear dark. **b** However, plotting the intensity along the linecut in **a** on a logarithmic scale reveals that the diffuse counts are at least an order of magnitude larger than the noise, allowing us to measure T-dependent TDS.

2.4 Estimating electron beam heating

The inelastic scattering giving rise to useful TDS and EELS signals also causes unwanted electron-beam induced heating. The effects of TEM beam heating can be dramatic for samples with low thermal conductivities or poor heat sinking. We now estimate the electron-beam induced temperature rise ΔT for our diffraction pattern experiments. For our continuous gold film suspended on thick aluminum grid bars with a 50 μm by 50 μm mesh spacing, we use a simple radial heat spreading model to estimate

$$\Delta \mathrm{T} = \frac{\mathrm{Q} \ln\left(\frac{r_0}{r_{beam}}\right)}{2\pi\kappa_{Au} t}. \quad (1)$$

Here, Q is the heat deposited by the electron beam of radius $r_{beam} = 2.5\ \mathrm{nm}$, $r_0 = 25\ \mu\mathrm{m}$ is the distance from the beam to the grid bar support, κ_{Au} is the thermal conductivity of the gold film, and $t = 11\ \mathrm{nm}$ is the thickness of the sample. This equation assumes that the electron beam has a top-hat profile and that temperature differences inside the electron beam are much smaller than the temperature drop outside of the beam; consideration of a Gaussian profile and temperature gradients inside the electron beam region do not significantly modify our answer. Note that because the radius ratio is inside the natural logarithm, the $\Delta\mathrm{T}$ estimate is relatively insensitive to values used in this ratio; for example, using the outer radius of the sample of r_0 =1.5 mm instead of the grid radius r_0 =25 μm only increases $\Delta\mathrm{T}$ by a factor of 1.4, indicating that even if the aluminum grid bars do not heat sink the gold film, our estimate will not be in error by orders of magnitude. We are also neglecting radiative losses from the sample to provide an upper bound on $\Delta\mathrm{T}$.

Gold has a room-temperature thermal conductivity of $\kappa_{Au} = 317\ \mathrm{Wm^{-1}K^{-1}}$ in the bulk, but boundary scattering reduces κ_{Au} in thin films[4]. We use the Wiedemann-Franz law $\mathrm{k}_{Au} = L_0 \sigma_{Au} T$ with the Sommerfeld value of the Lorenz number L_0 and previous measurements of the room-temperature electrical conductivity σ_{Au} of 10-40 nm thick gold films[82] to estimate $\kappa_{Au} = 40\ \mathrm{Wm^{-1}K^{-1}}$. In estimating Q, it is important to note that the deposited energy from the electron beam is many orders of magnitude smaller than the incident electron beam energy. This is because the 200 kV electrons only lose a small amount of energy in each inelastic scattering event, and they undergo relatively few scattering events in the thin samples of interest in the STEM. Following Egerton et al.[83], we calculate $\mathrm{Q} = \mathrm{I}(\Delta\mathrm{E})(\mathrm{t}/\Lambda)$, where $\mathrm{I} = 5\ \mathrm{nA}$ is a typical electron beam current, $\Delta\mathrm{E}$ is the average energy loss per inelastic scattering event, and Λ is the mean free path for inelastic electron scattering. Interestingly, since Q increases linearly with t, this model predicts that $\Delta\mathrm{T}$ is independent of t. For gold samples with an incident electron energy of 200 keV, EELS measurements gave values of $\Lambda = 84$ nm and $\Delta\mathrm{E} = 27$ eV [84]. Plugging these numbers in, we find that $\mathrm{Q} = 18\ \mathrm{nW}$ and $\Delta\mathrm{T} = 0.06\ \mathrm{K}$, a value much smaller that the temperature resolution of our diffraction pattern measurement. Therefore, we can safely neglect the electron-beam heating effects in our diffraction pattern experiments.

2.5 Temperature dependent electron diffraction patterns

We quantify both the average T-dependence and the position-to-position variation in the diffuse counts by acquiring a series of N =64 diffraction patterns from a 400 by 400 nm region of the sample. The beam diameter is 5 nm, and the pitch between diffraction pattern locations is 50 nm by 50 nm. After acquiring the series of diffraction patterns, we move to a different region of the sample (typically 5-10 microns away), focus and tilt the sample back into the [001] zone axis, and acquire another series of diffraction patterns. In post-processing, we use Digital Micrograph to sum all N

diffraction patterns from the region, creating a virtual position-averaged CBED (PACBED) pattern. Using ImageJ, we make our virtual aperture mask by marking off all of the Bragg discs of this PACBED pattern. We then apply the virtual apertures to each individual diffraction pattern and sum the diffuse counts outside the Bragg peaks in each pattern. We control T using a double-tilt Gatan 636 cooling holder, and acquire data at $\mathrm{T} = 300\ \mathrm{K}$ and $\mathrm{T} = 100\ \mathrm{K}$. For this global cooling holder, we found the thermal time constant to be around 30 minutes, and significant drift was observed as the temperature changes. We track a characteristic feature on the sample as it thermally drifts to move back to the same general region of the sample after waiting at least one hour for the temperature to stabilize.

Figure 2-4 illustrates the data analysis procedure for representative diffraction pattern measurements at room temperature and T =100 K. The insets in **a,b** display the PACBED pattern with the virtual apertures masking the Bragg spots. We apply this mask and calculate the diffuse counts in each individual CBED pattern (location index i) within the region. Position-to-position variations in this diffuse count signal D reflect both experimental noise and physical differences due to thickness fluctuations, stacking faults, or other microstructural variations. Since the sample is isothermal and nominally homogeneous, we take the mean and standard deviation of this diffuse count signal as representative of the sample location. In this example, the mean diffuse counts at high temperature are larger than the diffuse counts at low temperature, but the error bars are also large. Since the data did not come from the exact same physical location, and because it would be very difficult to achieve identical tilt and focus conditions even at the same location at two temperatures, it is difficult to make concrete conclusions about the TDS from only one diffraction pattern series. However, averaging over many regions at different T isolates the TDS effect, because any non-thermal variations in the diffuse counts will, on average, be the same at the two different temperatures.

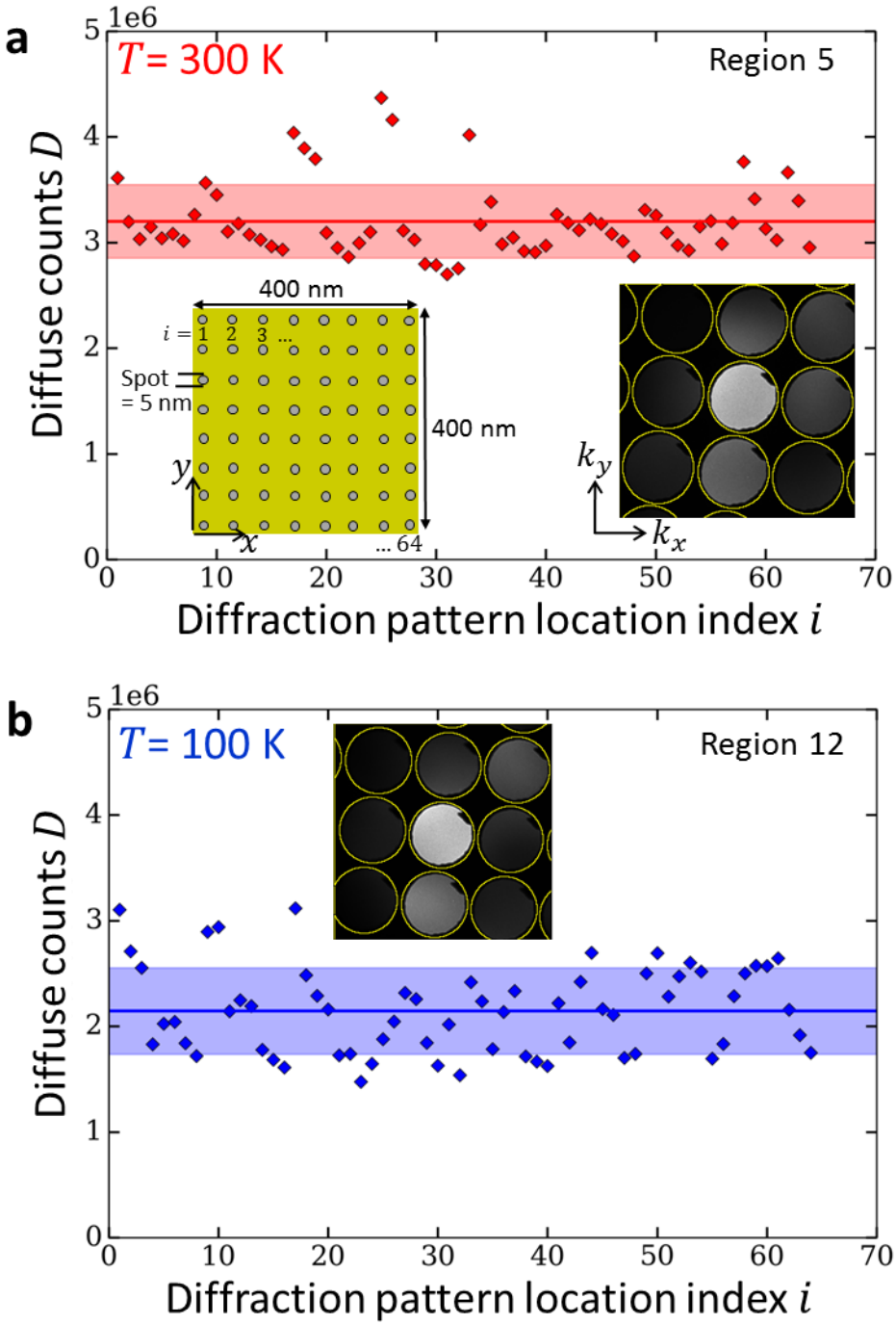

Figure 2-4: Representative diffraction pattern TDS measurements. As illustrated in the inset in the bottom left of **a**, we obtain $N = 64$ diffraction patterns from two 400 nm by 400 nm regions of the sample at **a** $\mathrm{T} = 300$ K (region 5 in Figure 2-5) and **b** $\mathrm{T} = 100$ K (region 12 in Figure 2-5). The inset images in **a,b** show the position-averaged diffraction patterns from all 64 frames with the masked Bragg peaks (yellow circles). We apply these virtual apertures to each individual diffraction pattern in the series to obtain the diffuse counts D for all N frames. We then take the mean (horizontal line) and standard deviation (shaded bars) of D, and plot those values as a single data point in Figure 2-5.

Figure 2-5 shows our T-dependent diffuse counts from the gold film. Each data point represents the average diffuse counts from a 400 by 400 nm region of the sample where the stack was acquired, and the error bars represent the standard deviations of the diffuse counts (as shown in Figure 2-4 for region #5 and region #12). The data is plotted in chronological order. When T is reduced from room temperature to 100 K at region 7, the diffuse counts decrease. When T is increased back to 300 K at region 13, the diffuse counts increase back to the previous room-temperature values, showing the repeatability of the measurement. Indeed, we observe similar diffuse count results when the experiment is repeated two weeks later at a different area of the sample (region 19). We also verified that our measured T effect is not due to differences in the total diffraction pattern counts (including both Bragg peaks and diffuse regions); averaging over the data shown in Figure 2-5, the total counts from $\mathrm{T} = 300$ K locations is $(1.78 \pm 0.26) * 10^8$, within 2% of the $\mathrm{T} = 100$ K value of $(1.75 \pm 0.28) * 10^8$.

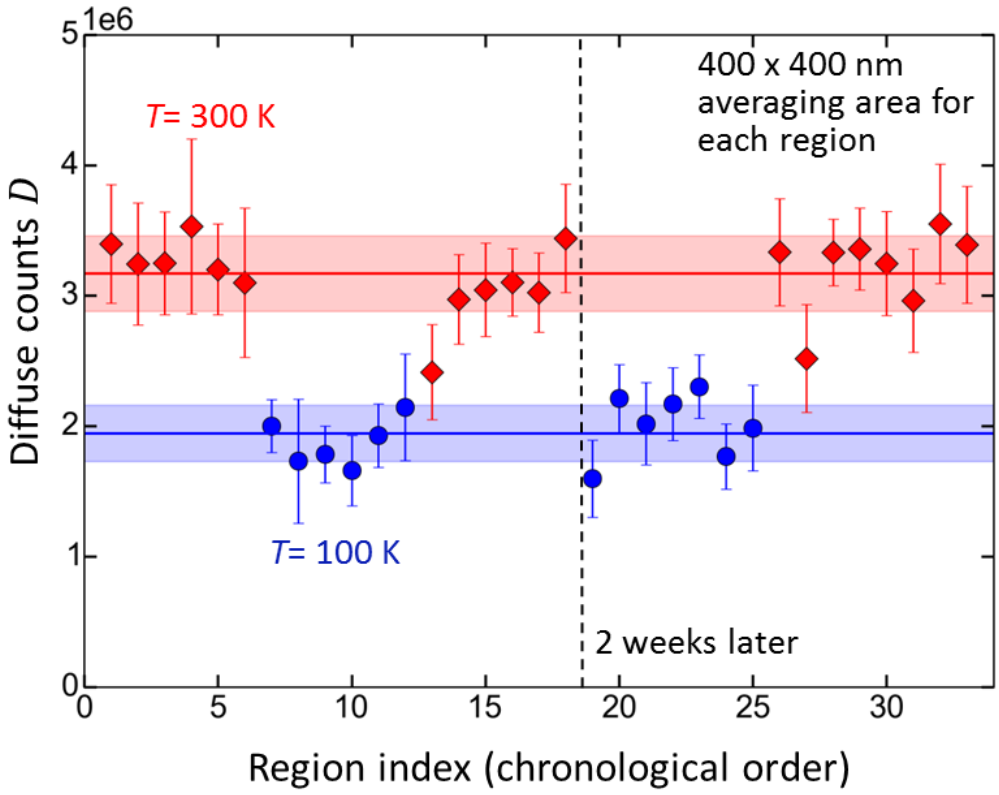

Figure 2-5: Calibrating the TDS temperature coefficient α. We use virtual apertures to find the average diffuse counts from 64 diffraction patterns obtained from a 400 by 400 nm area (error bars represent position-to-position standard deviations). We repeat the calibration at many different sample locations at T=300 K and T=100 K and measure an average $\alpha = 2400 \pm 400$ ppm/K. This experimental result is in order-of-magnitude agreement with a simple Debye-Waller prediction of 5000 ppm/K.

We define the measured diffuse counts temperature coefficient as $\alpha = \frac{1}{D_{\mathrm{avg}}} \frac{\Delta \mathrm{D}}{\Delta T}$, where $\Delta \mathrm{D} = \mathrm{D}_1 - \mathrm{D}_2$ is the difference in the diffuse counts at the two temperatures T_1

and T_2, $\mathrm{D_{avg}} = \frac{1}{2}(D_1 + D_2)$ is the average diffuse counts, and $\Delta T = T_1 - T_2$. Our experimental measurements from Figure 2-5 give $\alpha = 2400 \pm 400$ ppm/K; note that this temperature coefficient is two orders of magnitude larger than temperature coefficients due to thermal expansion (~14 ppm/K for gold). Using the stack acquisition time of 96 seconds (1.5 seconds per frame and 64 frames per stack) and a typical position-to-position variation in the diffuse counts of 10%, we estimate a typical thermal sensitivity of the diffuse counts measurement to be 400 $\mathrm{K\,Hz^{-1/2}}$, indicating that long averaging times will be required for accurate T measurements.

2.6 Comparison with Debye-Waller theory

We now compare our experimental result with a simple Debye-Waller theory. As a first approximation to the complicated inelastic scattering physics[66], [67], we follow He and Hull[74] in assuming that the TDS intensity $\mathrm{I_{TDS}}(k, \mathrm{T})$ at a reciprocal space distance k from the direct beam is proportional to $(1 - \exp(-2W))$, where the Debye-Waller factor for a material with an isotropic Debye phonon dispersion [67] is

$$W = \frac{6\pi^2\hbar^2k^2}{mk_BT_D}\left(\frac{1}{4} + \left(\frac{T}{T_D}\right)^2 \int_0^{\frac{T_D}{T}} \frac{x}{\exp(x) - 1}\,dx\right). \qquad (1)$$

Here, $\hbar$ is the reduced Planck's constant, m is the atomic mass, k_B is the Boltzmann constant, and T_D is the Debye temperature. The first term in the parenthesis in Eq. (1) is due to the zero-point motion of the lattice and dominates at low temperatures, while the second term arises from thermal vibrations and dominates at high T.

In the high temperature limit of $T \gg T_D$, Eq. (1) simplifies to $W = W_{HT} \equiv \frac{6\pi^2\hbar^2k^2T}{mk_bT_D^2}$; this expression can be used with <10% error for all $T > T_D/2$. Gold has $T_D = 165$ K[85], so we take $W = W_{HT}$ for our experiments. The Debye-Waller prediction of the temperature coefficient then becomes

$$\alpha_{\mathrm{TDS}} = \frac{1}{\mathrm{T}}\left(\frac{2W_{HT}\exp(-2W_{HT})}{1 - \exp(-2W_{HT})}\right). \qquad (2)$$

The temperature coefficient of diffuse counts is maximized at small k when $W_{HT} \ll 1$ and $\alpha_{\mathrm{TDS,max}} = \frac{1}{T}$. This $W_{HT} \ll 1$ limit applies for our experiments, since using a value of $k = 0.5$ $\mathrm{Å^{-1}}$ for a typical reciprocal distance halfway between adjacent Bragg spots results in $W_{HT} = 0.03$ at $T = 200$ K. Therefore, the TDS theory predicts $\alpha_{\mathrm{TDS,max}} = \frac{1}{T_{\mathrm{avg}}} = 5000$ ppm/K, which overestimates our measured value by a factor of two. This discrepancy is likely due to the simplicity of our diffuse scattering model, but could also be due to the additional non-TDS diffuse scattering and dark counts in our

experiment, which would add a T-independent contribution to the diffuse counts and reduce α below $\alpha_{\mathrm{TDS,max}}$.

2.7 Summary and future directions

To summarize, we have demonstrated T -dependent diffuse scattering measurements of a single-crystal gold foil in the STEM. Building on previous diffuse count TDS measurements in the TEM [74], we characterized the position-to-position variation of the diffuse counts in STEM and measured a repeatable 2400 ± 400 ppm/K temperature coefficient over many sample locations.

This measurement is only a first demonstration of TDS diffuse counts measurements in the STEM. Future experimental work to quantify the effects of material composition, sample thickness, and temperature on the TDS signal will be necessary to apply the technique. Since the high-T and small W limit $\alpha_{\mathrm{TDS,max}} = T_{\mathrm{avg}}^{-1}$ is independent of material properties, Debye-Waller theory predicts that TDS measurements of all materials would display large α at high temperatures (compared to $T_D/2$). This indicates that 300 K TDS measurements should be feasible for many materials of interest with relatively low T_D (<700 K), including semiconductors such as silicon or germanium and simple metals such as aluminum or platimum. The notable exceptions, for which the zero-point motion still dominates the diffuse scattering and α is reduced at room temperature, are strongly bonded materials such as diamond, graphite, and silicon carbide.

Increasing the thickness of the material will increase the number of diffuse counts, which would enhance the temperature sensitivity. However, He and Hull [74] reported negative temperature coefficients in the TEM for thick samples of germanium, which they attributed to multiple scattering effects. Therefore an intermediate thickness may provide the best tradeoff between experimental signal-to-noise considerations and TDS theory predictions. From the theoretical perspective, multislice or "frozen phonon" simulations [86] can be performed to obtain more accurate predictions of the diffuse counts. These simulations may even reveal optimal virtual aperture positioning or experimental imaging conditions that can further enhance the temperature sensitivity.

Lastly, this scanning diffraction pattern technique is most easily applied to single crystal materials which have relatively simple diffraction patterns in which the Bragg scattering regions and diffuse scattering regions are distinctly separated in reciprocal space. Of course, TDS still affects the diffraction patterns of polycrystalline or amorphous materials, but separating the diffuse counts from the elastic counts may be more experimentally challenging because the elastic scattering is not confined to a relatively sharp Bragg disc. In the next section, we will demonstrate T measurements and T mapping of polycrystalline materials using the annular dark field (ADF) signal.

Chapter 3 : Annular Dark Field nanothermometry

In the previous chapter, I described the motivation for nanothermometry and demonstrated a scanning electron diffraction pattern nanothermometry technique. This diffraction pattern technique is most easily applied to single crystal materials, and the measured signal is relatively noisy. To address these challenges, we develop a different TDS measurement technique using the annular dark field (ADF) detector. TDS scattered electrons can dominate the high-angle scattering measured by the ADF detector, and ADF imaging is easily performed for all sample microstructures. In addition, because the detector provides a single voltage output at each electron beam location, the signal is highly amenable to a lock-in technique. Lock-in amplifiers are commonly used in optical, electronic, and magnetic experiments to isolate small signals at a known frequency from a noisy background.

In this chapter, we use a lock-in amplifier to measure the time-periodic change in the ADF signal from a 100 by 100 nanometer scanning area due to periodic Joule heating. We calibrate the ADF response as a function of temperature rise $\Delta \mathrm{T}$ for silicon carbide and tungsten, and find that the temperature coefficient varies by <10% at different sample positions. The lock-in detection enables improved temperature sensitivities of $12\ \mathrm{K\ Hz^{-1/2}}$ at each sample location. This improved sensitivity allows us to use the calibrated ADF signal to obtain an *in-situ* $\Delta \mathrm{T}$ map of a Joule-heated silicon carbide device. We compare the experimental results with finite-element method (FEM) electrothermal simulations, and discuss future applications of the ADF technique.

3.1 Lock-in measurements of the ADF signal

The ADF image[87] is formed by rastering the electron beam across the sample and recording the voltage output of the ADF detector at each location. The contrast in the ADF image represents the number of electrons scattered into the angular collection range of the ADF detector at different regions of the sample. TDS scattered electrons contribute significantly to this ADF signal[77], [86], [88], [89], indicating that the ADF response can be calibrated and used to map T. Figure 3-1 is an ADF image showing the suspended silicon carbide (SiC) membrane, an etched hole, and a tungsten line deposited on top of the SiC membrane. The tungsten region displays a larger ADF intensity than the SiC membrane due to the enhanced electron scattering in the tungsten, and the variation of contrast within the tungsten is due to the polycrystalline microstructure.

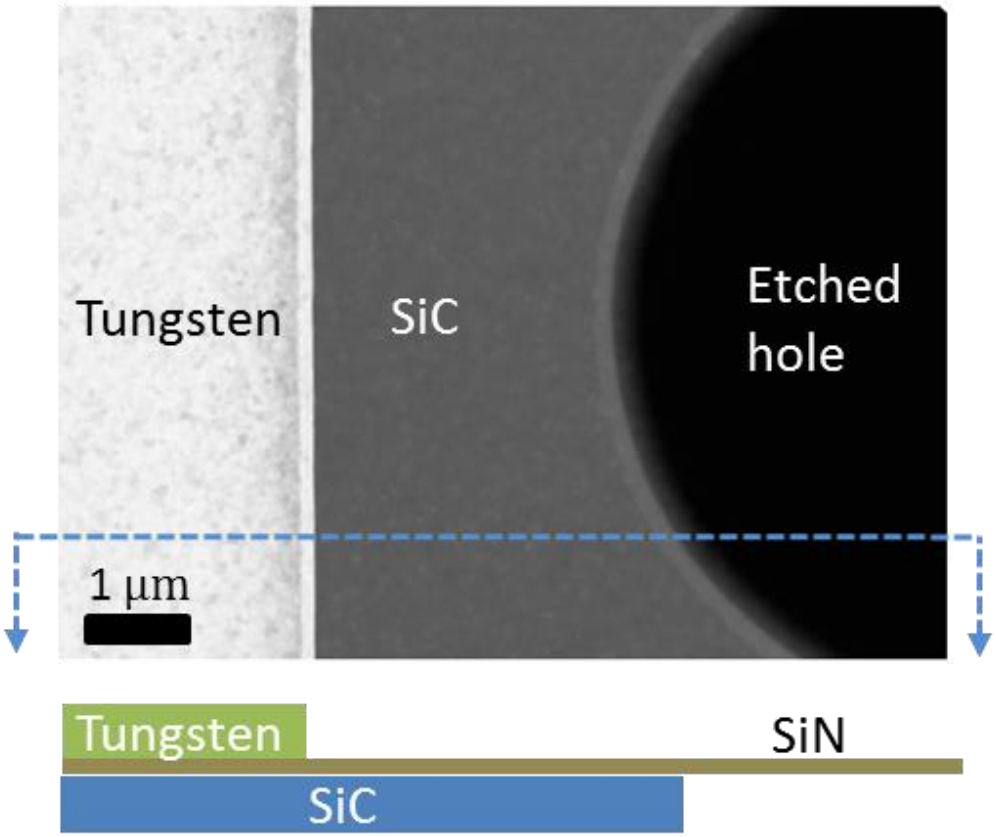

Figure 3-1: ADF image of an electrothermal heating sample. The image shows the Joule-heated silicon carbide membrane with a deposited tungsten line and a etched hole. An electron-transparent SiN layer electrically separates the tungsten and SiC.

We measure T-dependent ADF signals using a lock-in technique, as illustrated in Figure 3-2. Time-periodically heating the sample causes a periodic temperature rise, which in turn induces a periodic component of the ADF signal that we measure using a lock-in amplifier. This AC heating technique improves the signal-to-noise ratio of the measurement by enabling accurate lock-in detection, and also reduces the sensitivity to potential DC drift, contamination, or beam heating artifacts. We use a FEI Titan FEG TEM/STEM operated at 200 kV with $\gamma = 10$ mrads, and detect the ADF signal using a Fischione Model 3000 with typical collection inner semi-angles β ranging from 63-105 mrads. Using a commercial in-situ electrothermal heating system (Protochips Aduro 300), we periodically heat a suspended silicon carbide device (Protochips E-AXA). Each of these MEMS heating devices was calibrated by the vendor using an optical pyrometry technique from room temperature to 900^{o}C. The voltage output of the ADF was connected to a lock-in amplifier (SRS Model 830), which measures the small periodic component of the ADF signal due to the temperature rise. We measure the in-phase and out-of-phase components of the ADF voltage at the fundamental square-wave heating frequency (typically 4 Hz). We use the high reserve setting on the lock-in with a 24 dB/octave filter and a time constant of 3 seconds.

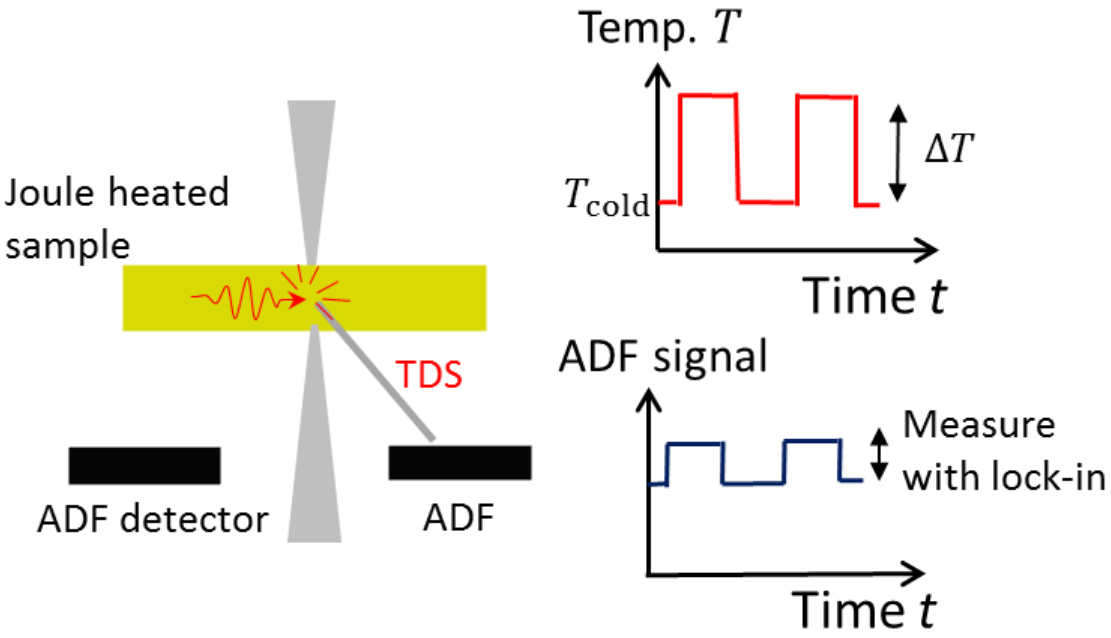

Figure 3-2: Concept of annular dark field nanothermometry. Time-periodically Joule heating the sample increases the TDS and causes a periodic change in the ADF signal, which we measure using a lock-in amplifier.

The most straightforward ADF thermometry protocol would be to leave the beam at one position on the sample as T is varied. However, we found that if the beam is left in spot mode, time-periodic thermal motion relative to the stationary beam location leads to artifacts due to position-dependent contrast variation. If the thermal drift amplitude is comparable to the beam size, then changes in ADF contrast due to position-dependent sample microstructures are detected by the lock-in amplifier, corrupting the TDS measurements. Since the change in contrast due to thermal drift is equally likely to be positive or negative, the in-phase component of the lock-in signal could take either polarity, with a magnitude that is highly dependent on the contrast at the particular sample location. We overcome this thermal drift artifact here by scanning the beam over a 100 by 100 nanometer window during the periodic heating, instead of keeping the beam in spot mode. Typical scan frame sizes of 16 by 16 pixels with a 1 µs dwell time per pixel lead to frame rates that are much faster than the heating times. We find that this effective averaging over a larger area reduces the thermal expansion artifacts and allows us to calibrate the T -dependent ADF signal from a nanoscale region.

3.2 ADF calibration of tungsten and silicon carbide

Figure 3-3 shows a calibration of T-dependent ADF signals for tungsten at six different locations. The in-phase component of the lock-in voltage V_x increases linearly as a function of the temperature rise ΔT above $T_{cold} = 500\ ^{o}C$ for all six locations. V_x is positive for all locations, indicating that the ADF scattering increases with T. The error bars representing the standard deviation of V_x over the 1 minute averaging time are

smaller than the data points in most cases, and correspond to a typical thermal sensitivity of $12\ \mathrm{K}/\sqrt{\mathrm{Hz}}$. The position-averaged temperature coefficient $\alpha_w = 32\ \mu\mathrm{V/K}$ has a standard deviation less than 7%, indicating that a single average α_w can be used for all locations in T mapping. Due to the relatively low heating frequency of 4 Hz, the out-of-phase component of the lock-in voltage V_y (not shown) is much smaller than V_x, displaying an average ΔT dependence of $-1\ \mu\mathrm{V/K}$. The dominant in-phase response indicates that the temperature rises are quasi-steady (frequency-independent).

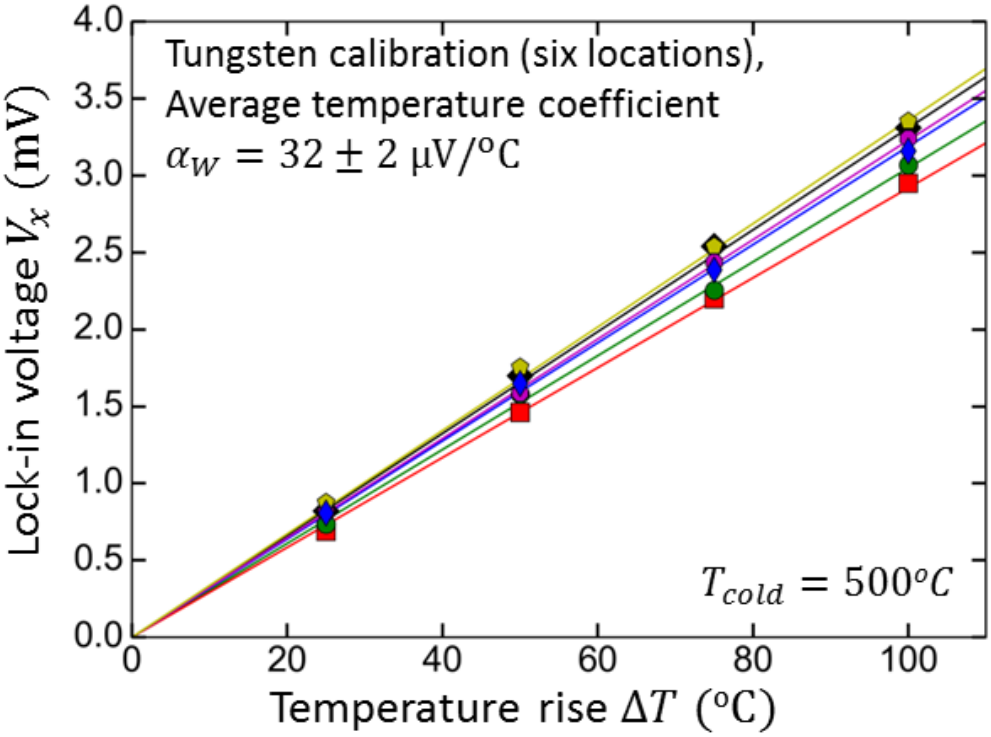

Figure 3-3: ADF calibration of tungsten. We measure the in-phase ADF lock-in voltage V_x as a function of ΔT at $T_{cold} = 500^0\mathrm{C}$, a low heating frequency of 4 Hz, and an averaging time of 1 minute.

The calibration in Figure 3-3 used a relatively large collection angle of $\beta = 63$ mrad. In Figure 3-4 we quantify the effects of different β on the in-phase thermal ADF signal. When β is much larger than the convergence angle $\gamma = 10$ mrad, the strongly scattering tungsten line appears bright in the ADF image (top right) and the in-phase lock-in voltage V_x is positive, as shown here for $\Delta T = 50$ K and $T_{cold} = 300$ K. However, as β decreases to be comparable to or smaller than γ, the ADF image (top left) shows the contrast of a bright field image because the direct beam is captured by the ADF detector and the electrons passing through the tungsten line are outscattered beyond the outer acceptance angle of the detector. In this bright field regime, the in-phase lock-in voltage V_x is negative because increased T causes greater outscattering, reducing the intensity of the ADF signal from the tungsten. Our experiments use the dark field settings of $\beta > 63$ mrad.

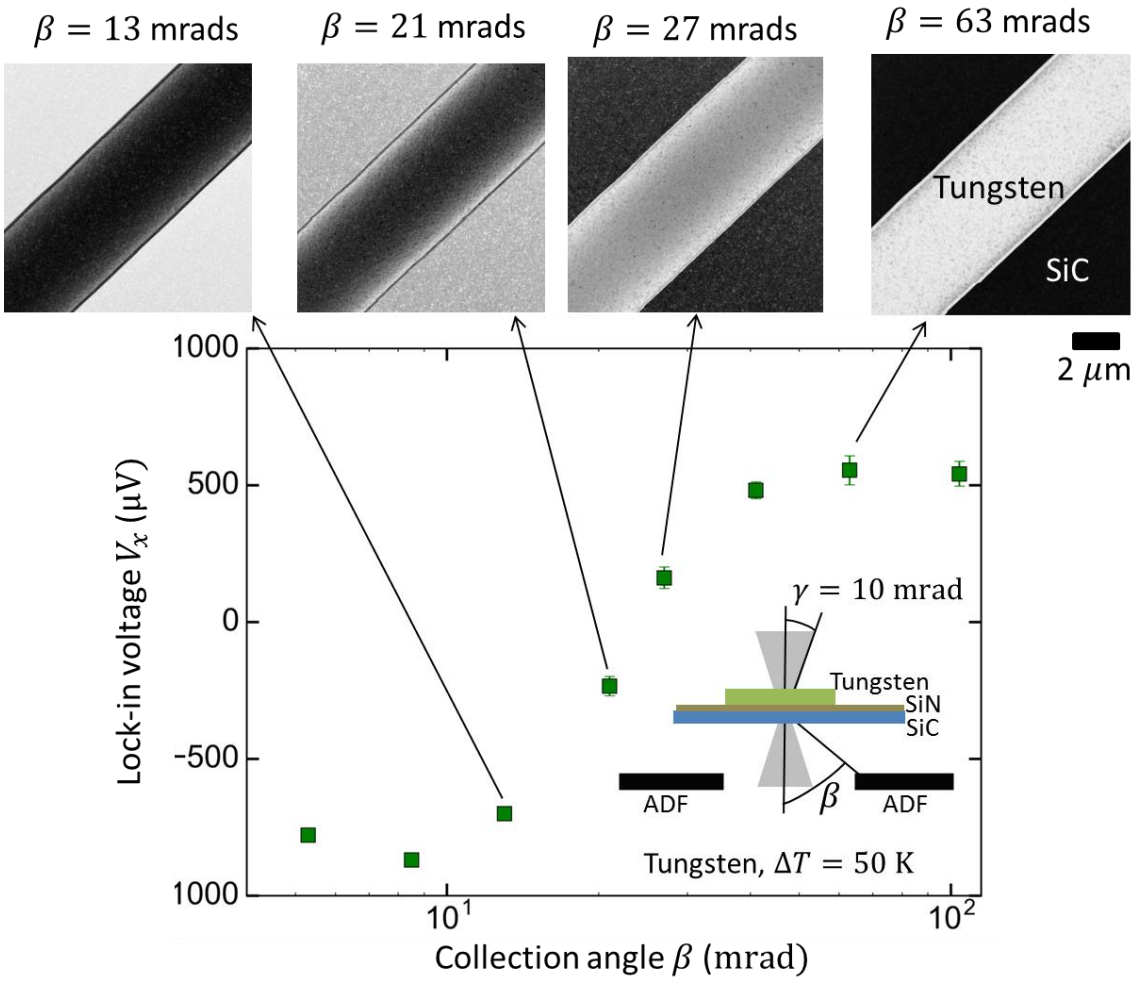

Figure 3-4: Inner ADF collection angle (β) effect on ADF signals from tungsten. The crossover from a positive to a negative in-phase voltage X occurs at small β when the ADF signal begins to measure elastically scattered electrons and displays the contrast of a bright field image.

Figure 3-5 shows a ΔT calibration at four locations on the silicon carbide membrane with $\beta = 105$ mrads. We found that using this larger value of β improved the signal-to-noise of the silicon carbide ADF signal compared to $\beta = 63$ mrads. The silicon carbide membrane displays an average ADF temperature coefficient of $\alpha_{SiC} = 26 \pm 1$ μV/K at $T_{cold} = 500$ °C. We use this relatively high value of T_{cold} because the commercial MEMS heating device is designed for high-T performance, and because silicon carbide has a high Debye temperature of 1200 °C. α_{SiC} is similar in magnitude to α_W and also positive, as expected. However, the dependence of these temperature coefficients on the brightness and contrast settings of the preamplifier precludes direct quantitative comparison, and also means that calibrations should be performed during the same session as ΔT mapping.

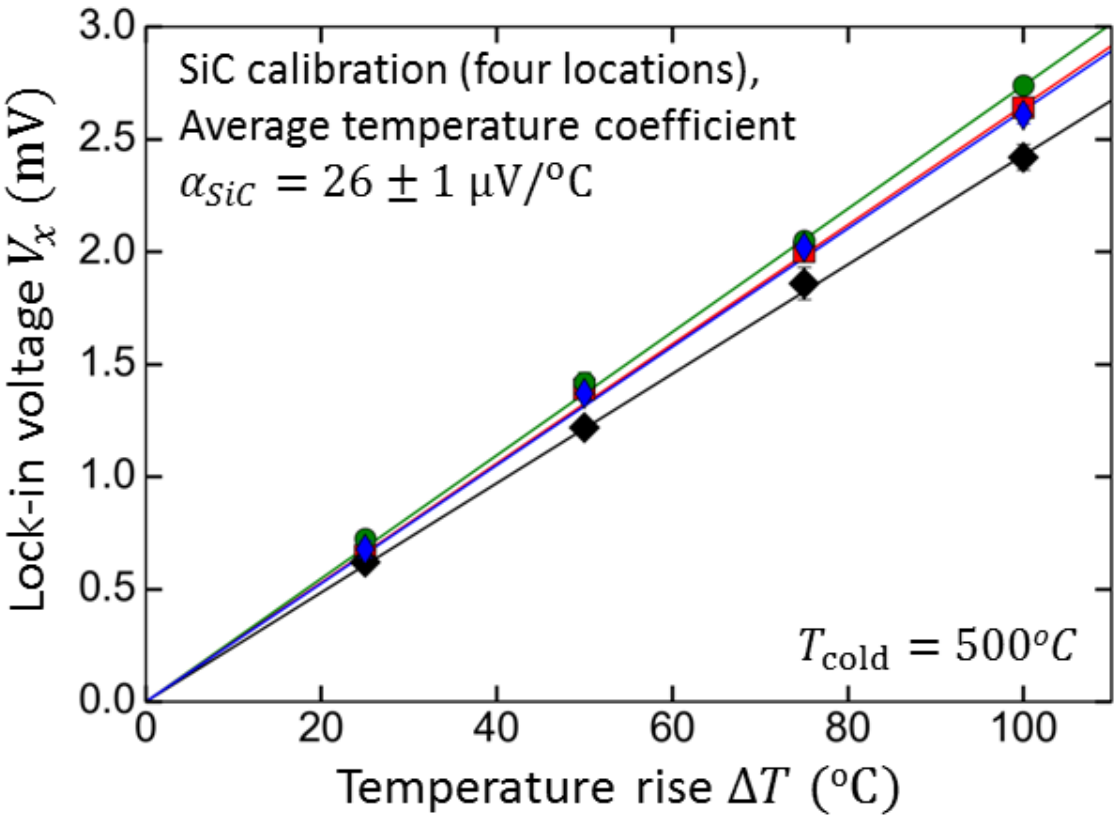

Figure 3-5: ADF calibration of silicon carbide. We measure the in-phase ADF lock-in voltage V_x as a function of ΔT at $T_{cold} = 500^0C$, a low heating frequency of 4 Hz, and an averaging time of 1 minute.

Lastly, we also used the SiC ADF signal to verify that the electric fields used for Joule heating do not lead to electrostatic artifacts, as shown in Figure 3-6. Since electric fields are used in the STEM to focus and deflect electron beams, it is natural to question whether the Joule heating electric fields affect the ADF signal. To separate possible thermal and electrostatic effects, we apply voltages V_W (10V and 20V peak-to-peak square wave at 4 Hz) to the tungsten lines. Since the tungsten is electrically isolated from the silicon carbide, V_W induces an electric field across the silicon carbide between the lines, but does not cause Joule heating. We find that the in-phase lock-in voltage V_X of the silicon carbide does not depend on V_W, even for electric fields of ~7-14 kV/cm that are at least ten times larger than the electric fields used to induce $\Delta T = 25$ K above $T_{cold} = 500^oC$. Error bars represent the standard deviation of V_x over the 1 minute averaging time. We obtained similar null results (not shown) from the effect of electrostatic voltage on the tungsten ADF signal as well.

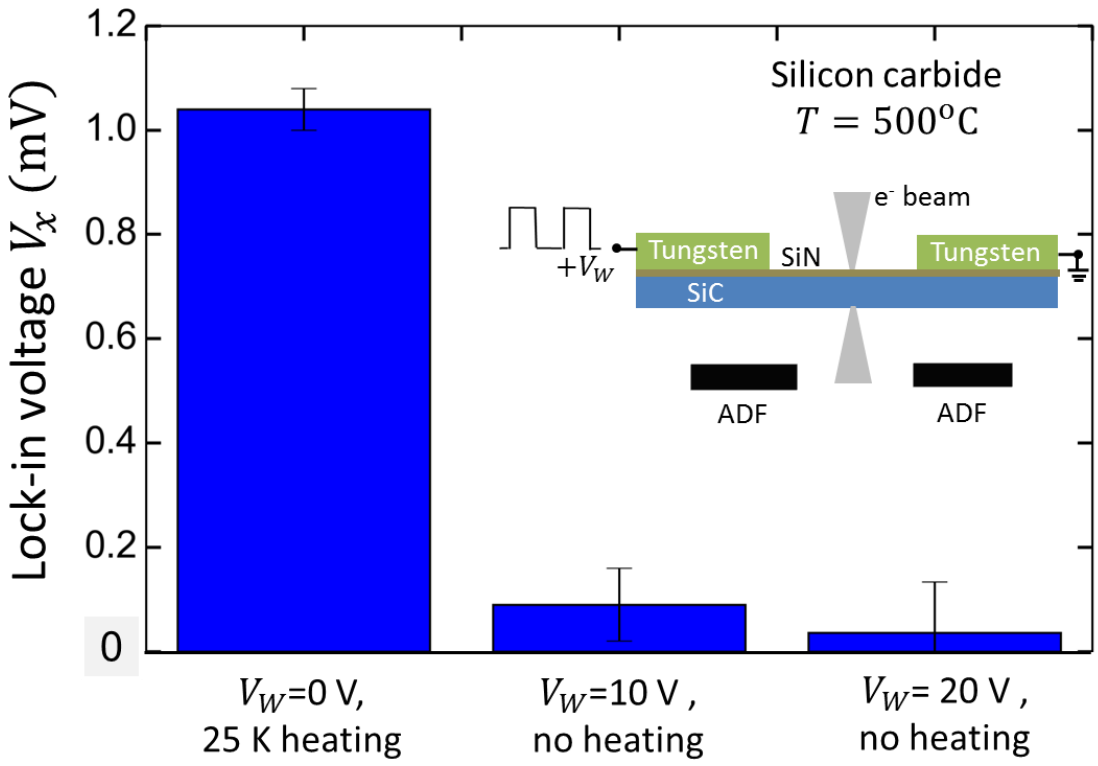

Figure 3-6: Checking for electrostatic artifacts on the ADF signal. The in-phase lock-in voltage V_x is much more sensitive to the temperature rise from Joule heating than it is to applied electric fields with no Joule heating.

3.3 ADF temperature rise mapping at high temperatures

After calibrating the temperature coefficient, we use the ADF signal to obtain an *in-situ* STEM temperature map. The optical image in Figure 3-7**a** shows the semiconducting silicon carbide membrane and ceramic electrodes for Joule heating. Tungsten lines are also deposited on the silicon carbide, but are electrically isolated from the silicon carbide and are not Joule heated. The ADF image in Figure 3-1 and the calibrations in Figure 3-3 and Figure 3-5 were acquired from the central heated portion of the MEMS device, where the nine small etched holes are visible.

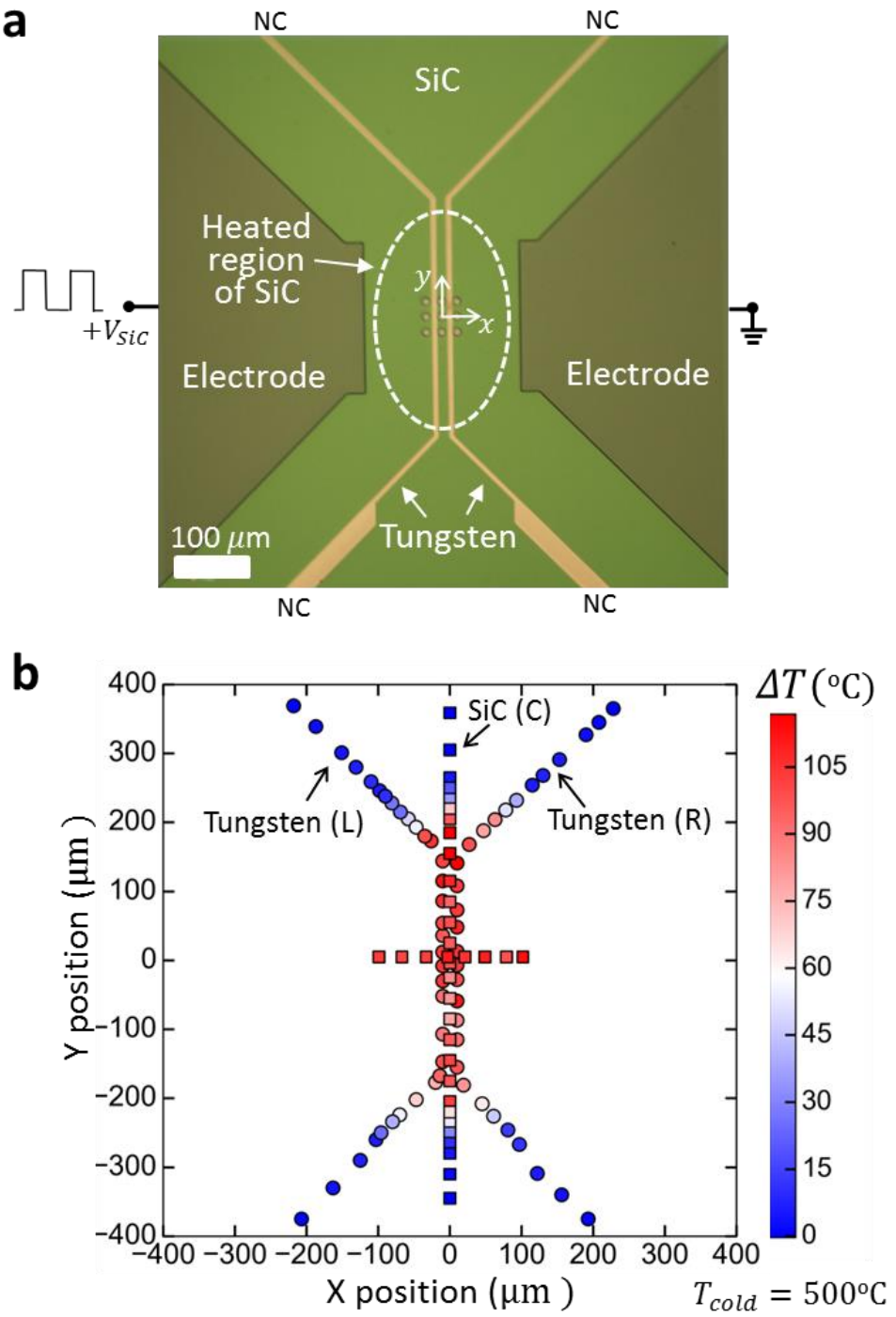

Figure 3-7: Mapping temperature rises at high temperatures using ADF TDS. **a** Optical image of electrothermal heating device. The heating voltage V_{SiC} applied to the electrodes heats the silicon carbide membrane, while the tungsten lines are electrically isolated from the SiC and not connected (NC) electrically. **b** Temperature rise map of the Joule heated device using the ADF technique, demonstrating the ability to map local temperature gradients. ΔT was acquired as a function of position on both the tungsten line and SiC membrane for $T_{cold} = 500^{o}C$, a heating frequency of 4 Hz, and an averaging time of 1 minute.

Figure 3-7**b** shows the measured ΔT as a function of position on the tungsten and the silicon carbide for $T_{cold} = 500^{o}C$. This ΔT map shows that the ADF signal can be used to measure local temperature gradients in the STEM. The averaging time at each location is 1 minute, and the heating frequency is 4 Hz. The good agreement between the measured ΔT on the tungsten and the silicon carbide shows that the technique can be used for multiple materials.

The spatial resolution of this ADF demonstration is determined not by the incident beam size (~2 nm), but rather by the 100 by 100 nanometer scan window required to reduce thermal drift artifacts. This nanoscale scan window allows us to readily map temperature gradients occurring over ~20 μm length scales in the Joule-heated silicon carbide, but temperature gradients with even finer length scales would be required to quantify the spatial resolution of the ΔT measurement. In the absence of thermal expansion artifacts, the spatial resolution of our experiment would likely be limited by the incident beam size, since recent work has indicated the electron-phonon interaction is sufficiently localized to enable high-resolution imaging of vibrational losses [56]–[58].

3.4 Comparison of experimental ΔT map with finite element simulations

To compare the experimental ΔT measurements with theory, we perform finite-element method (FEM) simulations using COMSOL's Joule Heating module to calculate the local heat dissipation in the silicon carbide device. Our experiments use time-periodic heating, but we find that the measured ΔT is always in-phase with the heating, indicating that the heating is slow enough that a quasi-steady temperature rise is reached. We also performed transient COMSOL simulations and verified that this quasi-steady approximation induces <0.2% errors in the maximum temperature T_{max} for the parameters used in Figure 3-7. We therefore discuss our steady-state COMSOL simulations here.

3.4.1 Details of COMSOL simulations

Since the suspended silicon carbide membrane is only 120 nm thick, the thickness Biot number is much smaller than unity and there are no appreciable T gradients in the out-of-plane z direction. Therefore, we perform two-dimensional simulations, while still considering radiative heat transfer from the top and bottom surfaces of the membrane as well as conduction through the membrane. We apply a constant $T = 300\ K$ boundary condition to all edges of the suspended membrane, which is supported by a silicon wafer heat sink. To calculate the Joule heating profile, we electrically ground one of the electrodes and apply a constant voltage boundary condition to the other electrode. The heating voltage for a given T is determined from experiment (Figure 3-8). We ensure mesh convergence by ensuring that T_{max} changes by <0.1% when the mesh density is increased by a factor of two. We note here that performing the full three-dimensional simulations was not only unnecessary, but was in fact more error-prone because of the very fine meshing requirements across the thickness of the membrane.

The parameters used as inputs the COMSOL simulations are shown in Table 1. Many of the parameters are taken from the known geometry of the device, or from handbook values. However, since the electrical conductivity of the silicon carbide depends heavily on the doping level and the thermal conductivity of thin films differs from the bulk, we fit for those parameters as further described below.

Table 1: Input parameters used in COMSOL simulations.

Parameter	Description	Unit	Value	Comment
k_{SiC}	Silicon carbide thermal conductivity	W m^{-1} K^{-1}	$53 * \left(\frac{300\ \mathrm{K}}{\mathrm{T}}\right)$	Fit to experiment in Fig. S6.
σ_{SiC}	Silicon carbide electrical conductivity	S m^{-1}	$1145 * \exp\left(-\frac{800K}{T}\right)$	Fit to experiment in Fig. S6.
t_{SiC}	Silicon carbide thickness	nm	120	Protochips
ϵ_{SiC}	Silicon carbide emissivity	[-]	0.87	Handbook value[90]
k_{el}	Ceramic electrode thermal conductivity	W m^{-1} K^{-1}	k_{SiC}	Assume same as k_{SiC}
σ_{el}	Ceramic electrode electrical conductivity	S m^{-1}	$5 * 10^5$	Assume much larger than σ_{SiC} (absolute number unimportant)
t_{el}	Ceramic electrode thickness	nm	250	Protochips
ϵ_{el}	Ceramic electrode emissivity	[-]	ϵ_{SiC}	
σ_W	Tungsten electrical conductivity	S m^{-1}	$1.0 * 10^7 * \left(\frac{300\ \mathrm{K}}{T}\right)$	Determined by experimental resistance in Fig. S5
k_W	Tungsten thermal conductivity	W m^{-1} K^{-1}	73	Wiedemann-Franz law, $k_W = L_0 \sigma_W T$ with $L_0 = 2.44 * 10^{-8}\ \mathrm{W}\ \Omega\mathrm{K}^{-2}$
t_W	Tungsten thickness	nm	150	Protochips
ϵ_W	Tungsten emissivity	[-]	0.1	Handbook value[90]

We fit the T-dependent electrical and thermal conductivities of the silicon carbide using the measured Joule heating voltage and electrical resistance as a function of T, as shown in Figure 3-8. We invert the vendor calibration of $T(V_{SiC})$ by requesting a given T from the commercial heating device and measuring the V_{SiC} used to achieve that temperature. We then measure the electrical resistance as a function of V_{SiC}. Since the electrical resistance depends on T, the thermal and electrical problems are coupled, requiring simultaneous fitting of the electrical and thermal properties. We find good agreement with experiment by assuming a T^{-1} dependence of the silicon carbide thermal conductivity with a room temperature value of $\mathrm{k}_{SiC}(300\ \mathrm{K}) = 53\ \mathrm{Wm^{-1}K^{-1}}$. The handbook value for single-crystal k_{SiC} is $490\ \mathrm{Wm^{-1}K^{-1}}$ at room temperature[90], but lower room-temperature values of $\mathrm{k}_{SiC} = 62\ \mathrm{Wm^{-1}K^{-1}}$ [91] and $\mathrm{k}_{SiC} = 168\ \mathrm{Wm^{-1}K^{-1}}$ [92] have been reported for polycrystalline silicon carbide, indicating that our fit value is reasonable. The T^{-1} dependence is more typically found in single crystals than in polycrystalline materials; however, we found that we could not successfully fit the experimental results with a temperature-independent k_{SiC}. Using an exponential form of the silicon carbide electrical conductivity typical for lightly doped semiconductors, we find that $\sigma_{SiC} = 1145 * \exp\left(-\frac{800\ \mathrm{K}}{\mathrm{T}}\right)\ \Omega^{-1}\mathrm{m}^{-1}$, with a room-temperature value of $80\ \Omega^{-1}\mathrm{m}^{-1}$.

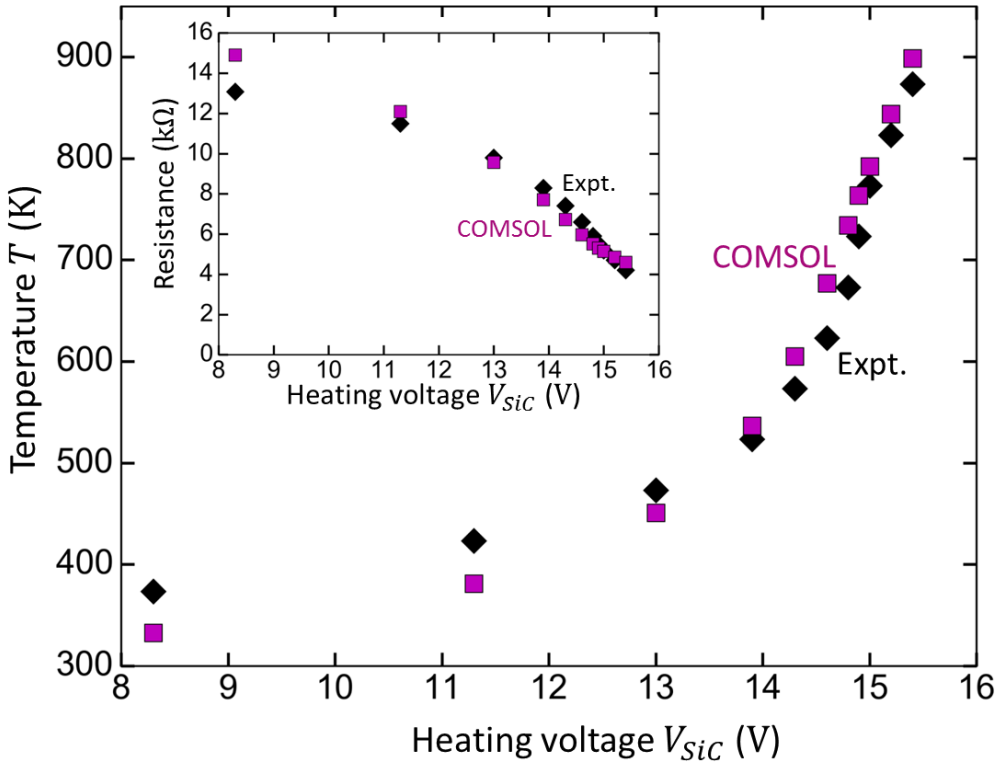

Figure 3-8: Joule-heated SiC temperature rise and electrical resistance. We find that the COMSOL model reproduces both the measured electrical resistance and temperature as a function of the heating voltage V_{SiC} for $\mathrm{k}_{SiC} = 53 * \left(\frac{300\ \mathrm{K}}{T}\right)\ \mathrm{Wm^{-1}K^{-1}}$ and $\sigma_{SiC} = 1045 \exp\left(-\frac{800\ \mathrm{K}}{T}\right)\ \Omega^{-1}\mathrm{m}^{-1}$. We then use these parameters to calculate ΔT profiles to compare with experiment.

3.4.2 Estimating characteristic thermal lengthscales

To understand the relevant thermal processes and check the self-consistency of our assumptions, we estimate the characteristic lengthscales of the thermal problem at $\mathrm{T} = 800$ K. The central heated region has a characteristic half-width of $\mathrm{w}_h = 100\ \mu\mathrm{m}$, and the half-width of the membrane is $\mathrm{w}_{\mathrm{mem}} = 375\ \mu\mathrm{m}$. The characteristic fin length $l_{\mathrm{fin}} = \sqrt{k_{SiC} t_{SiC} / 2h_{rad}} = 193\ \mu\mathrm{m}$, where the linearized radiative heat transfer coefficient $h_{rad} \equiv 4\sigma_{SB}\epsilon_{SiC}T_{avg}^3 = 32\ \mathrm{Wm^{-2}K^{-1}}$, σ_{SB} is the Stefan-Boltzmann constant, and $T_{avg} = 550$ K is the average temperature of the sample and surroundings. At $\mathrm{T} = 800$ K, the thermal penetration depth of periodic heating is $\delta_{SiC} = \sqrt{2\mathrm{k}_{SiC}/(\rho C\omega)} = 665\ \mu\mathrm{m}$, where $\rho C = 3.58 * 10^6\ \mathrm{Jm^{-3}K^{-1}}$ is the volumetric specific heat of silicon carbide [90], $\omega = 25.1\ \mathrm{s^{-1}}$ is the heating frequency, and $\mathrm{k}_{SiC} = 20\ \mathrm{Wm^{-1}K^{-1}}$ is our fit value of thermal conductivity. Because δ_{SiC} is at least a factor of 3 larger than w_h or l_{fin}, our steady-state approximation is reasonable and self-consistent. At lower temperatures, k_{SiC} increases and ρC decreases, so δ_{SiC} will be even larger. This analysis also shows that since l_{fin} is smaller than $\mathrm{w}_{\mathrm{mem}}$, the radiative heat transfer losses from the sample are important at these high temperatures. At room temperature, the smaller h_{rad} and larger k_{SiC} result in $l_{\mathrm{fin}} = 772\ \mu\mathrm{m}$. This value is larger than $\mathrm{w}_{\mathrm{mem}}$, indicating that more of the heat is conducted outwards to the silicon heat sink at room temperature than at high temperature.

3.4.3 Comparison of simulation with experiment

Figure 3-9**a** shows the COMSOL temperature map due to Joule heating of the SiC membrane. We calculate these COMSOL temperature profiles due to the measured Joule heating power inputs required to achieve 500 and 600 $^{\circ}$C, and subtract the T profiles to obtain a $\Delta\mathrm{T}$ map. Figure 3-9**b** compares the experimental results for $\Delta\mathrm{T}(\mathrm{y})$ along the tungsten and SiC from Figure 3-7**b** with the COMSOL simulations for $\Delta\mathrm{T}(\mathrm{y})$ along the tungsten. The experimental temperature profiles are in fair agreement with the simulations; note that there are no free fitting parameters in this $\Delta\mathrm{T}(\mathrm{y})$ comparison. The experimental results show a slightly larger temperature plateau in the heated region and a sharper drop-off to the cooled outer region near the edge of the suspended membrane. The linecuts in Figure 3-9**b** also emphasize that the ADF measurements satisfy the symmetries of the thermal problem; the left and right tungsten lines display very similar $\Delta\mathrm{T}(\mathrm{y})$ profiles, as expected. The theoretical $\Delta\mathrm{T}(\mathrm{y})$ profile lacks an exact mirror symmetry in the xz plane around $\mathrm{y} = 0\ \mu\mathrm{m}$ because the tungsten lines are asymmetric (Figure 3-7**a**); however, this broken symmetry has only a mild impact on the experimental and theoretical $\Delta\mathrm{T}(\mathrm{y})$ profiles.

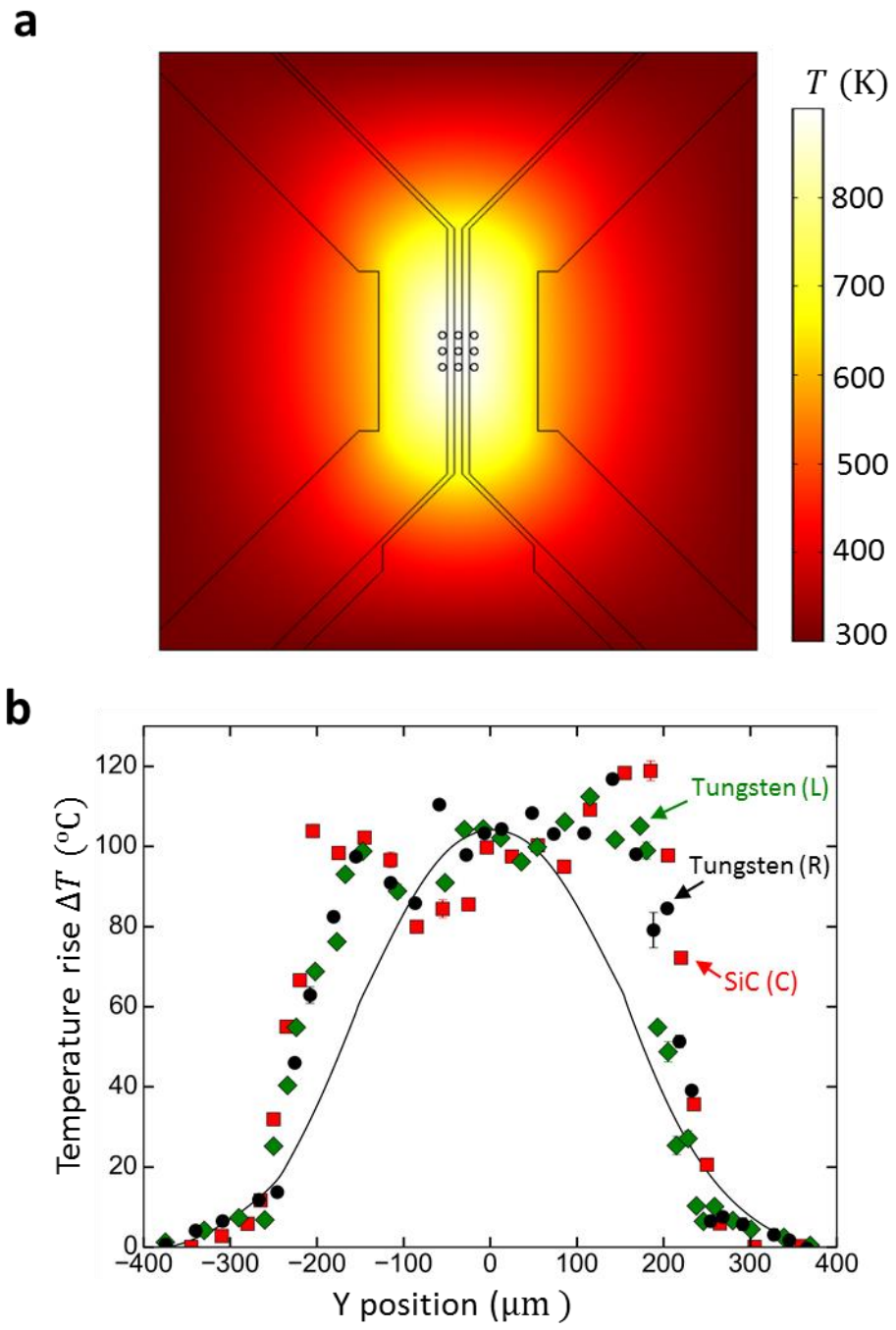

Figure 3-9: Comparing temperature rise experiments and theory. **a** Finite element method (FEM) COMSOL simulations of the temperature profile due to Joule heating of the silicon carbide. **b** The measured $\Delta T(y)$ for the left tungsten line (green diamonds), right tungsten line (black circles), and silicon carbide membrane (red squares) are mutually consistent and in general agreement with the COMSOL temperature rise profile (black curve, no fitting parameters). Error bars representing the standard deviation of the lock-in voltage are smaller than the data points in almost all cases.

3.5 Temperature mapping near room temperature

The measurement of Figure 3-7**b** was performed by Joule-heating the silicon carbide membrane by $\Delta \mathrm{T} = 100^{o}\mathrm{C}$ above $500^{o}\mathrm{C}$. We performed these measurements at high temperatures partially because we found that the temperature calibration was more reliable at temperatures far above room temperature. Figure 3-10 shows that the vendor calibration for small temperature rises ΔT above room temperature has an unexpected heating power dependence of $P^{1/2}$, while the prediction of the COMSOL model follows the linear response trend of P^{1}. At high temperatures, both the Protochips calibration and the COMSOL model follow the expected linear trend. Since the device is calibrated over a large temperature range (up to 900 ^{o}C), and the optical pyrometry calibration technique is most accurate at high temperatures, we choose to work primarily at high temperatures.

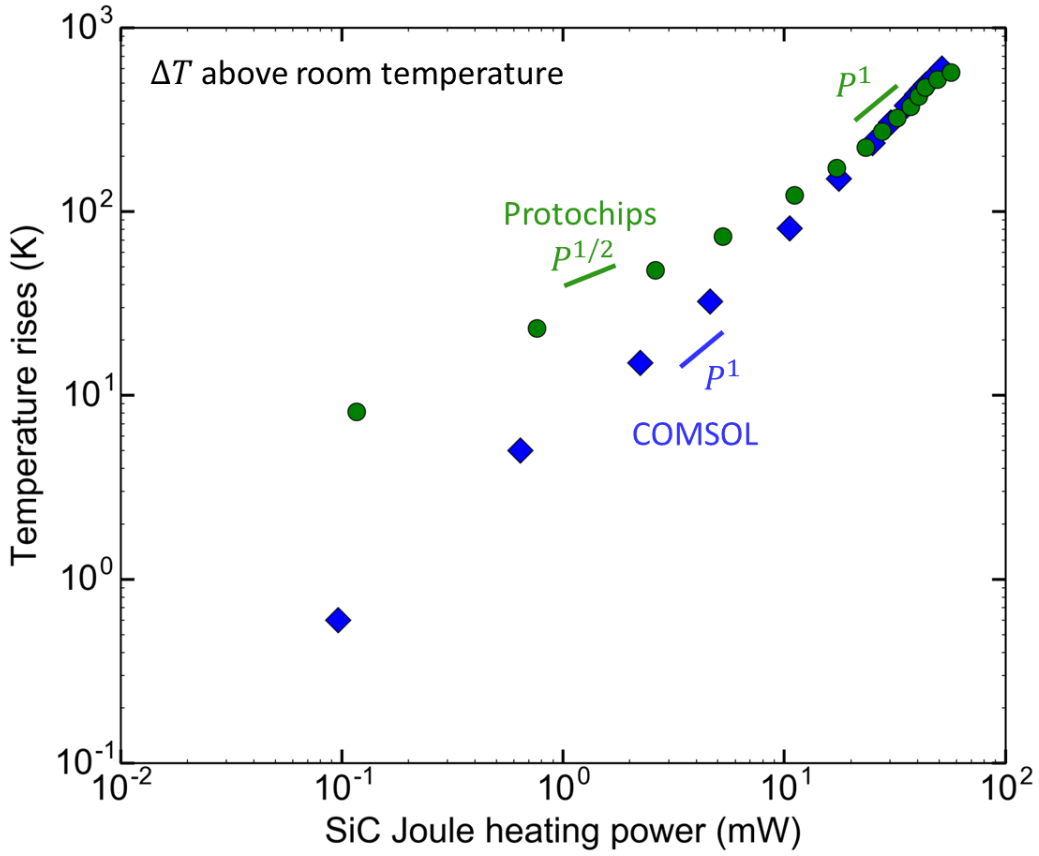

Figure 3-10: ΔT as a function of SiC heating power. The COMSOL simulation results show the expected $\Delta T \propto P^{1}$ trend at small ΔT above 300 K, but the vendor-calibrated temperature has an unexpected $P^{1/2}$ trend at small ΔT. At high ΔT, both the COMSOL and Protochips temperatures follow a P^{1} trend.

To demonstrate that the ADF technique can be used to map $\Delta \mathrm{T}$ around Joule-heated microstructures near room temperature, we deposited a thin (~5 nm) chromium layer connecting the two tungsten lines in Figure 3-11**a**. We then apply bias voltages to the tungsten lines to induce Joule heating; an electron-transparent dielectric SiN layer on top of the SiC layer prevents the tungsten lines from shorting through the silicon

carbide membrane. In Figure 3-11**b**, we plot the in-phase lock-in voltage $\mathrm{V_x}$ as a function of the tungsten Joule heating power $\mathrm{P_W} = \mathrm{V_W^2}/R_s$, where $\mathrm{V_W}$ is the applied voltage to the tungsten lines and $R_s = 599\ \Omega$ is the measured resistance of the tungsten and chromium in series. For small $\Delta\mathrm{T}$, the temperature rise is linearly proportional to $\mathrm{P_W}$, so the calibration implies that $\mathrm{V_x}(\Delta\mathrm{T})$ is also linear at room temperature. We also note that although the chromium is visible in the optical image of Figure 3-11, we cannot detect any changes in contrast of the ADF image due to the chromium because the ADF signal is dominated by scattering from the thicker tungsten and silicon carbide.

Figure 3-11**c** shows the measured lock-in voltage $\mathrm{V_x}$ as a function of position on tungsten line heated at 1.25 Hz with $\mathrm{P_W}$=0.8 mW. $\mathrm{V_x}$ is largest in the middle of the suspended membrane close to the deposited chromium, and decreases near the edges of the supported region. To compare the experiments with theoretical predictions, we perform COMSOL simulations of the experimental geometry using the parameters in Table 1. We use a tungsten electrical resistivity value of $\rho_W = 1 * 10^{-7}\ \Omega.\mathrm{m}$, which is a factor of two larger than the handbook value. We believe this value is reasonable, since the additional grain scattering or boundary scattering in deposited metal lines can enhance the resistivity. By requiring that the total series resistance be equal to the measured value $\mathrm{R}_s = 599\ \Omega$, we find the effective resistance of the chromium section to be $\mathrm{R}_{Cr} = 290\Omega$. The shape of the COMSOL $\Delta\mathrm{T}$ profile in Figure 3-11 is in qualitative agreement with the shape of the $\mathrm{V_x}(x, y)$ profile from experiment. Quantitative agreement is obtained by assuming a temperature coefficient of $10.5\ \mu\mathrm{V/K}$, which is of a similar order-of-magnitude to the high temperature values of $\alpha \sim 25 - 30\ \mu\mathrm{V/K}$, although direct comparison is hindered by the different preamplifier settings used at room and high temperatures. The standard deviation of the lock-in signal corresponds to a temperature sensitivity of $63\ \mathrm{K\ Hz^{-1/2}}$. This temperature sensitivity is a factor of 5 larger than the $12\ \mathrm{K\ Hz^{-1/2}}$ sensitivity from Figure 3-7, which could be due to the larger $1/\mathrm{f}$ noise at 1.25 Hz compared to 4 Hz, or due to the smaller temperature coefficient at room temperature.

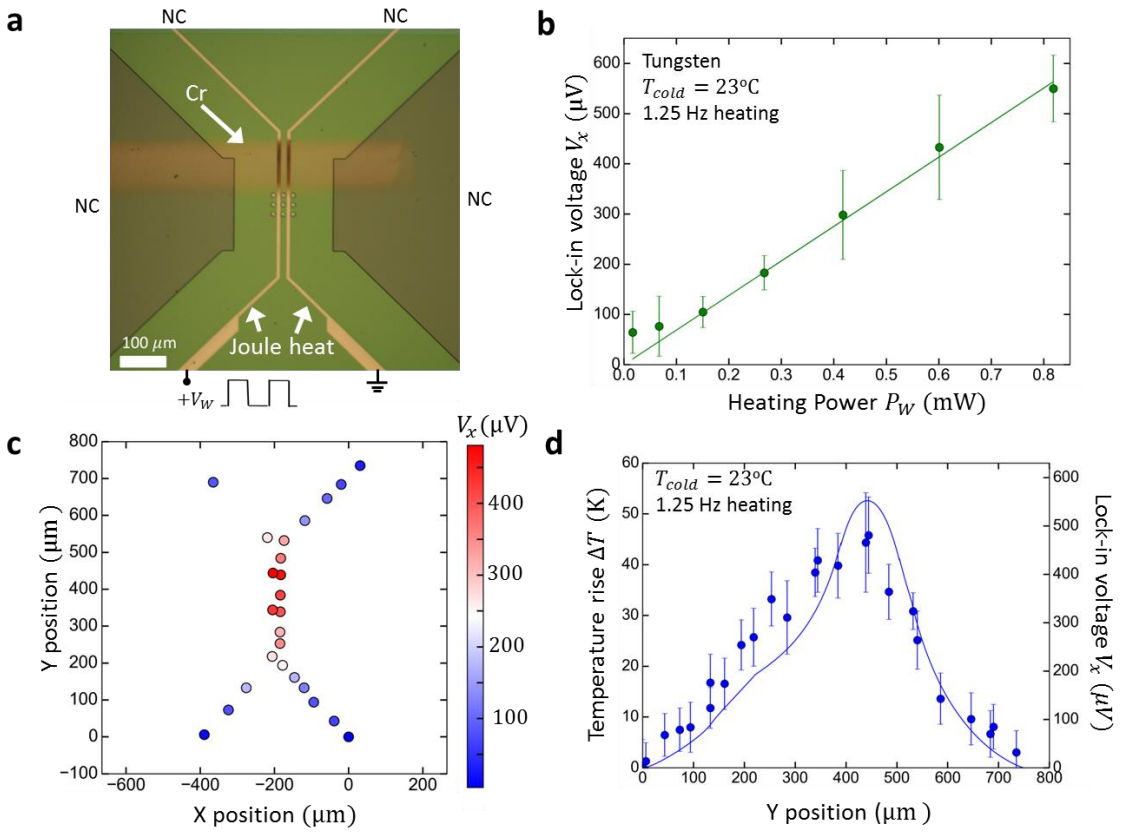

Figure 3-11: Room temperature ADF mapping of a Joule-heated microstructure. **a** Optical image of electrothermal heating sample with evaporated chromium connecting the tungsten lines. We apply a bias voltage V_W to Joule heat the tungsten and chromium; in these experiments, the electrodes are not connected (NC) electrically and the silicon carbide is not Joule heated. **b** The lock-in voltage V_x of the tungsten line increases linearly with the input Joule heating power P_W. This linear response is expected because ΔT is linearly proportional to P_W for small temperature rises. **c** ADF map of the Joule-heated tungsten-chromium circuit at room temperature with P_W =0.8 mW peak-to-peak, a heating frequency of 1.25 Hz, and an averaging time of 2 minutes. **d** Linecuts of the experimental lock-in voltages (points, right axis) and the COMSOL temperature rise ΔT (line, left axis) along both tungsten lines due to Joule heating, illustrating the good agreement between experiment and simulation for a temperature coefficient of $10.5\ \mu V/K$.

3.6 Summary and future work

In this chapter, we developed a time-periodic heating method using a lock-in amplifier to measure T-dependent annular dark field signals from polycrystalline tungsten and silicon carbide. We used this ADF technique to map the temperature rise of a Joule-heated silicon carbide membrane, and compared our experimental results with simulations. We also showed that the ADF signal can be used to map temperature gradients near room temperature. This TDS nanothermometry demonstration offer new capabilities for temperature mapping of electron-thinned microelectronic devices or nanostructures of fundamental interest.

The immediate next steps for the TDS measurement technique would include calibration of different materials, including both crystalline and amorphous samples of

different chemical composition. The effects of sample thickness will also be important to consider. Thinner samples have less ADF scattering, and the thermal sensitivity may be reduced unless optimal collection angles or imaging conditions can be chosen. Comparing measurements of the temperature rise profiles to further theoretical predictions will also be necessary to ensure that the ADF signal corresponds directly to the temperature rise in all experimental scenarios.

The time-periodic heating components of the ADF experiments can be further explored as well. Our measurements are performed at low heating frequencies, where the thermal response is quasi-steady and frequency-independent. This low-frequency limit is desirable for thermal metrology of steady-state systems. However, the time-periodic thermal response of a system is leveraged by common thermal measurement tools ranging from three-omega electrothermal techniques[93] and time-domain thermoreflectance[6] to variations of Angstrom's method[94]. If higher heating frequencies are used, then both the in-phase and out-of-phase signals will contain thermal information about the system. Measuring the ratio of the in-phase and out-of-phase signals can be convenient because this ratio is independent of the temperature coefficient, meaning that some thermal information can be extracted without the need for calibration.

A main direction of future work will be quantifying and improving the spatial resolution of TDS STEM nanothermometry. We sacrificed spatial resolution in our current demonstration by scanning the electron beam over a 100 nm by 100 nm region to avoid thermal drift artifacts. This scanning requirement could be eliminated by performing the lock-in analysis digitally in post-processing, rather than using hardware at the microscope. If stacks of annular dark field images were acquired as the sample is time-periodically heated, image processing tools could be used to correct for the thermal drift, aligning the images through the stack by tracking a characteristic feature. The Fourier transform with respect to time of the drift-corrected ADF signal would then be analogous to the signal currently measured using the lock-in amplifier. Indeed, this type of digital lock-in analysis could also be applied to improve the sensitivity of the diffraction pattern technique discussed in the previous section.

The spatial resolution of the ADF technique could be demonstrated by mapping the thermal point spread function or line spread function. If a known sharp feature in the true temperature profile is created due to a nanoscale heat source or a nanoscale gap separating a hot and cold region of the sample, then the measured ADF temperature profile will be a smeared convolution of the true temperature profile and the probe's thermal response function. The response function could be smeared due to the scan window, or if the thermal drift is accounted for in post-processing, the beam size. For thicker samples, the scattering through the sample can further broaden the probe size. Quantifying this thermal spread function will be crucial in understanding the fundamental limits of ultrahigh spatial resolution T mapping.

Chapter 4 : Ray tracing simulations of phonon transport in silicon nanostructures

Content adapted with permission from J. Lee*, W. Lee*, G. Wehmeyer*, S. Dhuey, D.L. Olynick, S. Cabrini, C. Dames, J.J. Urban, and P. Yang, "Investigation of phonon coherence and backscattering using silicon nanomeshes," *Nature Communications* **8**, 14054 (2017). Here, I focus primarily on the ray tracing simulations and compare my simulation results to the experiments performed by my collaborators (Jaeho Lee and Woochul Lee).

In this chapter, I describe a ray tracing simulation technique to quantify boundary scattering in geometrically complicated nanostructures known as silicon nanomeshes. I validate this ray tracing technique against previous numerical BTE solutions and experiments, and use the simulation results to model my collaborator's silicon nanomesh experiments. The good agreement between the ray tracing results and experiments indicates that that coherent phonon effects are not important for nanomesh pitches greater than 100 nm or temperatures above 14 K. The ray tracing results also provide insight into the role of phonon backscattering in the boundary scattering reduction of k.

4.1 Silicon nanomesh motivation: Coherent and incoherent phonon transport

Classical theories based on the Boltzmann Transport Equation (BTE) that treat phonons as incoherent particles have accurately described the size-dependent thermal conductivity (k) in silicon thin films[95] and high purity nanowires[96], [97]; these k reductions are due to mean free path suppression from boundary scattering. However, recent k measurements of superlattices[19], [98] and of silicon nanomeshes[11], [12], [99], [100], which are thin membranes with a fabricated periodic mesh of nanoscopic holes, have called into question the validity of this particle-based BTE approach when applied to periodic nanostructures. The periodic holes in the nanomesh introduce a secondary artificial periodicity to the original lattice, potentially modifying the phonon dispersion relations and scattering from the bulk in a phononic crystal analogy to photonic crystals[101]. The resulting phononic bandgaps and reduced group velocities would lead to a lower k than predicted by the particle-based models. This k reduction is referred to as a coherence effect due to the required phase coherence of phonon waves. Because the phonon band structure and transport properties inherently arises from the secondary periodicity of the holes, the periodic and aperiodic nanomeshes illustrated in Figure 4-1 would have different k within the coherent model. This reduction in k due to aperiodicity has been numerically demonstrated for acoustic wave propagation in the nanomesh[102] and phonon transport in superlattices[20].

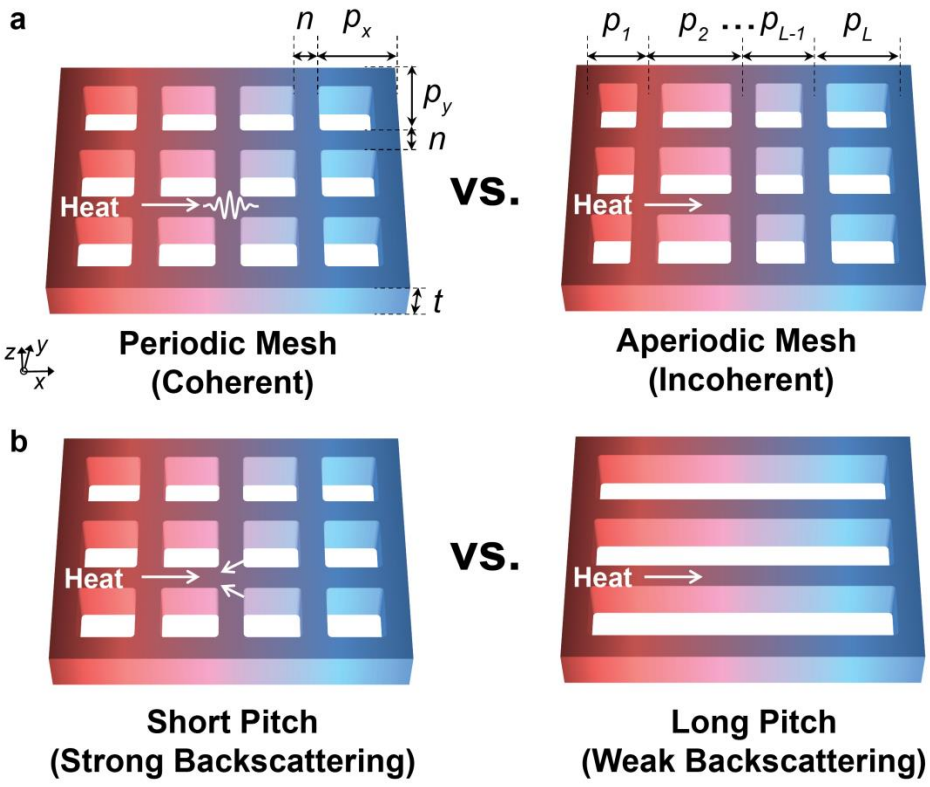

Figure 4-1: Silicon nanomesh concept to investigate phonon wave coherence and particle backscattering. **a** Coherence effects are isolated by comparing periodic and aperiodic nanomeshes with identical thickness (t), neck size (n), transverse pitch (p_y) and average pitch along the direction of heat flow *(p_x)*, while varying the aperiodic individual pitches *(p_1, p_2,...)* by up to ± 20 % around the nominal p_x=100 nm. Coherence effects would be sensitive to the periodicity variations, and ray tracing simulations will show that the boundary scattering is not. (**b**) The backscattering effect is quantified by comparing short and long pitch silicon nanomeshes with fixed p_y, n and t, while varying p_x between 100 nm and 1 µm for different samples. The bridging necks in the short pitch nanomeshes increase the phonon backscattering as compared to the long pitch nanomeshes.

While the prospect of controlling phonon waves is attractive for potential phononic systems[103], [104], experimental reports remain inconclusive on the relative importance of wave-based coherence effects versus particle-based boundary scattering effects in the nanomesh. Researchers have fabricated and measured k of silicon nanomeshes[11]–[13], [99], [100], [105]–[107] with hole periodicities ranging from 10 µm down to 34 nm. Some of these experiments reported stronger k reductions than that predicted by BTE theories; these results were attributed to coherence effects[11]–[13], [106], [108]. In contrast, computational works by Jain *et al*.[109] and Ravichandran and Minnich[110] concluded that some of these experimental results could indeed be explained by particle based models without considering the coherence effects.

Underlying these various interpretations are differing views of the important coherence length scales in periodic structures. When periodicities are smaller than the dominant phonon wavelengths (λ), which are < 10 nm in silicon[111] for temperatures

T > 10 K, the particle models can break down[112]. When length scales are larger than inelastic mean free paths (*e.g*. due to Umklapp scattering, Λ_{U}), coherence effects can be safely neglected. The average Λ_{U} in bulk silicon at room temperature is experimentally found[113] to be ~300 nm, and calculations[3], [114] suggest that phonons with Λ_{U} between 100 nm and 10 μm carry ~70% of the heat at 300 K. The current question[13], [19], [108], [115] is whether phonon coherence effects are important when periodicities (here, pitch p) are large compared to λ but small compared to Λ_{U}. For example, studies have questioned whether coherence lengths that characterize the spatial extent of the wave packet[116], [117] are meaningful when wave packets can undergo multiple reflections in periodic structures[1], [118]. A common justification for applying the particle model in periodic nanostructures is that the interfacial roughness δ is comparable to or larger than the coherence length[1]. However, it has been recently proposed that phonon wave effects must be considered at room temperature even with disordered interfacial length scales $\delta \approx$1 nm in superlattices[19] or surface roughness $\delta \approx$2.5 nm in silicon nanomeshes[13].

An alternate, purely particle-based, explanation for the measured k reduction in the nanomesh is the phonon backscattering effect[110], [119]. As an illustration of backscattering, first consider an array of parallel nanowires, *e.g.* Figure 4-1 (right). The backscattering concept predicts that adding lateral bridging necks linking the nanowires into a nanomesh (Figure 4-1(left)) would reduce k because ballistic phonons are more likely to be scattered backwards when colliding with the nanomesh necks than with the nanowire walls, providing additional resistance to heat flow. This backscattering effect has recently been used to explain why k of a nanomesh could be lower than k of an equivalent nanowire array[110] even in the absence of coherence effects.

Although there are several mechanisms proposed to explain the k reduction in silicon nanomeshes, possible coherence (wave) and backscattering (particle) effects are often coupled, and previous experimental studies were unable to isolate the dominant mechanism. For example, experiments that change the hole size at fixed porosity[120], [121] or change the neck size at fixed hole spacing[105], [122] modify both the particle and wave predictions for k in nontrivial ways. A main difficulty in interpreting the experimental data is that even the particle model predictions are not well known; when searching for small coherence effects, accurate quantification of the boundary scattering is required. For example, it is not known whether periodic and aperiodic nanomeshes have the same boundary scattering mean free path.

In this chapter, I describe ray tracing simulations to quantify incoherent phonon boundary scattering in silicon nanomeshes. I describe the thermal conductivity modeling, introduce the computational method, present validation studies, and compare the simulations with experiments performed by my collaborators. These ray tracing simulations reveal that the particle model predicts that periodic and aperiodic silicon nanomeshes have the same k (within 1% numerical error), while backscattering reduces k for short-pitch nanomeshes. The ray tracing predictions are in excellent agreement with k measurements performed between T =14-325 K for nanomeshes with pitches ranging from 100-1000 nm. This agreement indicates that phonon coherence effects are not necessary to describe thermal transport in the regime where the nanomesh pitch is

greater than λ but smaller than Λ_{U} and the surfaces scatter phonons diffusely. Instead, we find that the particle backscattering effect explains the experimental trends, elucidating the mechanism of heat trantsport in silicon nanomeshes.

4.2 Modeling heat conduction in silicon nanomeshes

In this section, we consider both macroscopic porosity effects and microscopic boundary scattering effects on the thermal conductance G and thermal conductivity k These quantities are related by

$$G = \frac{kfwt}{L}, \tag{1}$$

where L and w are the length and width of the suspended silicon nanomesh, t is the thickness, and f is the bulk porosity correction factor which describes the reduction in conductance for bulk porous materials. We choose to define k such that when all length scales are large compared to Λ_{U}, k recovers the handbook value for silicon, regardless of the geometry or porosity. Using this definition, any differences in k for our nanomeshes are due solely to sub-continuum effects, and it is meaningful to make direct comparisons between the thermal conductivity of the nanomeshes and the thermal conductivity of fully dense nanostructures such as thin films or nanowires.

4.2.1 Macroscopic effect: porosity factors

Even in the absence of sub-continuum size effects, introducing porosity decreases G. To quantify this porosity correction factor f, we performed FEM simulations using COMSOL software for arrays of square holes and circular holes. The porosity correction factor can be readily obtained by the ratio of G for mesh structures to G of completely filled structures, *i.e.* a homogenous plate with the same overall external dimensions but no holes. We find that the FEM simulation results for both square and circular holes with the experimental dimensions are in excellent agreement (<4% error) with the 2D Maxwell-Garnett effective medium model (EMM)[123] $f = (1-\phi)/(1+\phi)$, where ϕ is the porosity. We also computed f for various aspect ratio rectangular holes using COMSOL. These FEM simulation results for rectangular holes agree well with a 2D EMM suitably generalized for aligned elliptic cylinders[124], $f = (1-\phi)/(1+\phi*(p_y/p_x))$. However, because of the microscopic boundary scattering effects, the thermal conductance will be further reduced beyond the predictions of the EMM. We quantify this reduction using ray tracing.

4.2.2Microscopic modeling of phonon transport

The BTE particle model for the thermal conductivity under the common isotropic dispersion approximation is[125]

$$k = \frac{GL}{fwt} = \frac{1}{3}\int C\mathrm{v}\Lambda\, d\omega, \tag{2}$$

where ω is the phonon frequency, C is the volumetric modewise heat capacity, v is the group velocity, and Λ is the mean free path. We choose an isotropic Born-van Karman (BvK) sine-type dispersion approximation $\omega = \omega_0 \sin\left(\frac{\pi}{2}\frac{\kappa}{\kappa_0}\right)$, where κ_0 is the cutoff wavevector set by the atomic number density and ω_0 is determined by the

weighted speeds of sound such that $k(T)$ is exact in the low T boundary scattering limit[126]. Though silicon's dispersion is not isotropic, k of bulk and nanostructured silicon is often successfully modeled with an assumed isotropic dispersion[3], and the isotropic dispersion approximation is essential in interpreting the ray tracing results. The LA and TA branches are lumped into one effective branch. Our previous studies showed that either an isotropic full dispersion model that accounts for six independent phonon branches[127] or the Born von Karman (BvK) model with lumped branches [3], [126] adequately describes phonon transport in bulk and nanostructured silicon.

Different choices of dispersion can lead to different predictions of k reduction due to boundary scattering. For example, for the mesh with n=30 nm, t= 90 nm, and $p_x = p_y$ =100 nm, the BvK dispersion model for the pure silicon predicts around a 20% larger room temperature conductivity reduction than predicted by one first-principles approach[3]. The BvK model was selected because its predictions agree well with previous measurements of silicon nanostructures[3] from 20 to 300 K, and reduces to give the correct $k(T)$ in the boundary scattering regime by construction.

We use the Matthiessen's rule $\Lambda^{-1} = \Lambda_{\mathrm{B}}^{-1} + \Lambda_{\mathrm{I}}^{-1} + \Lambda_{\mathrm{U}}^{-1}$ to combine boundary, impurity, and Umklapp scattering, respectively. The Umklapp scattering was determined by a least-squares fit[3] of experimental $k(T)$. We use the Umklapp scattering rate $\tau_{\mathrm{U}}^{-1} = P\omega^2 T \exp\left(-\frac{C_{\mathrm{U}}}{T}\right)$ with $P = 1.53 * 10^{-19}$ sK^{-1} and $C_{\mathrm{U}} = 144$ K. The impurity scattering rate for the literature silicon was $\tau_{\mathrm{I}}^{-1} = C_{\mathrm{I}}\omega^4$ with $C_{\mathrm{I}} = 2.54 * 10^{-45}$ s^3. We will fit the impurity scattering rates to the experimental data, since C_{I} depends on the doping level. Because *n* and *t* are much smaller than the important Λ_{U} in silicon at our experimental temperatures[3], the particle model predicts that boundary scattering dominates Λ. Analytical results for Λ_{B} are known for simple geometries such as nanowires[128], [129], but Λ_{B} is generally unknown for complicated structures such as the nanomesh[105], [109]. To rigorously determine Λ_{B} we use a ray tracing technique[130].

4.2.3 Ray tracing calculation of boundary scattering

From the Landauer-Büttiker formalism[131], [132], the thermal conductance *G* is

$$G = \frac{A}{4}\int C v \langle\tau\rangle d\omega, \tag{3}$$

where $\langle\tau\rangle = \int_{\phi=0}^{2\pi}\int_{\mu=0}^{1}\int_A \tau(\phi,\mu,A)\mu\, d\mu\, d\phi\, dA\, /\pi A$ is the average transmission coefficient, μ =cosθ is the directional cosine, and $A = wt$ is the cross-sectional area. Comparing the Landauer-Büttiker and the BTE models,

$$\frac{f\Lambda}{L} = \frac{3}{4}\langle\tau\rangle. \tag{4}$$

We use a ray tracing method with Monte Carlo integration to find the average transmission coefficient $\langle\tau\rangle$ for the 3D nanomesh structures considering only boundary scattering. A phonon is launched at the device-lead contact with a randomly selected initial position. The azimuthal angle of injection is also uniformly random, while the polar angle is sampled from a $\cos\theta \sin\theta$ weighted distribution[133]. The phonon is propagated along a straight line to the nearest intersecting surface, and a uniform

random number is drawn to determine the reflection angle. If the surface specularity parameter P is less than (greater than) the random number, then the particle is reflected diffusely (specularly). The ray tracing continues until the phonon exits the computational domain by reaching either thermalizing contact. For all results presented, at least $3*10^5$ phonons were launched, and $\langle\tau\rangle$ is calculated as the number of transmitted phonons divided by number of total phonons injected.

As a measure of uncertainty, the standard deviations of $\langle\tau\rangle$ and thus *k* are estimated following a common subsampling method[134]. The phonons are uniformly distributed into J subsamples (here, $J = 40$). Each of these subsamples is now regarded as an independent measurement, and the difference between these subsamples provides an estimate of the variance of the total transmission coefficient $\langle\tau\rangle$. The mean transmission coefficients of the *n* subsamples $\langle\tau_n\rangle$ are calculated, and the variance σ^2 of $\langle\tau\rangle$ is found as

$$\sigma^2 = \frac{1}{J(J-1)}\sum_{n=1}^{J}[\langle\tau_n\rangle - \langle\tau\rangle]^2. \quad (5)$$

The computational domain is determined based on the symmetry of the structure. We take the global heat flow direction to be in-plane in $\hat{x}$. Since the experimental sample widths are much larger than the pitch, we consider only one unit cell in the in-plane direction $\hat{y}$ and apply fully specular boundary conditions on the periodic unit cell in $\hat{y}$ due to the mirror symmetry. The top and bottom surfaces of the film form two additional walls of the domain in the xy planes. The neck n between pores along $\hat{x}$ and $\hat{y}$ is always identical. When comparing the periodic and aperiodic mesh, we explicitly place distinct mesh pores along the length L of the device. For the aperiodic structure, n and p_y are held constant while p_x is varied randomly and uniformly by up to $\pm 20\%$ of the nominal spacing by drawing a different random number for each pore. We perform multiple trials with different aperiodic structures to achieve ensemble statistics. Figure 4-2 shows an example ray tracing trajectory in a periodic nanomesh.

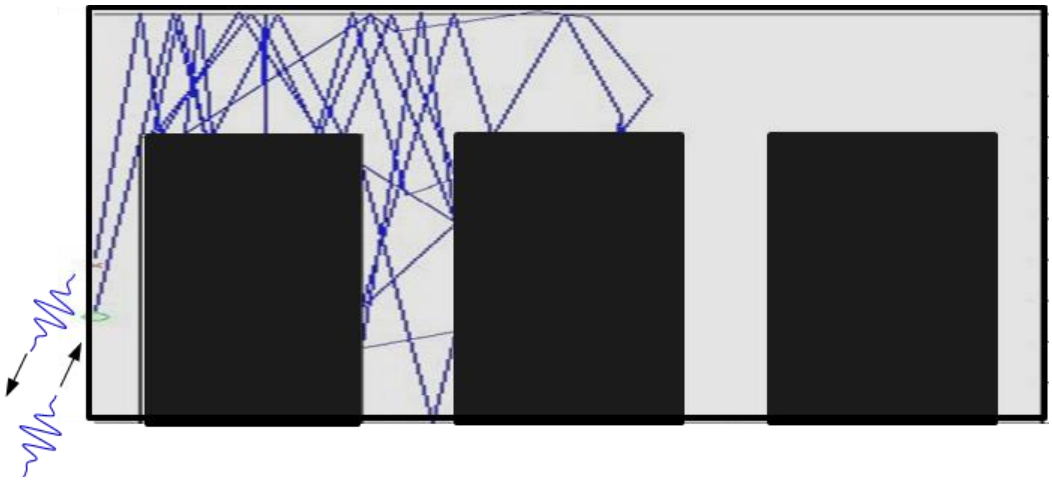

Figure 4-2: Example phonon trajectory in nanomesh. The blue lines indicate the phonon's ballistic transport. The phonon scatters diffusely off of the etched holes and the top and bottom of the nanomesh out of the page. The specular reflections account for the mirror symmetry of the nanomesh. This phonon did not transmit.

For simulations where all structures of interest have a discrete translational symmetry along $\hat{x}$, we populate only one unit cell of surfaces to save computational time calculating the nearest collision. The yz mirror symmetry plane at the midpoint of the unit cell in $\hat{x}$ allows us to convert the periodic boundary condition to specular boundary conditions at $x = 0$ and $x = p_x$. We track the total distance the phonon has travelled along L and terminate the simulation when the phonon reaches either of the device-lead contact planes.

A characteristic behavior of diffusive transport is a mean free path Λ that saturates for long L. The mean free path Λ calculated from the transmission coefficient $\langle\tau\rangle$ describes the combined effects of diffusive nanomesh boundary scattering and a length-independent ballistic resistance (which can be represented through a transmission coefficient τ_{ball}) that depends on the configuration of the device-contact connection. To find the intrinsic Λ_{B}, defined as $\lim_{L\to\infty}(\Lambda)$, from finite-$L$ simulations, we follow the technique of previous works[135] and sum the ballistic and diffusive scattering in parallel in a Matthiessen's rule-type approximation, resulting in

$$\frac{L}{\Lambda} = \frac{1}{\tau_{\mathrm{ball}}} + \frac{L}{\Lambda_{\mathrm{B}}}. \qquad (5)$$

We calculate Λ as a function of L and use a weighted least-squares fitting to Eq. 5 to determine Λ_{B}. If ballistic behavior is important even for large L, as is the case for transport in a fully specular nanowire or a diffuse thin film in the in-plane direction in the absence of Umklapp scattering[4], then Λ does not converge with L ; this is not the case here. The length-convergence procedure is illustrated in Figure 4-3, showing that the periodic and aperiodic nanomeshes have the same boundary scattering mean free path.

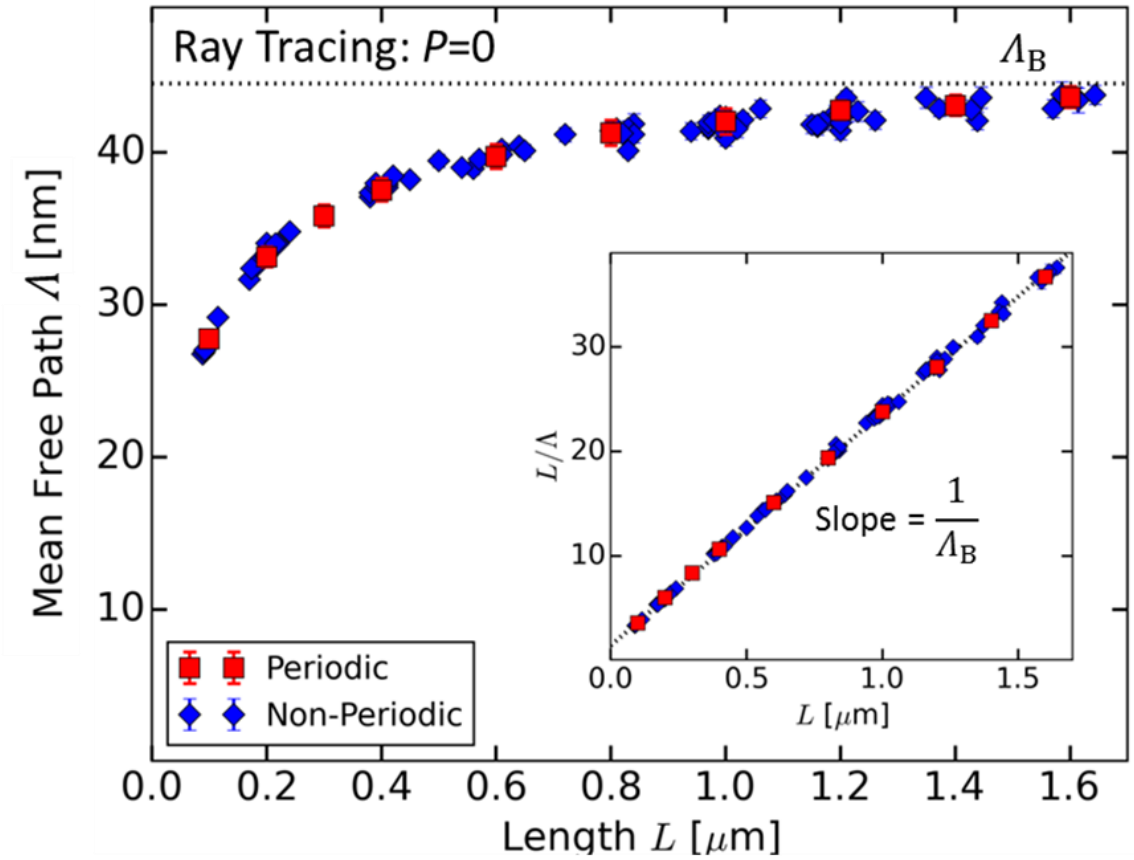

Figure 4-3: Ray tracing length convergence study. Ray tracing results for periodic and aperiodic nanomeshes show Λ as a function of L for fully diffuse surfaces. Error bars indicate the standard error. The dotted line is the extrapolated long-length limit Λ_B , which is found from the slope of L/Λ against L (inset). The ray tracing simulations show that the periodic and aperiodic structures have the same thermal conductivity.

4.2.4 Validating the ray tracing against numerical BTE solution

We have validated the ray tracing code against analytical solutions for Λ_B, including nanowires[130] and cross-plane transport in diffuse superlattices[136]. Here, we compare the ray tracing predictions with previously published BTE simulation results for two nanomeshes[110]. The literature results were obtained using a variance-reduced Monte Carlo (VRMC) algorithm to solve the BTE while including both boundary and intrinsic scattering in the 3D diffuse nanomesh. We performed ray tracing simulations using the same dimensions and specularity to obtain Λ_B for a mesh with square holes ($p = 34$ nm, $n = 23$ nm, $t = 22$ nm) and a mesh with circular holes ($p = 34$ nm, diameter d =11 nm, $t = 22$ nm). For the purpose of this comparison only, we use the same Si [100] dispersion and intrinsic scattering times as in the original work[110] to make a fair comparison between numerical predictions. We note that the plotted quantity for the mesh in the reference[110] is $k_{\text{eff}} = kf = GL/A$, and we use the EMM result $f = (1-\phi)/(1+\phi)$, which agreed with our FEM analysis for both circular and square holes.

As shown in Figure 4-4, the ray tracing and the VRMC predictions for $k_{\mathrm{eff}}(T)$ show excellent agreement within 3% for all temperatures for the circular and square holes, validating our ray tracing code. The small remaining discrepancy between techniques may be due to our use of Matthiessen's rule or slight differences in the dispersion fits. A benefit of using a ray tracing approach as compared to solving the BTE with a known mean free path spectrum as an input is that in the ray tracing, the material-independent Λ_{B} is determined once and for all for a given geometry and surface specularity. Once Λ_{B} is found from the ray tracing, different isotropic dispersions, intrinsic scattering rates, or temperatures are then easily incorporated using Matthiessen's rule without requiring the additional computationally expensive simulations of a BTE solver. We note that Λ_{B} could also be found by solving the BTE assuming that all phonons have the same mean free path. In addition, detailed BTE solvers can also obtain the full temperature profile in addition to the heat flux

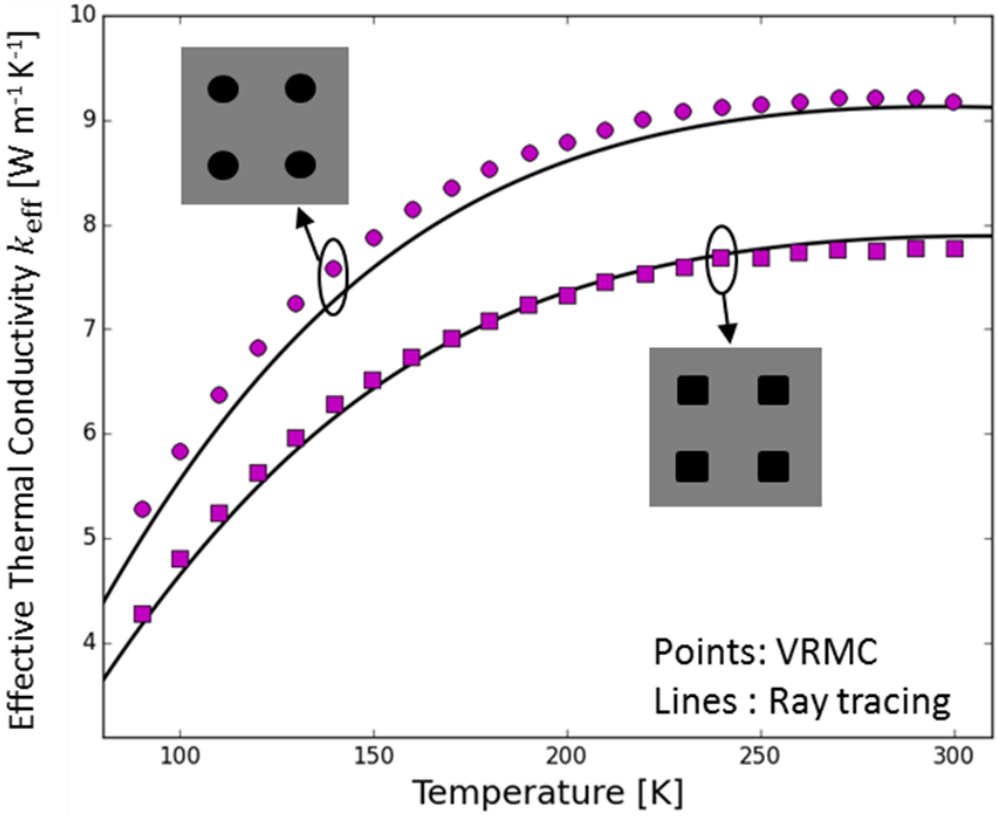

Figure 4-4 : Ray tracing validation. Validating the ray tracing predictions (lines) against published variance-reduced Monte Carlo (VRMC) simulations[110] for nanomeshes with square and circular holes. The computational approaches agree within 3% for all temperatures for both the square and circular holes. For this comparison only, we use the same dispersion and bulk scattering parameters as the reference[110].

4.2.5 Testing Matthiessen's rule

We use Matthiessen's rule to combine ray tracing boundary scattering with frequency dependent intrinsic scattering when predicting $k(T)$. To test the validity of Matthiessen's rule for these structures, we also performed several ray tracing simulations that incorporate Umklapp scattering as well as boundary scattering. After a phonon is input to the domain or undergoes a scattering event, a free path is determined by drawing a random number ζ from a uniform distribution between 0 and 1. The phonon free path is then $-\Lambda_{\mathrm{U}}\ln(\zeta)$, where Λ_{U} is the Umklapp scattering mean free path. If the free path is smaller than the distance to the next surface, an Umklapp scattering event occurs at the corresponding point within the domain, with the phonon's outgoing direction uniformly random among 4π sr.

Figure 4-5 compares the calculated Λ from the simulations explicitly including both Umklapp and boundary scattering with the predictions from Matthiessen's rule, for different input values of $\Lambda_{\mathrm{B}}/\Lambda_{\mathrm{U}}$. Both the *AR*=1 and *AR*=8 structures have $n = 30$ nm, t =90 nm, p=100 nm, and L =0.8 μm. The discrepancy between the points that include the coupled scattering and the dashed line showing the Matthiessen's rule calculation is never larger than 7%, indicating that using Matthiessen's rule is not a major source of error in the high temperature analysis. Similarly good agreement between Matthiessen's rule and rigorously coupled scattering in nanostructures has also been observed in previous works[3], [130].

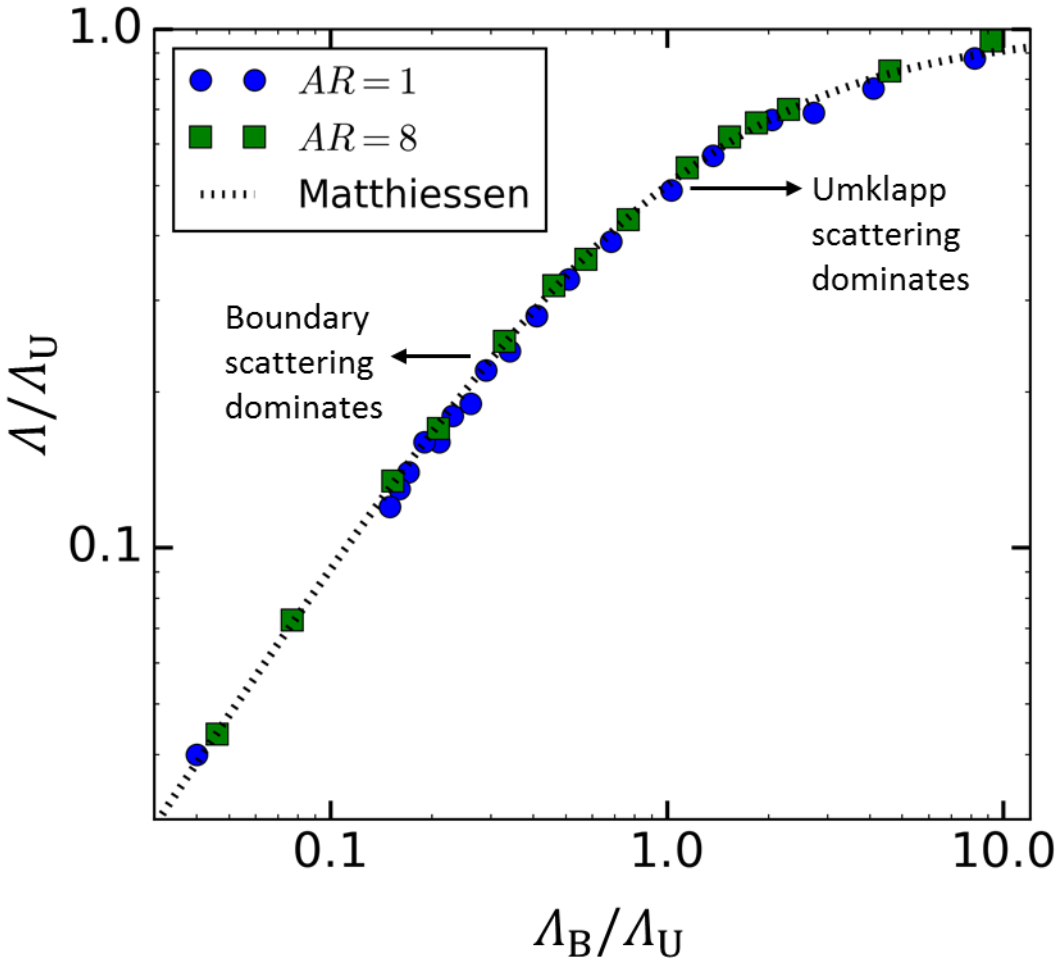

Figure 4-5: Testing Matthiessen's rule using ray tracing. Points are ray tracing simulations explicitly including both Umklapp scattering and diffuse boundary scattering, while the dashed line is the analytical Matthiessen's rule prediction for the given boundary scattering Λ_B and Umklapp scattering Λ_U. The very good agreement (7% maximum error for these dimensions of n =30 nm, t =90 nm, p =100 nm and L =0.8 μm for pitch aspect ratio *AR*=1 and *AR*=8 nanomeshes) indicates that Matthiessen's rule accurately describes the combined scattering processes for the silicon nanomeshes.

4.3 Comparison of ray tracing with experiment

Here, I compare the ray tracing predictions against experiments performed by my collaborators, Jaeho Lee and Woochul Lee. I also compare the ray tracing predictions to previous silicon nanomesh experiments[13].

4.3.1 Investigating coherence in periodic and aperiodic nanomeshes

We compare a periodic nanomesh (Figure 4-6**a**) of 100 nm pitch p_x to an aperiodic nanomesh (Figure 4-6**b**) of variable p_x ranging from 80 nm to 120 nm along the direction of heat flow $\hat{x}$. The aperiodic nanomesh was constructed to break the periodicity yet have the same porosity and average p_x of 100 nm. Other dimensions including the transverse pitch p_y, neck between holes n, and membrane thickness t were kept the same between the nanomesh structures. Figure 4-6**c** shows the measured

$k(T)$ for three samples. The thermal conductivities of the periodic and the aperiodic samples are the same within experimental uncertainty (estimated at 6 %) over the entire temperature range of 14-325 K. Identical k from the periodic and aperiodic nanomeshes indicate that coherence effects are not important for heat transfer at these temperatures. In addition, a clear T^3 trend is observed at low T, consistent with the classical diffuse boundary scattering theory. The measured k at 300 K is an order of magnitude smaller than the bulk silicon handbook value, demonstrating the importance of boundary scattering in reducing k. The measured k is also more than a factor of two smaller than literature measurements of in-plane k of suspended silicon membranes of comparable thickness[10], indicating that the mesh structuring further reduces k of the thin membranes.

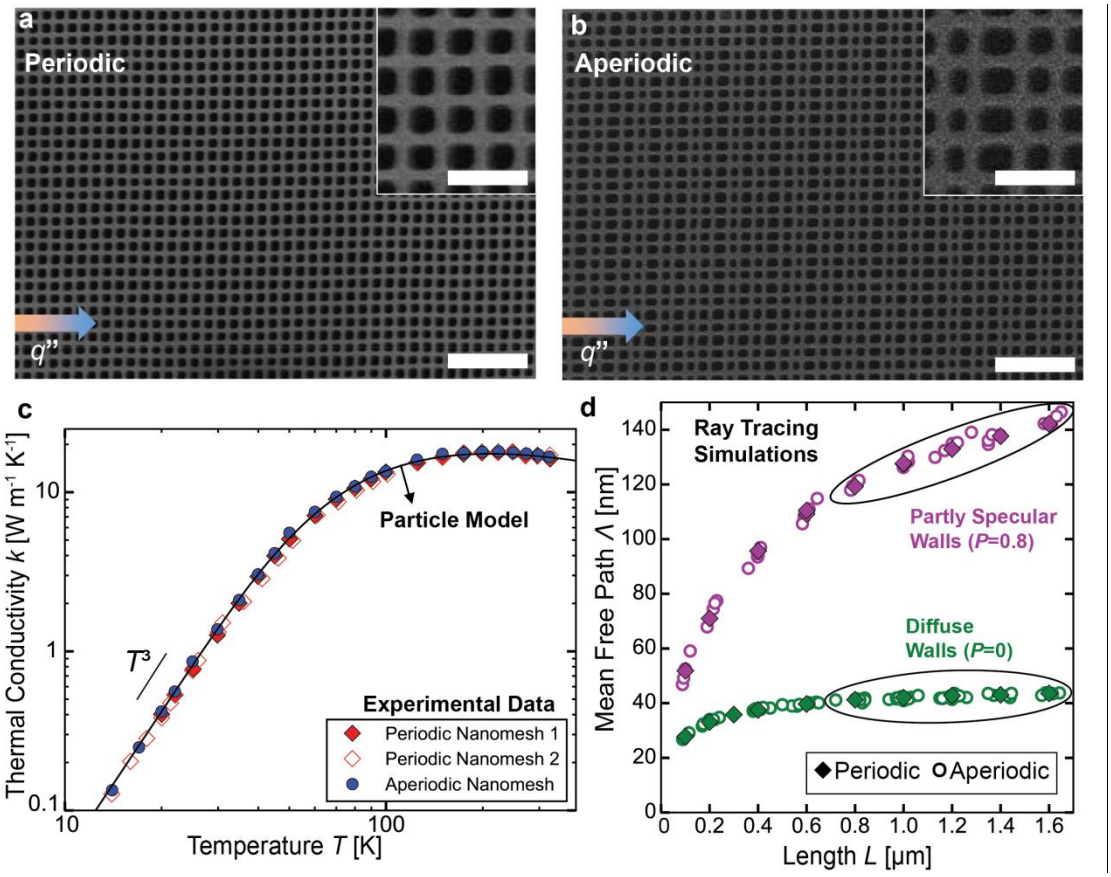

Figure 4-6: Isolating coherence effects with periodic and aperiodic nanomeshes. (**a**) SEM image of a periodic Si nanomesh with a controlled periodicity of $p_x = p_y = 100$ nm. (**b**) SEM image of an aperiodic Si nanomesh, in which the pitch in the transport direction p_x varies by up to ±20% (80 – 120 nm). Scale bars in **a,b** 200 nm (inset) and 600 nm (main). (**c**) Experimental data (points) and the BTE particle model with diffuse surfaces (line) show excellent agreement for $k(T)$ of two periodic and one aperiodic nanomeshes. The very similar k between the 3 samples at all T indicate negligible coherence effects for thermal transport in silicon nanomeshes for $p \geq 100$ nm and $T > 14$ K. (**d**) Ray tracing simulation results for the mean free path Λ as a function of sample length L considering boundary scattering with fully diffuse ($P = 0$) and partly specular ($P = 0.8$) surfaces show that the BTE particle model predicts equal k for the periodic and aperiodic meshes. The P=0 long-length limit, $\Lambda_B = 44.2 \pm 0.5$ nm, was used in the particle model calculation in **c**.

Figure 4-6**d** shows the ray tracing simulations for the mean free path Λ as a function of length L for periodic and aperiodic nanomeshes. All surfaces were taken to be either fully diffuse ($P = 0$) or partly specular ($P = 0.8$). Λ of the periodic and the aperiodic nanomeshes are identical within the simulation uncertainty ($\pm$1%) for both specularities shown here. The BTE model therefore predicts equal conductivity for our periodic and aperiodic nanomeshes, just as observed in experiments. In addition, the experimental results in Figure 4-6**c** agree well with the particle model using the $P = 0$ boundary scattering value. To find the impurity scattering rates required for the particle model (which have only a mild influence even at high temperature), we performed a best fit to the periodic and aperiodic experimental data, which is shown in Figure 4-6**c** as the particle model. We obtain an impurity scattering constant value of $C_{\mathrm{I}} = 1.96 * 10^{-44}$ s^3, which is a factor of 10 larger than the literature value. This larger phonon impurity scattering rate appears reasonable given the literature silicon room temperature resistivity was 2000 Ω-cm (p-type)[137] and our boron-doped silicon resistivity is 14-22 Ω-cm, indicating larger dopant concentrations and scattering rates for our silicon. The impurity scattering modifies k by at most 15% at T=300 K, and for all T below 60 K the impurity correction to k is less than 5%.

In Figure 4-7, we show that for all $P < 0.9$, the periodic conductivity k_{p} and aperiodic conductivity k_{ap} remain equal within simulation error. For very large specularities ($P > 0.9$), $k_{\mathrm{p}}$is significantly larger than k_{ap}. We attribute this result to a "critical angle" effect: for the periodic structures, phonons incident at critical angles can be specularly reflected forward through the nanomesh for many periods before being backscattered, as illustrated in the specular cartoon in Figure 4-7. Introducing aperiodicity can backscatter these critical angle phonons due to the shifted positions of the holes. Of course, adding the aperiodicity can also cause some phonons who were previously backscattered in the periodic structure to now transmit; however, the increased Λ for periodic structures at $P = 1$ indicates that the net effect of the aperiodicity is to increase backscattering in this scenario.

These ray tracing results reveal that at very low temperature (<5 K) where the dominant phonon wavelengths are large compared to surface roughness and surfaces are well approximated as fully specular, the particle model also predicts that k_{p} and k_{ap} can differ. Clearly, this has nothing to do with coherence effects on the phonon dispersion relation. Thus, in this regime great care must be taken to properly identify the coherent contributions to thermal transport, since differences between k_{p} and k_{ap} cannot be simply attributed to wave effects. Lastly, we note that the experiments are well described by the $P = 0$ ray tracing predictions. Such fully diffuse behavior in our temperature range is expected from specularity model predictions such as Ziman's commonly used expression[138] assuming surface roughness >1 nm, as well as previous measurements of silicon nanostructures[10], [139].

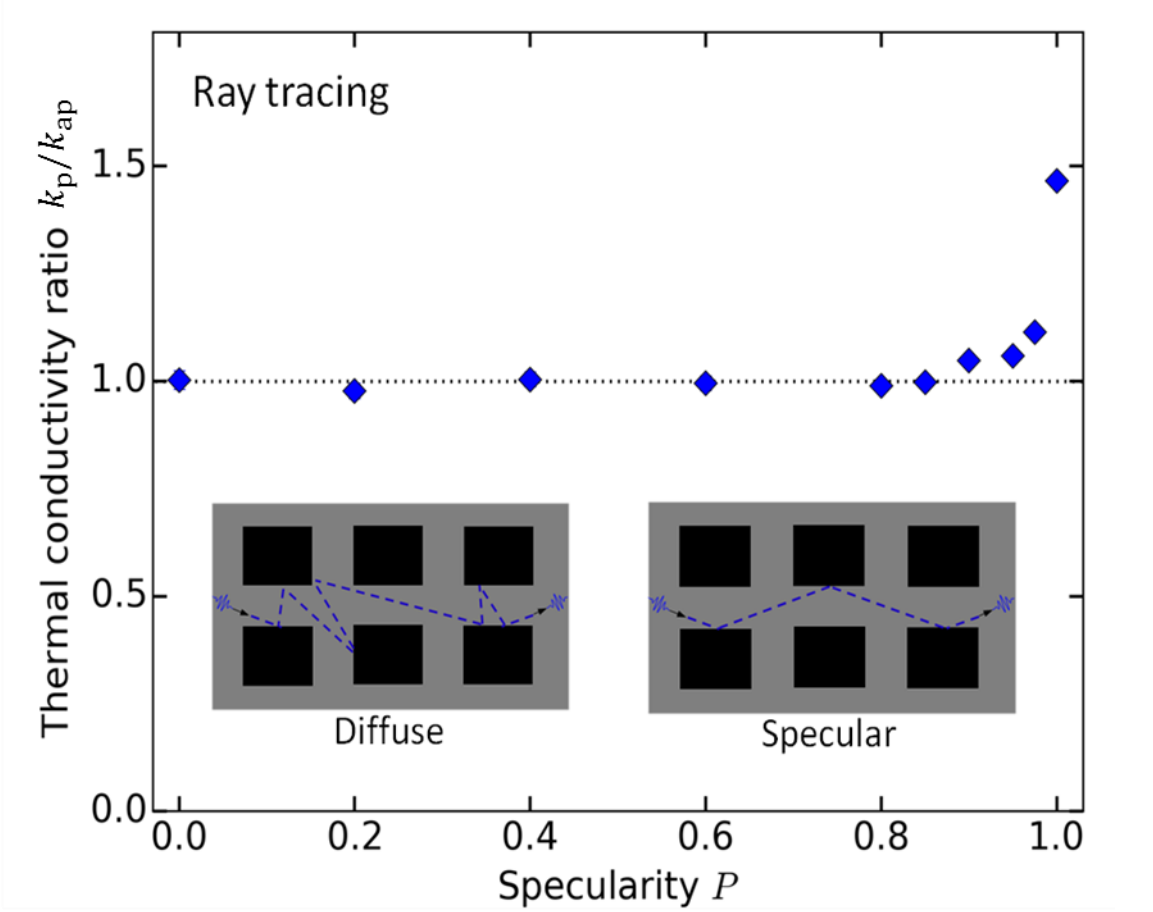

Figure 4-7 : Periodic/aperiodic thermal conductivity ratio k_p/k_{ap}. Ray tracing simulations were performed in the boundary scattering regime as a function of specularity P for nanomeshes with the same dimensions as in Figure 4-6 and $L = 1.6$ μm. For $P \leq 0.85$, the periodic and aperiodic nanomeshes have the same k within the r of the ray tracing (standard deviation ±1 %). For larger specularities, the periodic conductivity is larger than the aperiodic conductivity, which we attribute to a "critical angle" phenomena. The experiments are modeled using the *P*=0 results.

Based on the combined ray tracing and experimental analysis, we conclude that coherence effects are not important for understanding thermal transport in silicon nanomesh structures with periodicities down to 100 nm and *T* down to 14 K. More generally, this experiment indicates that the wave nature of phonons does not need to be considered to describe transport in the regime where $\lambda \ll p \ll \Lambda_U$ and $\lambda \sim \delta$.

4.3.2 Comparison with previous experiment

A recent experimental work[13] measured k of silicon nanomeshes with circular holes (p=1100 nm, t=366 nm, n=250 nm, and various diameters) and suggested that coherence effects arising from the mesh periodicity are important for heat transfer at 300 K. Here, we use ray tracing simulations to find rigorous incoherent model predictions for these geometries assuming diffuse scattering, and find that the particle model also predicts the experimental trend previously attributed to phonon wave effects.

The experiment[13] was designed to manipulate the phononic band structure by interpenetrating an additional periodic array of small circular holes (radius r_s=102.5 nm) within the larger periodic mesh. The work calculates a modified dispersion relation for sub-10 GHz phonons due to changes in this secondary periodicity for five meshes with different interpenetrated arrays. We note that 10 GHz is relatively low energy compared to the characteristic thermal frequency at 300 K, estimated as $f_{\mathrm{th}} = \frac{k_{\mathrm{b}}T}{h} \approx 6{,}250$ GHz, where h is Planck's constant and k_{b} is Boltzmann's constant. Two trends in the experimental results were interpreted as suggestive of room temperature coherence effects. First, the measured k_{mesh} normalized by a measured k_{tf} of a film of the same thickness was smaller than a BTE model prediction using an assumed $\Lambda_{\mathrm{B}} = n$. Second, the experimental k_{mesh} trend showed a stronger decrease with increasing porosity than predicted by a BTE model with constant Λ_{B} between structures. A crucial approximation in the reported BTE analysis is that Λ_{B} was essentially unchanged between the different meshes even though additional holes have been introduced.

We performed ray tracing simulations using the geometries and dimensions of the five reported mesh structures. Contrary to the previous assumption[13], we find that Λ_{B} decreases monotonically with the number of additional small holes, and that the decrease in Λ_{B} from the original supercell mesh and the "1x1" mesh with the highest density of small holes is around 20% (from $\Lambda_{\mathrm{B}} = 320$ nm to $\Lambda_{\mathrm{B}} = 256$ nm). We use these Λ_{B} values as inputs to the BvK model using Matthiessen's rule with the same silicon scattering parameters used in the main text here, to find k_{mesh} at 300 K using our definition of k from Eq. (1). All surfaces are taken fully diffuse. To focus on the BTE model predictions for the change in k_{mesh} with additional holes, we normalize the simulation and experimental values by their respective supercell conductivity k_{SC}. We present results using the BvK model for clarity since the six different models analyzed in Yang and Dames[3] yield $k_{\mathrm{mesh}}/k_{\mathrm{SC}}$ that differ by no more than 4%.

Figure 4-8 shows $k_{\mathrm{mesh}}/k_{\mathrm{SC}}$ as measured in the experiment[13] and as predicted here from the ray tracing and BTE model. The labeling notation follows the original work, and the experimental fractional percentage uncertainty in $k_{\mathrm{mesh}}/k_{\mathrm{SC}}$ is taken to be the same as the reported percentage uncertainty in $k_{\mathrm{mesh}}/k_{\mathrm{tf}}$. In the BTE model, the reduced k_{mesh} with increasing small hole density is due exclusively to increased boundary scattering because the BTE model uses bulk dispersion and bulk intrinsic scattering. This result shows that the BTE model predicts the observed experimental trend in $k_{\mathrm{mesh}}/k_{\mathrm{SC}}$ once boundary scattering is rigorously considered, without any appeal to coherent effects.

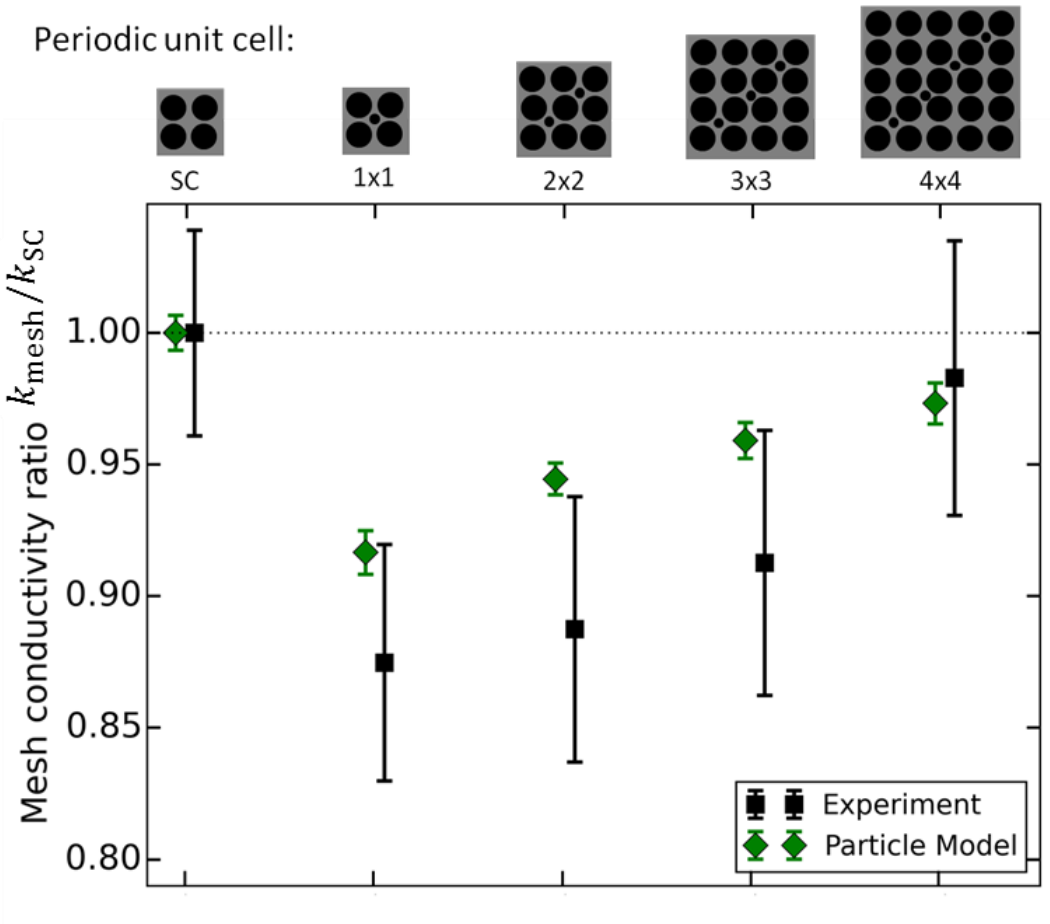

Figure 4-8 : Particle model comparison with previous experiment. Particle BTE modeling results are compared to previously reported measurements[13] of thermal conductivity k_{mesh} for structures with different interpenetrating small hole arrays, normalized to the value of the original supercell k_{SC}. Ray tracing simulations predict that adding the interpenetrating small holes decreases Λ_{B} and k_{mesh}, in contrast to the previous constant-Λ_{B} assumption[13] which predicts a constant k_{mesh} (dotted line). The experimental trend is well explained by the BTE model without any modified dispersion or scattering due to coherence effects.

4.3.3 Investigating backscattering in variable pitch nanomeshes

Figure 4-9**a** shows SEM images of silicon nanomeshes with pitches p_x by p_y of 100 by 100 nm, 200 by 100 nm, and 1000 by 100 nm. In the limit of large p_x, the nanomesh resembles a nanowire array. Comparing k of samples with different p_x directly tests the backscattering concept by controlling the number of possible backscattering centers at the bridging necks. The measured thermal conductivity $k(T)$ is shown in Figure 4-9**b**. For all T, k decreases as the aspect ratio $AR = p_x/p_y$ decreases, as predicted by the backscattering concept. Significantly, this geometric dependence is in contrast to the bulk theory prediction of geometry-independent k *(*recall that k has already been corrected for bulk porosity effects using the FEM f factors). Figure 4-9**b** also shows the BTE predictions for $k(T)$ of the nanomeshes using ray tracing results with diffuse surfaces. The particle model is in good agreement with the experimental data without using additional fitting parameters.

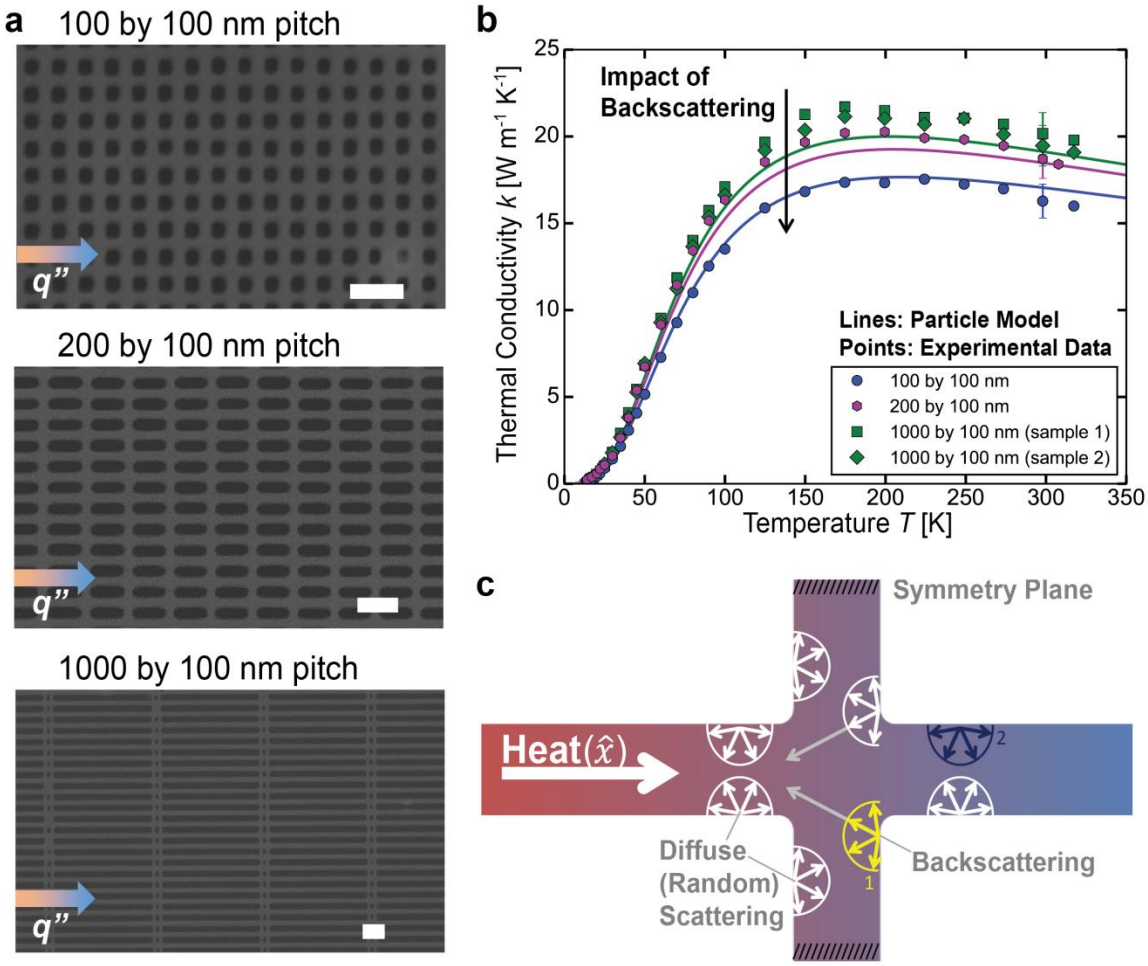

Figure 4-9: Investigating backscattering effects with short and long pitch nanomeshes. (**a**) SEM images of silicon nanomeshes with varying pitch size (100 nm – 1 µm) along the direction of heat flux (*q"*). Scale bars, 200 nm. (**b**) Experimental results and particle model predictions for *k(T)* of four samples show that decreasing the pitch decreases *k*, as predicted by the backscattering effect. Error bars represent the experimental uncertainty. The particle model contains no free parameters, and all surfaces are fully diffuse. (**c**) Illustration of backscattering for diffuse surfaces. The neck intersection backscatters a larger percentage of incident phonons that the nanowire-like boundaries parallel to the global *q"*, which leads to increased backscattering from short pitch nanomeshes. For example, 100% of the phonons are backscattered at point 1 (indicated in yellow) while the backscattering percentage is only 50% at point 2 (indicated in dark blue).

4.4 Ray tracing simulations of the backscattering effect

We now dive deeper into the backscattering effect with additional ray tracing simulations. We define backscattering as a boundary scattering event that changes the $\hat{x}$ velocity component from positive to negative for a phonon originally emitted from the hot terminal, where $\hat{x}$ is aligned along the global temperature gradient. Backscattering reflects these phonons travelling in $+\hat{x}$ back towards the hot terminal in $-\hat{x}$, providing resistance to heat transfer. Figure 4-10**a** plots the fraction of boundary scattering events resulting in backscattering for phonons emitted from the hot terminal travelling in $+\hat{x}$

for meshes with varying p_x, fixed $p_y = 100$ nm, $n = 45$ nm, $t = 60$ nm, and either $P = 0$ (left axis) or $P = 0.8$ (right axis). Decreasing the aspect ratio $AR = p_x / p_y$ increases the backscattering fraction, and for large aspect ratios the backscattering fraction approaches the nanowire limit of $(1 - P)/2$. Figure 4-10**b** shows how the resulting long-length boundary scattering mean free path Λ_B decreases as the backscattered fraction increases. For diffuse scattering, $AR > 5$ nanomeshes have very similar Λ_B to an equivalent diffuse nanowire of rectangular cross section $n \times t$ [129]. However, the Λ_B for partly specular nanomeshes remains below the equivalent partly specular nanowire limit, indicating that the increased backscattering in partly specular nanomeshes is still important for thermal transport even at $AR = 10$.

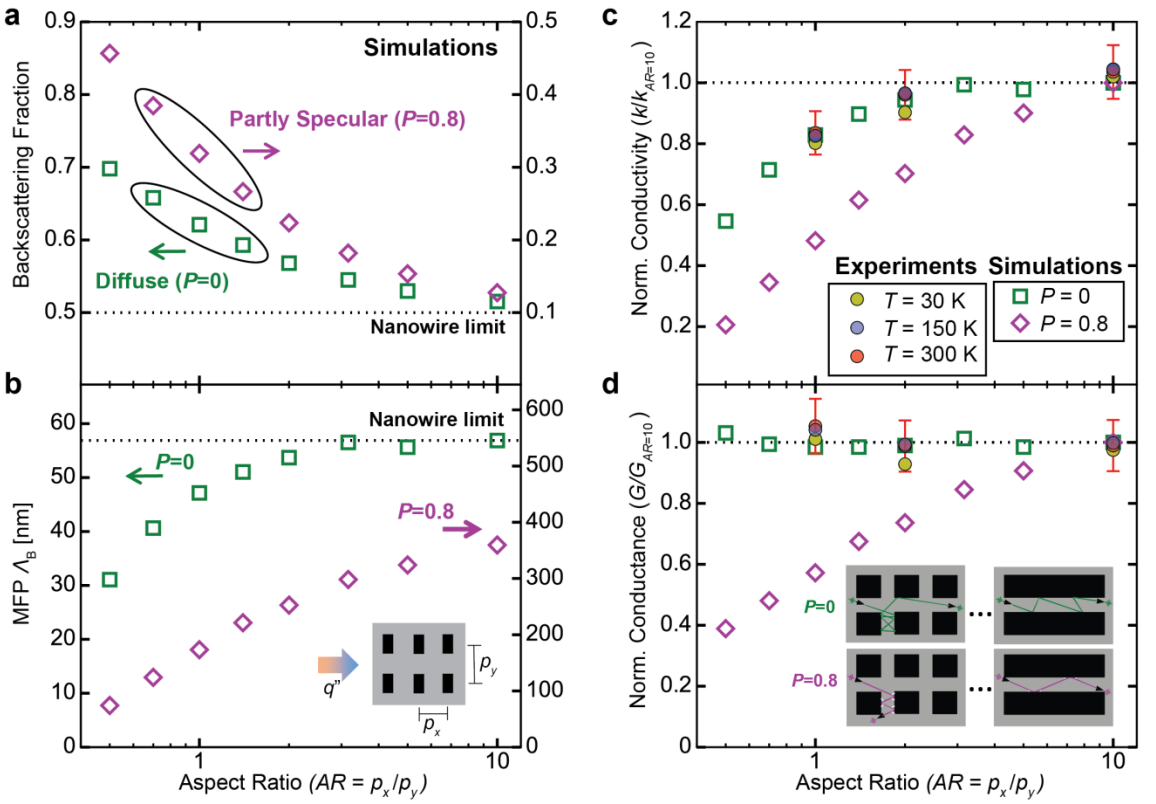

Figure 4-10: Influence of backscattering. Ray tracing simulations investigate phonon backscattering for nanomesh structures with varying pitch aspect ratios $AR = p_x/p_y$, comparing diffuse ($P = 0$) and partly specular ($P = 0.8$) surfaces. (**a**) Increasing AR decreases the backscattering fraction, which quantifies the backscattering effect. For large aspect ratios, the backscattering fraction approaches the nanowire limit of $(1 - P)/2$ (dashed line). (**b**) Consistent with the backscattering effect mechanism, the boundary scattering mean free path Λ_B decreases as the backscattering increases. (**c**) Normalized conductivity $k/k_{AR=10}$ from ray tracing simulations (empty points) and experiments at 3 different temperatures (filled points, taken from Figure 4-9**b**) show decreasing *k* with increased backscattering (*i.e.*, with smaller *AR*). (**d**) The normalized conductance $G/G_{AR=10}$ is surprisingly independent of aspect ratio for diffuse surfaces, which we attribute to a multiple backscattering effect (inset, green). If the surfaces are partially specular, the backscattering does reduce G. Panels **c,d** show that the experimental normalized conductivity and conductance results are consistent with diffuse scattering simulations.

We compare the ray tracing results with experiments in Figure 4-10**c**, where the normalized conductivity $k/k_{AR=10}$ from ray tracing and normalized experimental values from Figure 4-9**b** at three temperatures show good agreement with the diffuse scattering predictions. Likewise, we plot a normalized conductance $G/G_{AR=10}$ in Figure 4-10**d** for both ray tracing simulation and experimental results. Surprisingly, the experiments and the ray tracing results for diffuse scattering show that *G* is essentially independent of the aspect ratio and backscattering fraction. We attribute this new observation to the effects of multiple backscattering. After multiple diffuse scatterings inside the bridging necks, the phonon has no preferential direction when exiting the bridging necks, exactly as if the phonon had scattered off a physical diffuse surface of the long-pitch nanomesh (see inset of Figure 4-10**d**). For $P = 0.8$, the high-*AR* nanomesh has less diffuse scattering to randomize the phonon directions, and adding the bridging necks does cause a reduction in G as well as a reduction in k.

4.4.1 Discussion of phonon backscattering

This work and several others in the literature have compared thermal transport in nanomeshes to equivalent nanowires. Several works[99], [110] have concluded that the apparent nanomesh conductivity kf is smaller than k_{nw} of a nanowire with a similar rectangular cross section $n \times t$. However, such comparisons do not account for the bulk effect of the mesh porosity factor f. Other measurements[11], [122] have indicated that even after accounting for f, the nanomesh conductivity k remains smaller than the nanowire conductivity k_{nw}. Within the coherent phonon picture, this reduction has been attributed to a smaller group velocity arising from the modified phonon dispersion. On the other hand, within the BTE particle model, the reduction in k has been attributed to greater phonon backscattering off the mesh holes facing the direction of transport[110]. Our results rule out significant coherence effects, while concluding that the phonon backscattering mechanism reduces k (20% reduction for *AR* =1 vs. *AR*= 10 at 300 K).

4.5 Summary and future work

In summary, I developed ray tracing simulations to model incoherent phonon transport in silicon nanomeshes. I validated the simulations against analytical solutions and previous nanomesh simulations, and compared the simulations to experiments. The good agreement between ray tracing results and experiments indicate that the wave nature of phonons is not important in the regime where the phonon wavelengths are much smaller than the silicon nanomesh pitch and inelastic mean free path, but are comparable to the surface roughness. Rather, the particle backscattering effect quantified by the ray tracing simulations explains the experimental trends. The insights obtained from this work will be valuable in understanding phonon transport in complicated nanostructured geometries and exploring possibilities of future phononic applications.

Improvements to the ray tracing simulations could lead to further insight and comparison with experiment. Extending the simulation methodology to handle yet more complicated geometries such as porous nanowires[140] or three-dimensional silicon

nanostructures[141] would enable quantitative comparison with experiment to investigate whether the classical boundary scattering effects still dominate in even smaller nanostructures. Recent work has indicated that anisotropy can be included in the ray tracing formalism, but at a large computational cost [142]. The Monte Carlo ray tracing code is highly parallelizable, indicating that complicated anisotropic structures could be accurately simulated at reasonable speed using parallel computing. Lastly, the ray tracing is an incoherent simulation, considering only particle effects. Extending the ray tracing theory and implementation to include partial coherence would allow the simulations to capture the crossover from incoherent to coherent phonon transport in superlattices[98], which can have $\lambda \sim p$.

Chapter 5 : Analytical modeling of heat transfer in arbitrarily anisotropic thin films

Content adapted from a recently submitted manuscript: Geoff Wehmeyer, Andrea D. Pickel, and Chris Dames. "An Onsager reciprocity relation for ballistic phonon heat transport in anisotropic thin films of arbitrary orientation." I additionally would like to thank Chenhan Liu for providing the molecular dynamic simulation results.

Nanostructures with anisotropic thermal properties are another class of complicated nanostructures with thermal properties that are not fully understood. For example, in the bulk regime, a classic Onsager reciprocity relation states that the thermal conductivity tensor is symmetric. However, it is not known whether an analogous Onsager relation can be identified in the thin-film boundary scattering regime, meaning that there may be as many as nine independent components of the tensor. Here, we solve the Boltzmann transport equation (BTE) for thin films with anisotropic phonon dispersion relations and scattering rates. We use these BTE solutions to show that the thermal conductivity tensor of thin films remains symmetric from the diffusive regime through the boundary scattering regime. We illustrate this reciprocity by calculating thermal conductivity suppression functions for a model anisotropic material. We then compare our BTE solution to previous atomistic simulations of arbitrarily aligned graphite thin films, and use published first-principles calculations to model anisotropic in-plane heat flow in aligned black phosphorus. This derivation shows how Onsager reciprocity for anisotropic heat conduction extends into the boundary scattering regime, and reduces the number of independent measurements required to fully characterize heat transport in anisotropic thin films.

5.1 Motivation for modeling anisotropic thin films

Fourier's law breaks down in dielectric thin films due to ballistic phonon transport effects, which become important when the film thickness t is comparable to or less than the phonon's intrinsic mean free path Λ. The breakdown of Fourier's law leads to a reduction in the thermal conductivity κ compared to the bulk value κ_{bulk}. Boltzmann transport equation (BTE) models have been developed [4], [5], [143]–[146] to quantify this thin film boundary scattering suppression in materials that have phonon dispersion relations and scattering rates of sufficiently high symmetry such that the heat flux $\mathbf{q}$ is parallel to the temperature gradient ∇T. However, for arbitrarily aligned materials with anisotropic dispersions and scattering rates, $\mathbf{q}$ is no longer necessarily parallel to ∇T, an effect described by off-diagonal terms in the $\boldsymbol{\kappa}$ tensor. These arbitrarily aligned conditions can be found in thin films with low-symmetry monoclinic or triclinic unit cells[147]–[154], as well in films which have higher symmetry unit cells (*e.g.* orthorhombic) but have temperature gradients imposed in a low-symmetry direction[155]–[159]. Particular examples of recent thermal interest include the phase-change material vanadium dioxide (VO_2) in the monoclinic phase[15], [160], the layered material black phosphorus (which displays anisotropic in-plane thermal properties)[16], and thermoelectric materials such as SnSe[14] or Bi_2Te_3 [161]. Being able to predict the boundary scattering effects on the thermal properties of these materials is important for interpretation of novel transport physics[15] and for applications in waste heat

scavenging[162]. In addition, other arbitrarily aligned materials have been investigated for applications in heat flux sensing and transverse thermoelectric cooling [159], [163].

In the diffusive regime where Fourier's law applies, an important Onsager reciprocity relation for arbitrarily aligned anisotropic materials [17], [164] mandates that the $\boldsymbol{\kappa}$ tensor is symmetric in the absence of a magnetic field. This prototypical relation dates back to Onsager's first work on reciprocity[17] and fundamentally arises from the microscopic time reversal symmetry of the macroscopically irreversible diffusion process. However, this diffusive Onsager relation has not been theoretically or experimentally extended into the thin film boundary scattering regime where Fourier's law breaks down due to ballistic phonon effects. In contrast, well-known examples of ballistic reciprocity can be found in the four-point probe conductance relations from the electrical domain [132], [165]. These electrical results, however, are not easily modified to model the ballistic phonon transport of the present work, because the electrical four-point probe relations are derived from the Landauer-Büttiker formalism, while thin film phonon boundary scattering is analyzed using the Boltzmann equation.

Here, we identify a generalized version of the Onsager reciprocity relation by using BTE solution to show that the $\boldsymbol{\kappa}$ tensor is symmetric from the diffusive regime through the boundary scattering regime for arbitrarily aligned anisotropic thin films. We present an example calculation of the thin film reciprocity relation for a model material with an anisotropic Debye dispersion relation, and compare our BTE solutions to molecular dynamics simulations [166] of arbitrarily aligned graphite thin films. As a further case study, we combine a tensor transformation result from our BTE solutions with previously published first-principles calculations[146] to model thermal transport in thin-film black phosphorus, a layered material with anisotropic in-plane thermal conductivities. Our BTE solutions extend Onsager's reciprocity relation for heat conduction into the boundary scattering regime, and the reciprocity relation reduces the number of independent measurements required to fully characterize heat transfer in anisotropic thin films.

5.2 Derivation of Boltzmann equation solution

5.2.1 Boltzmann transport equation

We begin by deriving BTE solutions for heat transport in arbitrarily aligned anisotropic thin films. Under the relaxation time approximation, the steady-state phonon BTE without internal energy generation is

$$\mathbf{v}_{\mathbf{k}} \cdot \nabla f_{\mathbf{k}} = -\frac{f_{\mathbf{k}} - f_{0,\mathbf{k}}}{\tau_{\mathbf{k}}}, \tag{1}$$

where ∇ is the gradient in real space, the subscript $\mathbf{k}$ denotes the phonon wavevector for a given polarization, $\mathbf{v}_{\mathbf{k}}$ and $\tau_{\mathbf{k}}$ are respectively the mode-dependent group velocity and bulk relaxation time, $f_{\mathbf{k}}$ is the distribution function (initially unknown), and the

equilibrium Bose-Einstein distribution function $f_{0,\mathbf{k}} = \left(\exp\left(\frac{\mathrm{h}\omega_{\mathbf{k}}}{k_B T} \right) - 1 \right)^{-1}$. Note that for simplicity of presentation, we suppress the index labeling the phonon polarization for all mode-dependent quantities, but this is understood to be contained within the symbol $\mathbf{k}$. The phonon angular frequency is $\omega_{\mathbf{k}}$, h is the reduced Planck constant, k_B is the Boltzmann constant, and T is the unknown local temperature.

The local heat flux vector is

$$\mathbf{q} = \frac{1}{V} \sum_{\mathbf{k}} \mathrm{h}\omega_{\mathbf{k}} \mathbf{v}_{\mathbf{k}} f_{\mathbf{k}}, \tag{2}$$

where V is the volume of the sample. In Eq. (2) and throughout this paper, a summation over $\mathbf{k}$ also implies a sum over polarizations. Conservation of energy dictates that at steady state with no heat generation, $\nabla \cdot \mathbf{q} = 0$. Taking the gradient of Eq. (2), noting that $\nabla \cdot \mathbf{v}_{\mathbf{k}} = 0$ for a homogeneous material, and substituting for $\mathbf{v}_{\mathbf{k}} \cdot \nabla f_{\mathbf{k}}$ using the BTE (Eq. (1)), the conservation of energy requirement becomes

$$\sum_{\mathbf{k}} \frac{\mathrm{h}\omega_{\mathbf{k}}}{\tau_{\mathbf{k}}} (f_{\mathbf{k}} - f_{0,\mathbf{k}}) = 0. \tag{3}$$

We will obtain BTE solutions for the two different scenarios of imposed temperature differences in the cross-plane direction and an in-plane direction. In both cases, we will use the recently developed deviational form of the Boltzmann equation[144], [167]. In the deviational BTE, we consider small temperature differences, such that at any spatial location the difference between the actual temperature T and the reference Fourier temperature profile T_r is much smaller than the magnitude of T. The deviational BTE solution represents the linear response of the BTE, and is equivalent to neglecting the temperature dependence of microscopic quantities such as the modewise specific heats.

5.2.2 Cross-plane temperature difference

We first consider a cross-plane temperature difference imposed across a thin film of thickness t, shown in Figure 5-1(a). The bottom black surface $(y = 0)$ is at a hot temperature T_h, and the top black surface $(y = t)$ is at a cold temperature T_c, and thus the cross-plane Fourier temperature profile is $T_{r,y} = T_h - (T_h - T_c)(y/t)$. We apply periodic boundary conditions in the $\hat{x}$ and $\hat{z}$ directions, so the only gradients in $f_{\mathbf{k}}$ and T are in the $\hat{y}$ direction; however, for crystals of sufficiently low symmetry, the temperature difference in $\hat{y}$ induces heat flows in orthogonal directions $(\hat{x}, \hat{z})$.

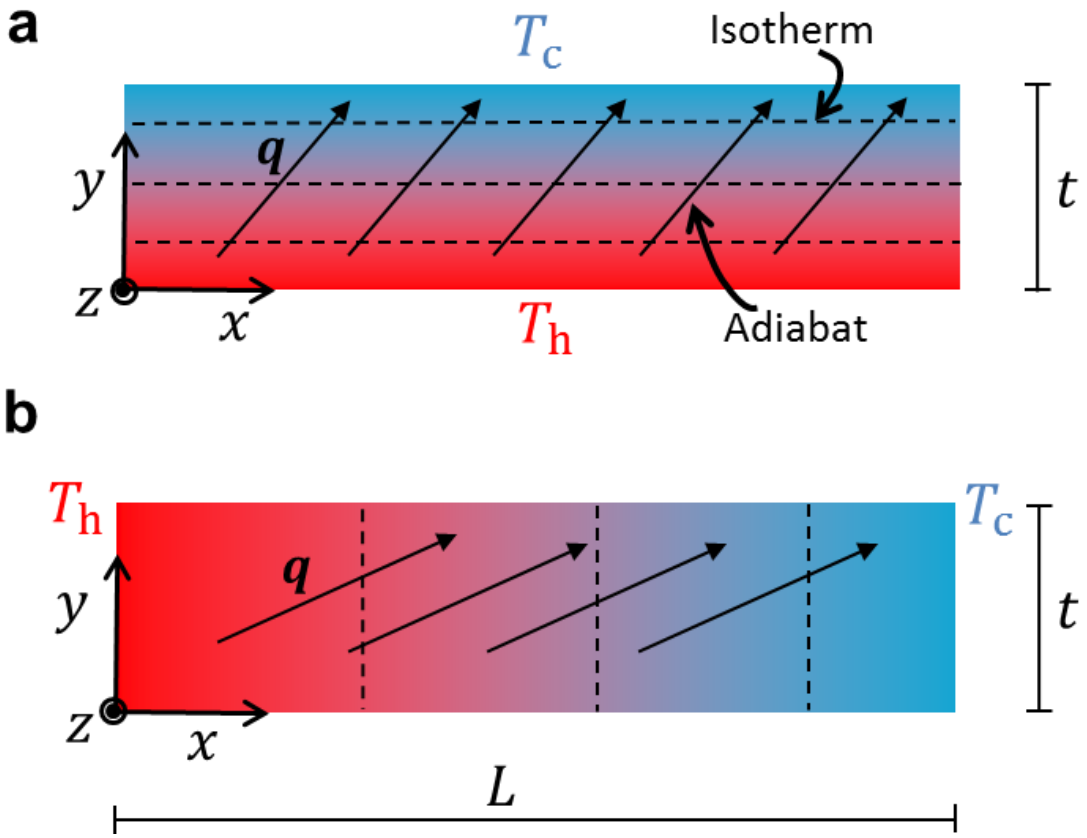

Figure 5-1: Schematic of anisotropic heat transfer in thin films due to (a) cross-plane and (b) in-plane temperature differences $(T_h - T_c)$. In arbitrarily aligned anisotropic materials, the heat flux $\mathbf{q}$ is not necessarily parallel to the temperature gradient ∇T, as represented by non-orthogonal adiabats and isotherms in (a,b) and mathematically described by off-diagonal components of the thermal conductivity tensor $\boldsymbol{\kappa}$. We use Boltzmann transport equation solutions to prove that $\boldsymbol{\kappa}$ remains symmetric from the bulk through the thin film boundary scattering regime.

We solve for the cross-plane deviational energy distribution function $g_{\mathbf{k}} \equiv \hbar\omega_{\mathbf{k}}(f_{\mathbf{k}} - f_{\mathbf{k},0}(T_{r,y}))/C_{\mathbf{k}}(T_h - T_c)$, where $C_{\mathbf{k}} \equiv \hbar\omega_{\mathbf{k}} \dfrac{\partial f_{\mathbf{k},0}}{\partial T}$ is the modewise specific heat. We also introduce the dimensionless parameters $\eta \equiv y/t$ and $\lambda_{\mathbf{k},y} \equiv \Lambda_{\mathbf{k},y}/t$. Here, the second subscript y indicates the vector mean free path has been projected along $\hat{y}$, that is, $\Lambda_{\mathbf{k},y} \equiv (\mathbf{v}_{\mathbf{k}} \cdot \hat{y})\tau_{\mathbf{k}}$. Due to this projection, $\Lambda_{\mathbf{k},y}$ is positive (negative) for phonons travelling with group velocities along + $\hat{y}$ ($-\hat{y}$). Expressing Eq. (1) in terms of g_k, and noting that $\hbar\omega_{\mathbf{k}}\left[f_{\mathbf{k},0}(T) - f_{\mathbf{k},0}(T_{r,y})\right] = C_{\mathbf{k}}(T - T_{r,y})$ for small temperature differences, the BTE becomes

$$\lambda_{\mathbf{k},y}\frac{dg_{\mathbf{k}}}{d\eta} + g_{\mathbf{k}} = \lambda_{\mathbf{k},y} + \Delta T_y(\eta), \tag{4}$$

where $\Delta T_y(\eta) \equiv \left(T(\eta) - T_{r,y}(\eta)\right)/\left(T_h - T_c\right)$ is the (currently undetermined) dimensionless deviational cross-plane temperature profile due to the imposed temperature difference in y. Using an integrating factor, we obtain the integral forms of Eq. (4) as

$$g_{\mathbf{k}}^{+}(\eta) = g_{\mathbf{k},0}^{+} \exp\left(-\frac{\eta}{\lambda_{\mathbf{k},y}}\right) + \int_{\eta'=0}^{\eta} \left[\lambda_{\mathbf{k},y} + \Delta T_y(\eta')\right] \exp\left(-\frac{\eta-\eta'}{\lambda_{\mathbf{k},y}}\right) \frac{d\eta'}{\lambda_{\mathbf{k},y}} \tag{5}$$

$$g_{\boldsymbol{k}}^{-}(\eta) = g_{\mathbf{k},1}^{-} \exp\left(\frac{1-\eta}{\lambda_{\mathbf{k},y}}\right) - \int_{\eta'=\eta}^{1} \left[\lambda_{\mathbf{k},y} + \Delta T_y(\eta')\right] \exp\left(-\frac{\eta-\eta'}{\lambda_{\mathbf{k},y}}\right) \frac{d\eta'}{\lambda_{\boldsymbol{k},y}}. \tag{6}$$

Here $g_{\mathbf{k}}^{+}(\eta)$ is the distribution function for phonons travelling upward ($\lambda_{\mathbf{k},y} > 0$), and $g_{\mathbf{k}}^{-}(\eta)$ is the distribution function for phonons travelling downward ($\lambda_{\mathbf{k},y} < 0$). Using the boundary condition $f_{\mathbf{k}} = f_{\mathbf{k},0}\left(T_{r,y}\right)$ for all phonons emitted from a wall, the integration constants are simply $g_{\mathbf{k},0}^{+} = g_{\mathbf{k},1}^{-} = 0$.

Now we implement the energy conservation requirement. Substituting the definition of $g_{\mathbf{k}}$ into Eq. (3), we have

$$\Delta T_y(\eta) = \left(\sum_{\mathbf{k}} \frac{C_{\mathbf{k}}}{\tau_{\mathbf{k}}}\right)^{-1} \left(\sum_{\mathbf{k}} \frac{C_{\mathbf{k}}}{\tau_{\mathbf{k}}} g_{\mathbf{k}}\right). \tag{7}$$

Substituting the integral forms of the BTE (Eqs. (5) and (6)) into Eq. (7) yields an integral expression for the unknown ΔT_y. This expression can be further simplified using the required inversion symmetries[168] of the phonon dispersion relation: time reversal symmetry mandates that $C_{\mathbf{k}}$ is even and $\boldsymbol{v}_{\mathbf{k}}$ is odd upon inversion of $\mathbf{k}$, even if the point group of the crystal's unit cell is non-centrosymmetric**.** We also restrict our attention to the most common phonon scattering processes (such as phonon-phonon or phonon-impurity scattering) that do not involve magnetic fields and thus obey time-reversal symmetry[17]. Therefore, $\tau_{\mathbf{k}}$ is also even under inversion of $\mathbf{k}$. Using these inversion symmetries, we obtain an integral equation for the deviational temperature profile

$$\Delta T_y(\eta) = \left(\sum_{\mathbf{k}} \frac{C_{\mathbf{k}}}{\tau_{\mathbf{k}}}\right)^{-1} \sum_{\lambda_{\mathbf{k},y}>0} \frac{C_{\mathbf{k}}}{\tau_{\mathbf{k}}} \lambda_{\mathbf{k},y} \left[\exp\left(-\frac{1-\eta}{\lambda_{\mathbf{k},y}}\right) - \exp\left(-\frac{\eta}{\lambda_{\mathbf{k},y}}\right) + \int_{\eta'=0}^{1} \Delta T_y(\eta') \exp\left(-\frac{|\eta-\eta'|}{\lambda_{\mathbf{k},y}}\right) \frac{d\eta'}{\lambda_{\mathbf{k},y}^2}\right]. \tag{8}$$

The notation in Eq. (8) indicates a summation over all modes that have $\lambda_{\mathbf{k},y} > 0$. To summarize this intermediate result, we have derived the temperature profile in response to a cross-plane temperature difference $\left(T_h - T_c\right)$ applied at the boundaries. We will later use Eq. (8) to derive the reciprocity relation.

5.2.3 In-plane temperature difference

We now move on to consider the conjugate problem of in-plane temperature differences along an arbitrarily selected in-plane direction $\hat{x}$ for a thin film of thickness t and a large length L, as shown in Figure 5-1(b). The traditional BTE approach for in-plane transport [4], [5], [144] never explicitly enforces energy conservation to find the temperature profile, but rather assumes that the temperature profile is always the in-plane Fourier reference temperature profile $T_{r,x}(x) = T_h - (T_h - T_c)(x/L)$. However, we will show that the temperature profile in arbitrarily aligned thin films can deviate from $T_{r,x}$ due to ballistic effects, indicating that the energy conservation requirement $\nabla \cdot \mathbf{q} = 0$ must be deployed to solve for the actual temperature profile.

The in-plane solution is very similar to the cross-plane procedure detailed above. We solve for the in-plane energy distribution function $j_{\mathbf{k}} \equiv \hbar\omega_{\mathbf{k}} \left(f_{\mathbf{k}} - f_{\mathbf{k},0}(T_{r,x}) \right) / C_{\mathbf{k}} (T_h - T_c)$, where $j_{\mathbf{k}}$ is analogous to $g_{\mathbf{k}}$ from the cross-plane scenario. Introducing the dimensionless x location $\zeta \equiv x/L$ and substituting into Eq. (1), the BTE becomes

$$\lambda_{\mathbf{k},x} \frac{dj_{\mathbf{k}}}{d\zeta} + \lambda_{\mathbf{k},y} \frac{dj_{\mathbf{k}}}{d\eta} + j_{\mathbf{k}} = \lambda_{\mathbf{k},x} + \Delta T_x, \tag{9}$$

where $\lambda_{\mathbf{k},x} \equiv \Lambda_{\mathbf{k},x} / L$ and $\Delta T_x(\eta) \equiv (T - T_{r,x}) / (T_h - T_c)$. Since $\lambda_{\mathbf{k},x} << \lambda_{\mathbf{k},y}$, we drop the derivative involving ζ, and Eq. (9) becomes a first order ODE for $j_{\mathbf{k}}(\eta)$.

The boundary conditions for in-plane transport should be conjugate to the cross-plane scenario boundary conditions. In the cross-plane solution, heat is allowed to flow along $\hat{x}$ due to the temperature difference along $\hat{y}$. Similarly, for the in-plane solution, the boundary conditions must allow heat to flow along $\hat{y}$ due to a temperature difference along $\hat{x}$. Therefore, we treat the bottom and top surfaces ($y = 0$ and $y = t$) as black emitters maintained at $T_{r,x}(x)$. This choice of boundary conditions allows heat to leave the film through the top and bottom surfaces, thereby providing the correct conjugate behavior to the cross-plane scenario.

Proceeding analogously to the cross-plane case, we obtain the formal solution to the BTE (Eq. (9)) as

$$j_{\mathbf{k}}^{+}(\eta) = j_{\mathbf{k},0}^{+} \exp\left(-\frac{\eta}{\lambda_{\mathbf{k},y}} \right) + \int_{\eta'=0}^{\eta} \left[\lambda_{\mathbf{k},x} + \Delta T_x(\eta') \right] \exp\left(-\frac{\eta - \eta'}{\lambda_{\mathbf{k},y}} \right) \frac{d\eta'}{\lambda_{\mathbf{k},y}} \tag{10}$$

$$j_{\mathbf{k}}^{-}(\eta) = j_{\mathbf{k},1}^{-} \exp\left(\frac{1-\eta}{\lambda_{\mathbf{k},y}} \right) - \int_{\eta'=\eta}^{1} \left[\lambda_{\mathbf{k},x} + \Delta T_x(\eta') \right] \exp\left(-\frac{\eta - \eta'}{\lambda_{\mathbf{k},y}} \right) \frac{d\eta'}{\lambda_{\mathbf{k},y}}. \tag{11}$$

Here $j_{\mathbf{k}}^{+}(\eta)$ is the distribution function for phonons travelling upward ($\lambda_{\mathbf{k},y}>0$), and $j_{\mathbf{k}}^{-}(\eta)$ is the distribution function for phonons travelling downward ($\lambda_{\mathbf{k},y}<0$). We fix the integration constants $j_{\mathbf{k},0}^{+}$ and $j_{\mathbf{k},1}^{-}$ using the boundary conditions at the walls. Since the walls are treated as black emitters, $f_{\mathbf{k}}=f_{\mathbf{k},0}\left(T_{r,x}\right)$ for all phonons leaving the walls. Applying this boundary condition to Eqs. (10) and (11) yields $j_{\mathbf{k},0}^{+}=j_{\mathbf{k},1}^{-}=0$.

Now we implement the energy conservation requirement, which is

$$\Delta T_x(\eta)=\left(\sum_{\mathbf{k}}\frac{C_{\mathbf{k}}}{\tau_{\mathbf{k}}}\right)^{-1}\left(\sum_{\mathbf{k}}\frac{C_{\mathbf{k}}}{\tau_{\mathbf{k}}}j_{\mathbf{k}}\right). \tag{12}$$

Plugging Eqs.(10) and (11) into Eq. (12), we obtain

$$\Delta T_x(\eta)=\left(\sum_{\mathbf{k}}\frac{C_{\mathbf{k}}}{\tau_{\mathbf{k}}}\right)^{-1}\left\{\begin{array}{l}\left[\sum_{\lambda_{\mathbf{k},y}>0}\frac{C_{\mathbf{k}}}{\tau_{\mathbf{k}}}\int_{\eta'=0}^{\eta}\left[\lambda_{\mathbf{k},x}+\Delta T_x(\eta')\right]\exp\left(-\frac{\eta-\eta'}{\lambda_{\mathbf{k},y}}\right)\frac{d\eta'}{\lambda_{\mathbf{k},y}}\right]\\ -\left[\sum_{\lambda_{\mathbf{k},y}<0}\frac{C_{\mathbf{k}}}{\tau_{\mathbf{k}}}\int_{\eta'=\eta}^{1}\left[\lambda_{\mathbf{k},x}+\Delta T_x(\eta')\right]\exp\left(-\frac{\eta-\eta'}{\lambda_{\mathbf{k},y}}\right)\frac{d\eta'}{\lambda_{\mathbf{k},y}}\right]\end{array}\right\}. \tag{13}$$

Using the inversion symmetries of the dispersion and scattering, we change the summation over $\lambda_{\mathbf{k},y}<0$ in Eq. (13) to an equivalent summation over $\lambda_{\mathbf{k},y}>0$ as

$$\Delta T_x(\eta)=\left(\sum_{\mathbf{k}}\frac{C_{\mathbf{k}}}{\tau_{\mathbf{k}}}\right)^{-1}\left\{\begin{array}{l}\left[\sum_{\lambda_{\mathbf{k},y}>0}\frac{C_{\mathbf{k}}}{\tau_{\mathbf{k}}}\int_{\eta'=0}^{\eta}\left[\lambda_{\mathbf{k},x}+\Delta T_x(\eta')\right]\exp\left(-\frac{\eta-\eta'}{\lambda_{\mathbf{k},y}}\right)\frac{d\eta'}{\lambda_{\mathbf{k},y}}\right]\\ +\left[\sum_{\lambda_{\mathbf{k},y}>0}\frac{C_{\mathbf{k}}}{\tau_{\mathbf{k}}}\int_{\eta'=\eta}^{1}\left[-\lambda_{\mathbf{k},x}+\Delta T_x(\eta')\right]\exp\left(\frac{\eta-\eta'}{\lambda_{\mathbf{k},y}}\right)\frac{d\eta'}{\lambda_{\mathbf{k},y}}\right]\end{array}\right\}. \tag{14}$$

Combining the summations in Eq. (14) and rearranging,

$$\Delta T_x(\eta)=\left(\sum_{\mathbf{k}}\frac{C_{\mathbf{k}}}{\tau_{\mathbf{k}}}\right)^{-1}\sum_{\lambda_{\mathbf{k},y}>0}\frac{C_{\mathbf{k}}}{\tau_{\mathbf{k}}}\lambda_{\mathbf{k},x}\left(\begin{array}{l}\int_{\eta'=0}^{\eta}\exp\left(-\frac{\eta-\eta'}{\lambda_{\mathbf{k},y}}\right)\frac{d\eta'}{\lambda_{\mathbf{k},y}}-\int_{\eta'=\eta}^{1}\exp\left(\frac{\eta-\eta'}{\lambda_{\mathbf{k},y}}\right)\frac{d\eta'}{\lambda_{\mathbf{k},y}}\\ +\int_{\eta'=0}^{1}\Delta T_x(\eta')\exp\left(\frac{|\eta-\eta'|}{\lambda_{\mathbf{k},y}}\right)\frac{d\eta'}{\lambda_{\mathbf{k},y}\lambda_{\mathbf{k},x}}\end{array}\right). \tag{15}$$

After performing the first two integrals in Eq. (15) analytically, we obtain an integral equation for the in-plane deviational temperature profile

$$\Delta T_x(\eta)=\left(\sum_{\mathbf{k}}\frac{C_{\mathbf{k}}}{\tau_{\mathbf{k}}}\right)^{-1}\sum_{\lambda_{\mathbf{k},y}>0}\frac{C_{\mathbf{k}}}{\tau_{\mathbf{k}}}\lambda_{\mathbf{k},x}\left[\exp\left(-\frac{1-\eta}{\lambda_{\mathbf{k},y}}\right)-\exp\left(-\frac{\eta}{\lambda_{\mathbf{k},y}}\right)+\int_{\eta'=0}^{1}\Delta T_x(\eta')\exp\left(-\frac{|\eta-\eta'|}{\lambda_{\mathbf{k},y}}\right)\frac{d\eta'}{\lambda_{\mathbf{k},y}\lambda_{\mathbf{k},x}}\right]. \quad (16)$$

If the material has a mirror symmetry on reflection across the yz plane (i.e. $\lambda_{\mathbf{k},x}$ is odd and $\lambda_{\mathbf{k},y}$ is even upon taking k_x to $-k_x$), the summation over the first two terms in the square bracket of Eq. (16) is zero. In that case, the trivial solution $\Delta T_x(\eta)=0$ results and no temperature gradients develop in the cross-plane direction y. This is the scenario for isotropic or aligned anisotropic thin films. However, a cross-plane temperature gradient can develop when the mirror symmetry is broken in the arbitrarily aligned scenario. Lastly, because the in-plane direction $\hat{x}$ was arbitrarily designated, the results of this section are trivially modified for temperature differences applied in the orthogonal in-plane direction $\hat{z}$ by relabeling the subscripts from x to z in Eq. (16).

5.2.4 Onsager reciprocity relation for thin film boundary scattering

We now use our BTE solutions to derive the central result of the paper, which is the generalized Onsager reciprocity relation for thin films with anisotropic dispersion relations or scattering. We will show that that the $\boldsymbol{\kappa}$ tensor is symmetric from the diffusive regime through the boundary scattering regime. We note that even though Fourier's law itself breaks down in the ballistic regime, it is useful to generalize the thermal conductivity concept into the boundary scattering regime by defining the elements of the $\boldsymbol{\kappa}$ tensor using the total heat flows, temperature differences, and sample dimensions. For example, the in-plane thermal conductivity κ_{xx} of thin films is conventionally defined[144] as $\kappa_{xx}\equiv -Q'_x/(t\frac{dT}{dx})$, where $Q'_x\equiv t\int_0^1 q_x d\eta$ is the in-plane heat flow divided by the sample width in the $\hat{z}$ direction w. In the diffusive regime where Fourier's law holds, $\kappa_{xx}=\kappa_{xx,bulk}$. However, κ_{xx} is suppressed below $\kappa_{xx,bulk}$ in the boundary scattering regime where Fourier's law breaks down due to ballistic effects.

To prove that the $\boldsymbol{\kappa}$ tensor is symmetric, we need to determine the six off-diagonal components of the tensor. We begin by calculating κ_{xy}, defined as the ratio of Q'_x to the cross-plane temperature difference (T_h-T_c). Substituting the definition of $g_{\mathbf{k}}$ into the definition of the heat flux (Eq. (2)) and dividing by (T_h-T_c),

$$\kappa_{xy}=\frac{1}{V}\sum_{\mathbf{k}}C_{\mathbf{k}}v_{\mathbf{k},x}t\int_0^1 g_{\mathbf{k}}d\eta. \quad (17)$$

We find $\int_0^1 g_{\mathbf{k}}d\eta$ by integrating the BTE (Eq. (4)) from $\eta=0$ to 1 and re-arranging to obtain

$$\int_0^1 g_{\mathbf{k}} d\eta = -\lambda_{\mathbf{k},y}\left[g_{\mathbf{k}}(1) - g_{\mathbf{k}}(0) - 1\right] + \int_0^1 \Delta T_y(\eta) d\eta. \tag{18}$$

Here $g_{\mathbf{k}}(0)$ and $g_{\mathbf{k}}(1)$ are determined from the integral form of the BTE (Eqs. (5) and (6)) after applying the boundary conditions. Substituting into Eq. (17) after again using the inversion symmetry of the dispersion and scattering, we obtain an important final result for the off-diagonal conductivity

$$\begin{aligned}\kappa_{xy} = \kappa_{xy,bulk} &- \frac{2}{V}\sum_{\lambda_{\mathbf{k},y}>0} \kappa_{\mathbf{k},xy}\lambda_{\mathbf{k},y}\left[1-\exp\left(-\frac{1}{\lambda_{\mathbf{k},y}}\right)\right] \\ &- \frac{1}{V}\sum_{\lambda_{\mathbf{k},y}>0} \kappa_{\mathbf{k},xy}\int_{\eta=0}^{1}\Delta T_y(\eta)\left[\exp\left(-\frac{1-\eta}{\lambda_{\mathbf{k},y}}\right)-\exp\left(-\frac{\eta}{\lambda_{\mathbf{k},y}}\right)\right]\frac{d\eta}{\lambda_{\mathbf{k},y}}.\end{aligned} \tag{19}$$

Here, we have introduced the modewise contribution to the off-diagonal thermal conductivity $\kappa_{\mathbf{k},xy} \equiv C_{\mathbf{k}} v_{\mathbf{k},x} v_{\mathbf{k},y} \tau_{\mathbf{k}}$, such that the bulk off-diagonal thermal conductivity $\kappa_{xy,bulk} = \frac{1}{V}\sum_{\mathbf{k}} \kappa_{\mathbf{k},xy}$. In the diffusive regime where $\lambda_{\mathbf{k},y} << 1$ for all phonons, the first term on the right hand side (RHS) of Eq. (19) dominates and we recover the Fourier result $\kappa_{xy} = \kappa_{xy,bulk}$. In the ballistic regime where $\lambda_{\mathbf{k},y} >> 1$, the first two terms on the RHS combine to yield the ballistic conductivity $\kappa_{xy} = \frac{1}{V}\sum_{\lambda_{\mathbf{k},y}>0} C_{\mathbf{k}} v_{\mathbf{k},x} t$.

Interestingly, in both the diffusive and ballistic regimes, the last term in Eq. (19) including the deviational temperature profile is unimportant and we do not need to solve the integral equation for ΔT_y (Eq. (8)). This can be seen by noting that in the diffusive regime, ΔT_y is of order $\lambda_y (<<1)$ and the third term in Eq. (13) is smaller than the first term by a factor of λ_y. In the ballistic regime, ΔT_y is of order 1/2, and the third term is smaller than the ballistic conductivity by a factor of $1/\lambda_y$. In the intermediate regime where $\lambda_{\mathbf{k},y} \sim 1$, all three terms contribute to κ_{xy}.

Now, we likewise calculate $\kappa_{yx} \equiv Q_y^{'}/(T_h - T_c)$, where $Q_y^{'} \equiv L\int_0^1 q_y d\zeta$ is the cross-plane heat flow divided by w and $(T_h - T_c)$ is the in-plane temperature difference. We will further manipulate $Q_y^{'}$ into a convenient form for the Onsager relation. First, we note that q_y is independent of position, which follows from the energy conservation requirement $\nabla \cdot \mathbf{q} = 0$ and the large L stipulation that $\frac{\partial q_x}{\partial x} = \frac{\partial q_y}{\partial x} = 0$. Thus, $Q_y^{'}$ can

equivalently be written as $Q_y^{'} = L\int_0^1 q_y d\eta$, since $\int_0^1 q_y d\eta = \int_0^1 q_y d\zeta = q_y$. We choose to represent $Q_y^{'}$ in this peculiar manner to facilitate later comparisons with $Q_x^{'}$ from the cross-plane scenario, where the integral over the dimensionless y location η arises naturally. Therefore, the off-diagonal conductivity $\kappa_{yx} = \frac{1}{V}\sum_{\mathbf{k}} C_{\mathbf{k}} v_{\mathbf{k},y} L\int_0^1 j_{\mathbf{k}} d\eta.$

Proceeding similarly to the development of Eq. (19), we integrate the in-plane BTE (Eq. (9)) from $\eta = 0$ to 1 to obtain an expression for $\int_0^1 j_{\mathbf{k}} d\eta$, and then determine $j_{\mathbf{k}}(0)$ and $j_{\mathbf{k}}(1)$ using the integral form of the BTE. Multiplying by $C_{\mathbf{k}} v_{\mathbf{k},y}$, summing over all modes, and using inversion symmetry, we obtain

$$\begin{aligned}\kappa_{yx} &= \kappa_{xy,bulk} - \frac{2}{V}\sum_{\lambda_{\mathbf{k},y}>0} \kappa_{\mathbf{k},xy}\lambda_{\mathbf{k},y}\left[1-\exp\left(-\frac{1}{\lambda_{\mathbf{k},y}}\right)\right] \\ &\quad -\frac{1}{V}\sum_{\lambda_{\mathbf{k},y}>0} \kappa_{\mathbf{k},xy}\int_{\eta=0}^{1}\Delta T_x(\eta)\left[\exp\left(-\frac{1-\eta}{\lambda_{\mathbf{k},y}}\right)-\exp\left(-\frac{\eta}{\lambda_{\mathbf{k},y}}\right)\right]\frac{d\eta}{\lambda_{\mathbf{k},x}}.\end{aligned} \tag{20}$$

We have also leveraged the fact that by definition, $\kappa_{xy,bulk} = \kappa_{yx,bulk}$ and $\kappa_{\mathbf{k},xy} = \kappa_{\mathbf{k},yx}$. Since the first two terms on the RHS of Eq. (20) for κ_{yx} are exactly the same as the first two terms on the RHS of Eq. (19) for κ_{xy}, subtracting and rearranging yields

$$\begin{aligned}\kappa_{xy} - \kappa_{yx} &= -\frac{tL}{V}\int_{\eta=0}^{1}\Delta T_y(\eta)\left\{\sum_{\lambda_{\mathbf{k},y}>0}\frac{C_{\mathbf{k}}\lambda_{\mathbf{k},x}}{\tau_{\mathbf{k}}}\left[\exp\left(-\frac{1-\eta}{\lambda_{\mathbf{k},y}}\right)-\exp\left(-\frac{\eta}{\lambda_{\mathbf{k},y}}\right)\right]\right\}d\eta \\ &\quad +\frac{tL}{V}\int_{\eta=0}^{1}\Delta T_x(\eta)\left\{\sum_{\lambda_{\mathbf{k},y}>0}\frac{C_{\mathbf{k}}\lambda_{\mathbf{k},y}}{\tau_{\mathbf{k}}}\left[\exp\left(-\frac{1-\eta}{\lambda_{\mathbf{k},y}}\right)-\exp\left(-\frac{\eta}{\lambda_{\mathbf{k},y}}\right)\right]\right\}d\eta.\end{aligned} \tag{21}$$

The terms in braces that multiply each of the deviational temperature profiles in Eq. (21) have already appeared in the integral solutions of the BTE (Eqs. (8) and (16)). Substituting those expressions into Eq. (21) and simplifying, we see that

$$\kappa_{xy} - \kappa_{yx} = \frac{tL}{V}\sum_{\lambda_{\mathbf{k},y}>0}\frac{C_{\mathbf{k}}}{\tau_{\mathbf{k}}\lambda_{\mathbf{k},y}}\left[\int_{\eta=0}^{1}\int_{\eta'=0}^{1}\exp\left(-\frac{|\eta-\eta'|}{\lambda_{\mathbf{k},y}}\right)\left[\Delta T_y(\eta)\Delta T_x(\eta') - \Delta T_y(\eta')\Delta T_x(\eta)\right]d\eta d\eta'\right]. \tag{22}$$

The integrand of Eq. (22) is anti-symmetric upon the exchange of variables $(\eta,\eta') \leftrightarrow (\eta',\eta)$. Since the limits of integration are from 0 to 1 for both η and η', we see that every contribution to the integral from (η,η') is exactly nulled by the

corresponding contribution from (η', η) of equal magnitude but opposite sign. Therefore, regardless of the functional forms of $\Delta T_y(\eta)$ and $\Delta T_x(\eta)$, Eq. (22) must always integrate to 0, and so

$$\kappa_{xy} = \kappa_{yx}. \tag{23}$$

Thus, we have found a principal result of this chapter: a derivation of a thermal conductivity reciprocity relation from the BTE.

We now extend this $(x \leftrightarrow y)$ reciprocity relation to the other two pairs of off-diagonal terms in the $\boldsymbol{\kappa}$ tensor. First, we note that since our distinction between the two orthogonal in-plane directions $(\hat{x}, \hat{z})$ was entirely arbitrary, the previous proof leading to Eq. (23) also shows that $\kappa_{zy} = \kappa_{yz}$. The last pair of off-diagonal thermal conductivities to compute from the BTE are the in-plane off-diagonal components κ_{zx} and κ_{xz}. We will now follow a procedure analogous to the development of Eqs. (17)-(23) to show that $\kappa_{zx} = \kappa_{xz}$.

5.2.5 Proof of the in-plane reciprocity relation

We begin by using our in-plane BTE solution to find $\kappa_{zx} \equiv Q_z^{'} / (T_h - T_c)$, where $Q_z^{'}$ is the heat flow in the $\hat{z}$ direction divided by t. Our solution proceeds analogously to the derivation of the reciprocity relation in the main text (Eq. (23). Substituting our definition of $j_{\mathbf{k}}$ into Eq. (2), integrating over the film thickness, and dividing by $(T_h - T_c)$, we obtain

$$\kappa_{zx} = \frac{L}{V} \sum_{\mathbf{k}} C_{\mathbf{k}} v_{\mathbf{k},z} \int_0^1 j_{\mathbf{k}} d\eta. \tag{24}$$

We integrate the in-plane BTE (Eq. (9)) from $\eta = 0$ to 1 to obtain an expression for $\int_0^1 j_{\mathbf{k}} d\eta$, and then determine $j_{\mathbf{k}}(0)$ and $j_{\mathbf{k}}(1)$ using the integral form of the BTE. Substituting into Eq. (24), we obtain

$$\kappa_{zx} = \frac{L}{V} \sum_{\lambda_{\mathbf{k},y}>0} C_{\mathbf{k}} v_{\mathbf{k},z} \left\{ \left(\lambda_{\mathbf{k},x} - \lambda_{\mathbf{k},x}\lambda_{\mathbf{k},y} \left(1 - \exp\left(-\frac{1}{\lambda_{\mathbf{k},y}} \right) \right) \right) - \int_{\eta'=0}^{1} \Delta T_x(\eta') \exp\left(-\frac{1-\eta'}{\lambda_{\mathbf{k},y}} \right) d\eta' + \int_0^1 \Delta T_x d\eta \right\} \tag{25}$$
$$+ \frac{L}{V} \sum_{\lambda_{\mathbf{k},y}<0} C_{\mathbf{k}} v_{\mathbf{k},z} \left\{ \left(\lambda_{\mathbf{k},x} - \lambda_{\mathbf{k},x}\lambda_{\mathbf{k},y} \left(\exp\left(\frac{1}{\lambda_{\mathbf{k},y}} \right) - 1 \right) \right) - \int_{\eta'=0}^{1} \Delta T_x(\eta') \exp\left(\frac{\eta'}{\lambda_{\mathbf{k},y}} \right) d\eta' + \int_0^1 \Delta T_x d\eta \right\}.$$

Using the symmetries of the dispersion relation to convert the summation over $\lambda_{\mathbf{k},y} < 0$ to an equivalent summation over $\lambda_{\mathbf{k},y} > 0$, we simplify Eq. (25)as

$$\kappa_{zx} = \kappa_{xz,bulk} - \frac{2}{V}\sum_{\lambda_{\mathbf{k},y}>0}\kappa_{\mathbf{k},xz}\lambda_{\mathbf{k},y}\left(1-\exp(-\frac{1}{\lambda_{\mathbf{k},y}})\right) - \frac{1}{V}\sum_{\lambda_{\mathbf{k},y}>0}\kappa_{\mathbf{k},xz}\int_{\eta'=0}^{1}\Delta T_x(\eta')\left(\exp\left(-\frac{1-\eta'}{\lambda_{\mathbf{k},y}}\right)-\exp\left(-\frac{\eta'}{\lambda_{\mathbf{k},y}}\right)\right)\frac{d\eta'}{\lambda_{\mathbf{k},x}}, \quad (26)$$

where $\kappa_{\mathbf{k},xz} \equiv C_{\mathbf{k}} v_{\mathbf{k},x} v_{\mathbf{k},z} \tau_{\mathbf{k}}$ and $\kappa_{xz,bulk} = \frac{1}{V}\sum_{\mathbf{k}}\kappa_{\mathbf{k},xz}$.

As previously noted in Section 5.2.3 , the designation of the in-plane direction $\hat{x}$ was arbitrary. Therefore, to assist in identifying the thermal conductivity component κ_{xz} we can write down the deviational temperature profile $\Delta T_z(\eta)$ due to an imposed temperature difference $(T_h - T_c)$ in $\hat{z}$ by direct analogy with Eq. (16) as

$$\Delta T_z(\eta) = \left(\sum_{\mathbf{k}}\frac{C_{\mathbf{k}}}{\tau_{\mathbf{k}}}\right)^{-1}\sum_{\lambda_{\mathbf{k},y}>0}\frac{C_{\mathbf{k}}}{\tau_{\mathbf{k}}}\lambda_{\mathbf{k},z}\left[\exp\left(-\frac{1-\eta}{\lambda_{\mathbf{k},y}}\right)-\exp\left(-\frac{\eta}{\lambda_{\mathbf{k},y}}\right)+\int_{\eta'=0}^{1}\Delta T_z(\eta')\exp\left(-\frac{|\eta-\eta'|}{\lambda_{\mathbf{k},y}}\right)\frac{d\eta'}{\lambda_{\mathbf{k},y}\lambda_{\mathbf{k},z}}\right]. \quad (27)$$

Here, $\lambda_{\mathbf{k},z} = v_{\mathbf{k},z}\tau_{\mathbf{k}} / w$, where w is the width of the sample in $\hat{z}$. By following the same procedure described in the development of Eqs. (24)-(26), we find

$$\kappa_{xz} = \kappa_{xz,bulk} - \frac{2}{V}\sum_{\lambda_{\mathbf{k},y}>0}\kappa_{\mathbf{k},xz}\lambda_{\mathbf{k},y}\left(1-\exp(-\frac{1}{\lambda_{\mathbf{k},y}})\right) - \frac{1}{V}\sum_{\lambda_{\mathbf{k},y}>0}\kappa_{\mathbf{k},xz}\int_{\eta'=0}^{1}\Delta T_z(\eta')\left(\exp\left(-\frac{1-\eta'}{\lambda_{\mathbf{k},y}}\right)-\exp\left(-\frac{\eta'}{\lambda_{\mathbf{k},y}}\right)\right)\frac{d\eta'}{\lambda_{\mathbf{k},z}}. \quad (28)$$

Subtracting Eq. (28) from Eq. (26) and rearranging,

$$\kappa_{zx} - \kappa_{xz} = -\frac{Lw}{V}\int_{\eta'=0}^{1}\Delta T_x(\eta')\left\{\sum_{\lambda_{\mathbf{k},y}>0}\frac{C_{\mathbf{k}}}{\tau_{\mathbf{k}}}\lambda_{\mathbf{k},z}\left(\exp\left(-\frac{1-\eta'}{\lambda_{\mathbf{k},y}}\right)-\exp\left(-\frac{\eta'}{\lambda_{\mathbf{k},y}}\right)\right)\right\}d\eta' + \frac{Lw}{V}\int_{\eta'=0}^{1}\Delta T_z(\eta')\left\{\sum_{\lambda_{\mathbf{k},y}>0}\frac{C_{\mathbf{k}}}{\tau_{\mathbf{k}}}\lambda_{\mathbf{k},x}\left(\exp\left(-\frac{1-\eta'}{\lambda_{\mathbf{k},y}}\right)-\exp\left(-\frac{\eta'}{\lambda_{\mathbf{k},y}}\right)\right)\right\}d\eta'. \quad (29)$$

Using the integral temperature solutions of the BTE (Eqs. (16) and (27) to simplify Eq. (29), we find

$$\kappa_{zx} - \kappa_{xz} = \frac{Lw}{V}\sum_{\lambda_{\mathbf{k},y}>0}\frac{C_{\mathbf{k}}}{\tau_{\mathbf{k}}}\int_{\eta=0}^{1}\int_{\eta'=0}^{1}\exp\left(-\frac{|\eta-\eta'|}{\lambda_{\mathbf{k},y}}\right)\left(\Delta T_x(\eta)\Delta T_z(\eta') - \Delta T_x(\eta')\Delta T_z(\eta)\right)\frac{d\eta'}{\lambda_{\mathbf{k},y}}d\eta. \quad (30)$$

Finally, using the same rationale leading to Eq. (23), the anti-symmetric integrand with equivalent limits of integration for Eq. (30)implies that $\kappa_{zx} - \kappa_{xz} = 0$. Therefore, the BTE solution shows that $\kappa_{zx} = \kappa_{xz}$.

Therefore, the BTE solutions show that the thermal conductivity tensor is always symmetric for arbitrarily aligned anisotropic thin films. Compared to the original diffusive Onsager relation, which was derived in the bulk regime and relies on the validity of Fourier's law [17], the BTE reciprocity relation is valid from the diffusive through the boundary scattering regime in which Fourier's law breaks down. Both reciprocity relations fundamentally arise from the time-reversal symmetry of the carrier dynamics[17], which are manifested in the inversion symmetry of the phonon dispersion and scattering rates.

5.3 Results and discussion of anisotropic thin film transport

5.3.1 Illustration and numerical validation of the Onsager relation

As a simple illustration of the reciprocity relation (Eq. (23)), we first consider heat transport in a model material with an anisotropic Debye dispersion relation[169]

$$\omega^2 = v_{ab}^2 k_{ab}^2 + v_c^2 k_c^2. \tag{31}$$

Here, v_{ab} and v_c (k_{ab} and k_c) are the group velocities (wavevectors) in the $\hat{ab}$ and $\hat{c}$ directions of the crystal. The crystal is rotated by an angle Ψ in the xy plane; at $\Psi = 0$, the $\hat{c}$ direction of the crystal is aligned with the $\hat{y}$ direction of the film. Figure 5-2(a) shows the reciprocal space representation of the iso-frequency ellipsoid for this anisotropic Debye dispersion relation, and illustrates the fact that the group velocity vectors are normal to the iso-ω surface (phonon focusing). For simplicity, and to emphasize the impact of the anisotropic dispersion, we consider a single phonon polarization, a spherical first Brillouin zone, and focus on the high temperature limit where $C_{\mathbf{k}} = k_B$ for all phonons. We also take the scattering to be gray ($\tau_{\mathbf{k}} = \tau$ for all $\mathbf{k}$).

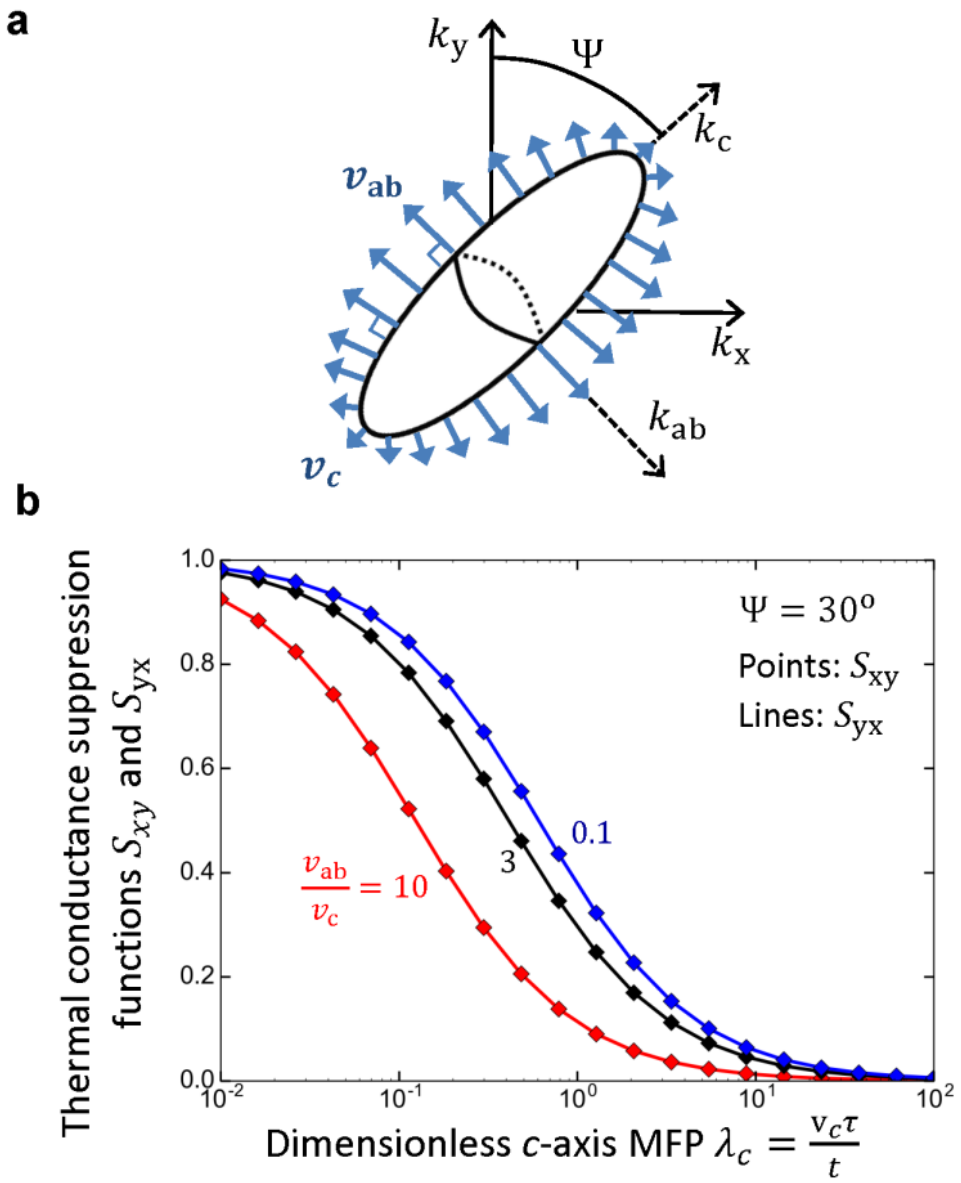

Figure 5-2: A numerical demonstration of the reciprocity relation $\kappa_{xy} = \kappa_{yx}$. (a) Reciprocal-space schematic of the iso-frequency ellipsoid for a material with an anisotropic Debye dispersion relation (Eq. (31)). The $\hat{c}$ axis of the material is tilted by an angle Ψ with respect to the $\hat{y}$ direction of the film. For simplicity we consider a constant relaxation time τ, high temperatures, and a spherical first Brillouin zone. (b) According to the reciprocity relation $\kappa_{xy} = \kappa_{yx}$ (Eq. (23)), the off-diagonal thermal conductivity suppression functions $S_{ij} = \kappa_{ij} / \kappa_{ij,bulk}$ are supposed to be equal ($S_{xy} = S_{yx}$) for all values of the dimensionless mean free path λ_c from the diffusive $(\lambda_c << 1)$ through the boundary scattering $(\lambda_c >> 1)$ regimes. Here this $S_{xy} = S_{yx}$ equality is verified numerically using Eqs. (19) and (20) for the particular case of $\Psi = 30^o$ and three values of the group velocity anisotropy ratio v_{ab} / v_c.

To quantify the impact of boundary scattering on the off-diagonal thermal conductivities, we define the suppression functions $S_{\mathrm{xy}} \equiv \kappa_{xy} / \kappa_{xy,bulk}$ and $S_{\mathrm{yx}} \equiv \kappa_{yx} / \kappa_{yx,bulk}$, which are the ratios of the actual BTE thermal conductivities to the bulk values. For the anisotropic Debye model considered here, S_{xy} and S_{yx} are functions of three dimensionless groups: the group velocity ratio v_{ab} / v_c, the tilt angle Ψ, and the dimensionless c-axis mean free path $\lambda_c \equiv v_c \tau / t$.

Figure 5-2 (b) shows the suppression functions S_{xy} (points) and S_{yx} (lines) as functions of λ_c for $\Psi = 30^o$ and three values of v_{ab} / v_c. We evaluated S_{xy} and S_{yx} numerically using two separate equations (Eq. (19) and Eq. (20)) and confirmed that $S_{\mathrm{xy}} = S_{\mathrm{yx}}$ over all parameter ranges considered (within 0.1% numerical precision). The fact that $S_{\mathrm{xy}} = S_{\mathrm{yx}}$ for all v_{ab} / v_c and λ_c in Figure 5-2(b) is a specific example of the general result $\kappa_{\mathrm{xy}} = \kappa_{\mathrm{yx}}$ (Eq. (23)). In Figure 5-2(b), we see that S_{xy} decreases for larger values of λ_c, representing the suppressed thermal transport due to boundary scattering. Interestingly, the difference in the suppression functions between $v_{ab} / v_c = 0.1$ and $v_{ab} / v_c = 3$ is relatively small despite the significant change in group velocity ratio, while increasing the velocity ratio to $v_{ab} / v_c = 10$ shifts the suppression function curves to smaller λ_c. This occurs because for $v_{ab} / v_c >> 1$, boundary scattering becomes more important for small λ_c due to the long mean free paths along the $\hat{ab}$-directions.

5.3.2 Comparison with atomistic simulations: arbitrarily aligned graphite

We next compare our BTE solution for arbitrarily aligned anisotropic thin films to recently published non-equilibrium molecular dynamics (NEMD) simulations [166]. The NEMD simulations apply cross-plane temperature differences to graphite films of various thicknesses and basal plane alignments. To characterize the basal plane alignment we use the same convention as in Figure 5-2 where the c-axis of graphite is tilted by an angle Ψ with respect to the $\hat{y}$ direction of the thin film: for example, Ψ=0^o represents the scenario where the basal plane is parallel to the film boundaries.

In these NEMD thickness-convergence studies [166], the thermal conductivity was defined as $\kappa_{yy,NEMD} \equiv -q_y / \frac{dT}{dy}$, where the temperature gradient $\frac{dT}{dy}$ within the film is smaller than the Fourier result $(T_c - T_h) / t$ due to the temperature jump at the boundary between the thermal reservoirs and the sample. This definition is reasonable within the context of NEMD simulations where $\frac{dT}{dy}$ is known, but in experiments where only q, $T_h - T_c$, and t are measured, the typical definition used in our BTE solutions

$\kappa_{yy} \equiv q_y t / (T_h - T_c)$ is more useful. Thus, to compare the atomistic results with our BTE predictions we apply the conversion $\kappa_{yy} = \kappa_{yy,NEMD}(-\frac{dT}{dy})(\frac{t}{T_h - T_c})$.

To obtain the BTE prediction, we first construct a simple analytical model describing phonon transport in graphite. Because graphite has highly anisotropic group velocities between the basal and cross-plane directions [169], the anisotropic Debye dispersion relation (Eq. 18) for degenerate polarizations simplifies to a quasi-2D dispersion, $\omega = v_{ab} k_{ab}$. Molecular dynamics simulations rely upon classical rather than Bose-Einstein statistics, so to compare with the NEMD simulations we take the specific heat of each phonon mode to be $C_{\mathbf{k}} = k_B$. As a first approximation, we also assume that the scattering is gray ($\tau_{\mathbf{k}} = \tau$ for all $\mathbf{k}$). The benefit of these approximations is that the cross-plane thermal conductivity suppression function $S_{yy} \equiv \kappa_{yy} / \kappa_{yy,bulk}$ becomes a universal function which only depends on the y-direction dimensionless mean free path $\lambda_y \equiv \Lambda \sin\Psi / t$, where $\Lambda \equiv v_{ab}\tau$. For example, under these approximations S_{yy} does not depend on the size or shape of the first Brillouin zone.

We use Λ as the only fitting parameter to compare the BTE solutions with the NEMD simulations. As shown in Figure 5-3, the BTE model is in good agreement with the non-dimensionalized NEMD results for 24 different (Ψ, t) pairings using $\Lambda = 103$ nm. We can assess the self-consistency of this fitting parameter by calculating the basal plane thermal conductivity using the quasi-2D expression $\kappa = \frac{1}{2} C v_{ab} \Lambda$ and comparing with the bulk NEMD values of κ. To determine κ, we use the same input parameters for graphite as in a previous modeling study [169]. We calculate $C = k_B \eta_{PUC}$, where $\eta_{PUC} = 5.56 * 10^{28}\ \mathrm{m^{-3}}$ is the primitive unit cell density, and we consider two degenerate polarizations with $v_{ab} = 13,200\ \mathrm{ms^{-1}}$. This value for v_{ab} was obtained by averaging the basal-plane group velocities of the acoustic TA and TL1 polarizations from Ref. [169]. We note that we neglect the thermal conductivity contribution from the third acoustic (TL2) polarization and from the optical polarizations due to the smaller basal-plane group velocities and velocity anisotropy ratios. Finally, using our fit value of Λ gives $\kappa = 1051\ \mathrm{Wm^{-1}K^{-1}}$, which is within 8% of the NEMD result $\kappa = 1140 \pm 30\ \mathrm{Wm^{-1}K^{-1}}$. This good agreement indicates that the one-parameter anisotropic Debye model combined with the BTE solution accurately describes the phonon transport in NEMD atomistic simulations.

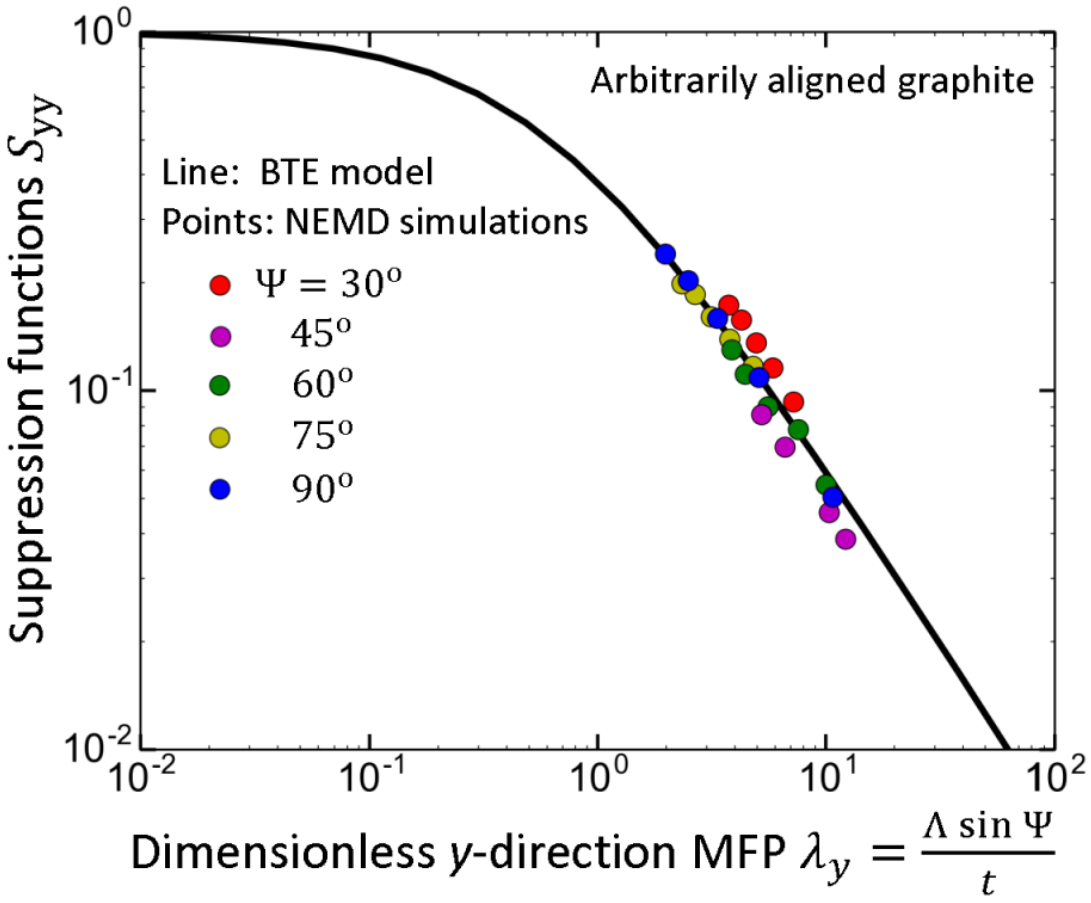

Figure 5-3: Comparing the analytical BTE solutions to atomistic simulations of arbitrarily aligned graphite[166]. The non-equilibrium molecular dynamics (NEMD) simulations were performed for 24 combinations of basal plane alignment angles Ψ (see Figure 5-2) and film thickness t. The BTE model for highly anisotropic layered materials agrees well with the numerical results using a gray mean free path $\Lambda = 103$ nm.

While the NEMD simulations can only be performed for relatively small thicknesses (t < 45 nm here) due to computational constraints, the BTE solutions can be readily applied for a broader range of film thicknesses, as emphasized by the much larger span of the line as compared to the points in Figure 5-3. The analytical BTE solution also provides insight into the size effects observed in the NEMD simulations: the most crucial parameter dictating the thermal conductivity suppression is the y-component of the mean free path, as also observed by Minnich for aligned thin films [144].

5.3.3 Case study: In-plane off-diagonal transport in black phosphorus

The thermal properties of black phosphorus nanostructures have received recent attention [146], [170]–[174] due to potential applications of black phosphorus or few-layer black phosphorene in nanoelectronics, optoelectronics, and thermoelectric energy conversion [16]. For example, the anisotropic in-plane electrical and optical properties

of black phosphorus have been leveraged to demonstrate a polarization-sensitive broadband photodetector [175]. The thermal design of such black phosphorus devices will require an understanding of how the heat transfer rates depend on the orientation of the temperature gradient with respect to the crystal structure.

Single-crystal black phosphorus has a larger thermal conductivity along the in-plane zigzag direction (κ_{ZZ}) than in the orthogonal in-plane armchair direction (κ_{AC}), with recently measured room temperature anisotropy ratios $r \equiv \kappa_{ZZ} / \kappa_{AC}$ of $r = 2.5-3$ [146], [171]–[173]. Due to this in-plane anisotropy, a temperature gradient $\frac{dT}{dx}$ imposed in the $\hat{x}$ direction oriented at an angle θ to the armchair direction induces a heat flow $q_z = -\kappa_{zx}\frac{dT}{dx}$ in the orthogonal $\hat{z}$ direction (see inset of Fig. 4). In the bulk regime, classic tensor rotation identities[176] show that $\kappa_{zx} = \frac{1}{2}(\kappa_{ZZ} - \kappa_{AC})\sin(2\theta)$. We will now show that our BTE solutions predict that this same simple identity applies for black phosphorus thin films even in the boundary scattering regime. We will then leverage previous first-principles calculations [146] to model $\kappa_{zx}(t,\theta)$ of black phosphorus thin films.

We first consider in-plane thermal transport of aligned thin films (i.e. Ψ =0 in Figure 5-2). We consider a temperature difference imposed along $\hat{x}$ and want to determine the heat flow in $\hat{z}$ using the off-diagonal conductivity κ_{zx}. In the (x, y, z) coordinate system of Figure 5-1, the off-diagonal conductivity κ_{zx} (Eq. (26)) of an aligned film is

$$\kappa_{zx} = \frac{2}{V}\sum_{\lambda_{\mathbf{k},y}>0} C_{\mathbf{k}} v_{\mathbf{k},x} v_{\mathbf{k},z} \tau_{\mathbf{k}} \left[1 - \lambda_{\mathbf{k},y}\left(1 - \exp(-\frac{1}{\lambda_{\mathbf{k},y}})\right)\right]. \quad (32)$$

If we instead choose to express the group velocity projections $v_{\mathbf{k},x}$ and $v_{\mathbf{k},z}$ in an alternate coordinate system (x', y, z') that is rotated about the y axis by an angle θ, Eq. (32) becomes

$$\kappa_{zx} = \frac{2}{V}\sum_{\lambda_{\mathbf{k},y}>0} C_{\mathbf{k}} \left(v_{\mathbf{k},x'}\cos(\theta) + v_{\mathbf{k},z'}\sin(\theta)\right)\left(-v_{\mathbf{k},x'}\sin(\theta) + v_{\mathbf{k},z'}\cos(\theta)\right)\tau_{\mathbf{k}} \left[1 - \lambda_{\mathbf{k},y}\left(1 - \exp(-\frac{1}{\lambda_{\mathbf{k},y}})\right)\right]. \quad (33)$$

Note that Eqs. (32) and (33) are simply different mathematical representations of the same physical quantity κ_{zx}. Multiplying out the different group velocity terms and rearranging, Eq. (33) can be written as

$$\kappa_{zx} = \cos(\theta)\sin(\theta)\left\{\frac{2}{V}\sum_{\lambda_{\mathbf{k},y}>0} C_{\mathbf{k}} v_{\mathbf{k},z'} v_{\mathbf{k},z'} \tau_{\mathbf{k}} \left[1-\lambda_{\mathbf{k},y}\left(1-\exp(-\frac{1}{\lambda_{\mathbf{k},y}})\right)\right]\right\}$$
$$-\cos(\theta)\sin(\theta)\left\{\frac{2}{V}\sum_{\lambda_{\mathbf{k},y}>0} C_{\mathbf{k}} v_{\mathbf{k},x'} v_{\mathbf{k},x'} \tau_{\mathbf{k}} \left[1-\lambda_{\mathbf{k},y}\left(1-\exp(-\frac{1}{\lambda_{\mathbf{k},y}})\right)\right]\right\} \quad (34)$$
$$+\left(\cos^2(\theta)-\sin^2(\theta)\right)\left\{\frac{2}{V}\sum_{\lambda_{\mathbf{k},y}>0} C_{\mathbf{k}} v_{\mathbf{k},x'} v_{\mathbf{k},z'} \tau_{\mathbf{k}} \left[1-\lambda_{\mathbf{k},y}\left(1-\exp(-\frac{1}{\lambda_{\mathbf{k},y}})\right)\right]\right\}.$$

However, the terms from Eq. (34) in braces are identical to the BTE predictions of the conductivities $\kappa_{z'z'}$, $\kappa_{x'x'}$, and $\kappa_{x'z'}(=\kappa_{z'x'})$ that would be identified if temperature gradients and heat fluxes were imposed and measured in the (x', y, z') coordinate system. Therefore, our BTE solutions lead to the simple transformation identity

$$\kappa_{zx} = \frac{1}{2}(\kappa_{z'z'} - \kappa_{x'x'})\sin(2\theta) + \kappa_{z'x'}\cos(2\theta), \quad (35)$$

where we have used the trigonometric identities $\cos(\theta)\sin(\theta) = \sin(2\theta)/2$ and $\cos^2(\theta) - \sin^2(\theta) = \cos(2\theta)$.

We will now show that Eq. (35) also holds for the more general case of in-plane rotations of arbitrarily aligned films (i.e. $\Psi \neq 0$ in Figure 5-2). A temperature gradient $-(T_h - T_c)/L_x$ imposed along $\hat{x}$ induces a cross-plane deviational temperature profile $\Delta T_x(\eta)$, which is found by solving the integral form of the BTE (Eq. (16)). Rearranging Eq. (16) to separate $\Delta T_x(\eta)$ from terms that depend on $v_{\mathbf{k},x}$ gives

$$\sum_{\lambda_{\mathbf{k},y}>0} \frac{C_{\mathbf{k}}}{\tau_{\mathbf{k}}}\left(2\Delta T_x(\eta) - \int_{\eta'=0}^{1} \Delta T_x(\eta')\exp\left(-\frac{|\eta-\eta'|}{\lambda_{\mathbf{k},y}}\right)\frac{d\eta'}{\lambda_{\mathbf{k},y}}\right)$$
$$= \sum_{\lambda_{\mathbf{k},y}>0} \frac{C_{\mathbf{k}} v_{\mathbf{k},x}}{L_x}\left[\exp\left(-\frac{1-\eta}{\lambda_{\mathbf{k},y}}\right) - \exp\left(-\frac{\eta}{\lambda_{\mathbf{k},y}}\right)\right]. \quad (36)$$

Due to the arbitrary choice of in-plane direction $\hat{x}$, analogous expressions for the deviational temperature profiles $\Delta T_{x'}(\eta)$ ($\Delta T_{z'}(\eta)$) due to a temperature gradient $(T_h - T_c)/L_{x'}$ ($(T_h - T_c)/L_{z'}$) imposed along in-plane directions x' (z') can be immediately written down by simply changing the subscript x to x' (z') in Eq. (36).

If we choose to express Eq. (36) for $\Delta T_x(\eta)$ in the rotated (x', y, z') coordinate system, we can use the relation $v_{\mathbf{k},x} = v_{\mathbf{k},x'}\cos(\theta) + v_{\mathbf{k},z'}\sin(\theta)$ to write Eq. (36) as

$$\sum_{\lambda_{\mathbf{k},y}>0}\frac{C_{\mathbf{k}}}{\tau_{\mathbf{k}}}\left(2\Delta T_x(\eta)-\int_{\eta'=0}^{1}\Delta T_x(\eta')\exp\left(-\frac{|\eta-\eta'|}{\lambda_{\mathbf{k},y}}\right)\frac{d\eta'}{\lambda_{\mathbf{k},y}}\right)$$
$$=\cos(\theta)\frac{L_{x'}}{L_x}\sum_{\lambda_{\mathbf{k},y}>0}\frac{C_{\mathbf{k}}v_{\mathbf{k},x'}}{L_{x'}}\left[\exp\left(-\frac{1-\eta}{\lambda_{\mathbf{k},y}}\right)-\exp\left(-\frac{\eta}{\lambda_{\mathbf{k},y}}\right)\right] \quad (37)$$
$$+\sin(\theta)\frac{L_{z'}}{L_x}\sum_{\lambda_{\mathbf{k},y}>0}\frac{C_{\mathbf{k}}v_{\mathbf{k},z'}}{L_{z'}}\left[\exp\left(-\frac{1-\eta}{\lambda_{\mathbf{k},y}}\right)-\exp\left(-\frac{\eta}{\lambda_{\mathbf{k},y}}\right)\right].$$

The two terms on the RHS of Eq. (37) also appear in the RHS of integral equation solutions for $\Delta T_{x'}(\eta)$ and $\Delta T_{z'}(\eta)$ that are analogous to Eq. (36). After substituting these integral equations, Eq. (37) can be written as

$$\sum_{\lambda_{\mathbf{k},y}>0}\frac{C_{\mathbf{k}}}{\tau_{\mathbf{k}}}\left(2\Delta T_x(\eta)-\int_{\eta'=0}^{1}\Delta T_x(\eta')\exp\left(-\frac{|\eta-\eta'|}{\lambda_{\mathbf{k},y}}\right)\frac{d\eta'}{\lambda_{\mathbf{k},y}}\right)$$
$$=\cos(\theta)\frac{L_{x'}}{L_x}\sum_{\lambda_{\mathbf{k},y}>0}\frac{C_{\mathbf{k}}}{\tau_{\mathbf{k}}}\left(2\Delta T_{x'}(\eta)-\int_{\eta'=0}^{1}\Delta T_{x'}(\eta')\exp\left(-\frac{|\eta-\eta'|}{\lambda_{\mathbf{k},y}}\right)\frac{d\eta'}{\lambda_{\mathbf{k},y}}\right) \quad (38)$$
$$+\sin(\theta)\frac{L_{z'}}{L_x}\sum_{\lambda_{\mathbf{k},y}>0}\frac{C_{\mathbf{k}}}{\tau_{\mathbf{k}}}\left(2\Delta T_{z'}(\eta)-\int_{\eta'=0}^{1}\Delta T_{z'}(\eta')\exp\left(-\frac{|\eta-\eta'|}{\lambda_{\mathbf{k},y}}\right)\frac{d\eta'}{\lambda_{\mathbf{k},y}}\right)$$

By substituting into Eq. (38), it can be shown that the deviational temperature profile due to a temperature gradient along $\hat{x}$ is $\Delta T_x(\eta)=\left(L_{x'}\Delta T_{x'}(\eta)\cos(\theta)+L_{z'}\Delta T_{z'}(\eta)\sin(\theta)\right)/L_x$. We note that our final results will not depend on the macroscopic dimensions $L_{x'}$, $L_{z'}$, or L_x.

For arbitrarily aligned films, the off-diagonal thermal conductivity κ_{zx} is (Eq. (32))

$$\kappa_{zx}=\frac{2}{V}\sum_{\lambda_{\mathbf{k},y}>0}\kappa_{\mathbf{k},xz}\left[1-\lambda_{\mathbf{k},y}\left(1-\exp(-\frac{1}{\lambda_{\mathbf{k},y}})\right)-\int_{\eta'=0}^{1}\Delta T_x(\eta')\left(\exp\left(-\frac{1-\eta'}{\lambda_{\mathbf{k},y}}\right)-\exp\left(-\frac{\eta'}{\lambda_{\mathbf{k},y}}\right)\right)\frac{d\eta'}{2\lambda_{\mathbf{k},x}}\right]. \quad (39)$$

Expressing $v_{\mathbf{k},x}$, $v_{\mathbf{k},z}$, and $\Delta T_x(\eta)$ in the rotated (x',y,z') coordinate system, we see that

$$\kappa_{zx}=\frac{\sin(2\theta)}{2}\left\{\frac{2}{V}\sum_{\lambda_{\mathbf{k},y}>0}\kappa_{\mathbf{k},z'z'}\left[1-\lambda_{\mathbf{k},y}\left(1-\exp(-\frac{1}{\lambda_{\mathbf{k},y}})\right)-\int_{\eta'=0}^{1}\Delta T_{z'}(\eta')\left(\exp\left(-\frac{1-\eta'}{\lambda_{\mathbf{k},y}}\right)-\exp\left(-\frac{\eta'}{\lambda_{\mathbf{k},y}}\right)\right)\frac{d\eta'}{2\lambda_{\mathbf{k},z'}}\right]\right\}$$
$$-\frac{\sin(2\theta)}{2}\left\{\frac{2}{V}\sum_{\lambda_{\mathbf{k},y}>0}\kappa_{\mathbf{k},x'x'}\left[1-\lambda_{\mathbf{k},y}\left(1-\exp(-\frac{1}{\lambda_{\mathbf{k},y}})\right)-\int_{\eta'=0}^{1}\Delta T_{x'}(\eta')\left(\exp\left(-\frac{1-\eta'}{\lambda_{\mathbf{k},y}}\right)-\exp\left(-\frac{\eta'}{\lambda_{\mathbf{k},y}}\right)\right)\frac{d\eta'}{2\lambda_{\mathbf{k},x'}}\right]\right\} \quad (40)$$
$$+\cos^2(\theta)\left\{\frac{2}{V}\sum_{\lambda_{\mathbf{k},y}>0}\kappa_{\mathbf{k},x'z'}\left[1-\lambda_{\mathbf{k},y}\left(1-\exp(-\frac{1}{\lambda_{\mathbf{k},y}})\right)-\int_{\eta'=0}^{1}\Delta T_{x'}(\eta')\left(\exp\left(-\frac{1-\eta'}{\lambda_{\mathbf{k},y}}\right)-\exp\left(-\frac{\eta'}{\lambda_{\mathbf{k},y}}\right)\right)\frac{d\eta'}{2\lambda_{\mathbf{k},x'}}\right]\right\}$$
$$-\sin^2(\theta)\left\{\frac{2}{V}\sum_{\lambda_{\mathbf{k},y}>0}\kappa_{\mathbf{k},z'x'}\left[1-\lambda_{\mathbf{k},y}\left(1-\exp(-\frac{1}{\lambda_{\mathbf{k},y}})\right)-\int_{\eta'=0}^{1}\Delta T_{z'}(\eta')\left(\exp\left(-\frac{1-\eta'}{\lambda_{\mathbf{k},y}}\right)-\exp\left(-\frac{\eta'}{\lambda_{\mathbf{k},y}}\right)\right)\frac{d\eta'}{2\lambda_{\mathbf{k},z'}}\right]\right\}.$$

The first two terms in braces on the RHS of Eq. (40) are simply $\kappa_{z'z'}$ and $\kappa_{x'x'}$, while the last two terms in braces are $\kappa_{z'x'}$ and $\kappa_{x'z'}$. Using the Onsager relation $\kappa_{z'x'}=\kappa_{x'z'}$ Eq. (40) can be finally written as $\kappa_{zx}=\frac{1}{2}(\kappa_{z'z'}-\kappa_{x'x'})\sin(2\theta)+\kappa_{x'z'}\cos(2\theta)$.

Thus, we have proved that the same tensor rotation rules that applies to Fourier heat conduction [176] also apply for in-plane rotations in the thin film boundary scattering regime. This relationship indicates that it is not necessary to independently measure the in-plane thermal conductivity as a function of many directions θ, even for a very thin film in which κ_{zx} will be dramatically reduced from its bulk value due to boundary scattering. Instead, only a maximum of three independent in-plane components need to be determined for a given t, and then Eq. (35) can be used to calculate κ_{zx} for any arbitrary θ.

For our example of black phosphorus thin films with $\Psi=0$, Eq. (35) further simplifies to $\kappa_{zx}=\frac{1}{2}(\kappa_{ZZ}-\kappa_{AC})\sin(2\theta)$. Recently, Smith et al. [146] performed first-principles calculations to determine both the harmonic and anharmonic force constants required to find κ_{ZZ} and κ_{AC} of pure samples (no impurity scattering) without any fitting parameters. They also used the BTE solution for in-plane thin film boundary scattering in aligned materials [144] to calculate $\kappa_{ZZ}(t)$ and $\kappa_{AC}(t)$. Here, we combine these first-principles predictions of $\kappa_{ZZ}(t)$ and $\kappa_{AC}(t)$ with the rotation transformation rule (Eq. (35)) to predict $\kappa_{zx}(\theta,t)$ of black phosphorus thin films. Figure 5-4 shows the BTE predictions for κ_{zx} as a function of rotation angle for four different film thicknesses. Due to the large conductivity contrast between $\kappa_{ZZ}(t)$ and $\kappa_{AC}(t)$, the off-diagonal component $\kappa_{zx}(t)$ can be as large as 33 $\mathrm{Wm^{-1}K^{-1}}$ for thick films (t=10 μm). Even for films as thin as t=10 nm, κ_{zx} can be as large as 18 $\mathrm{Wm^{-1}K^{-1}}$, indicating that the thermal conductivity suppression from boundary scattering is relatively weak due to the phonon focusing along the in-plane directions.

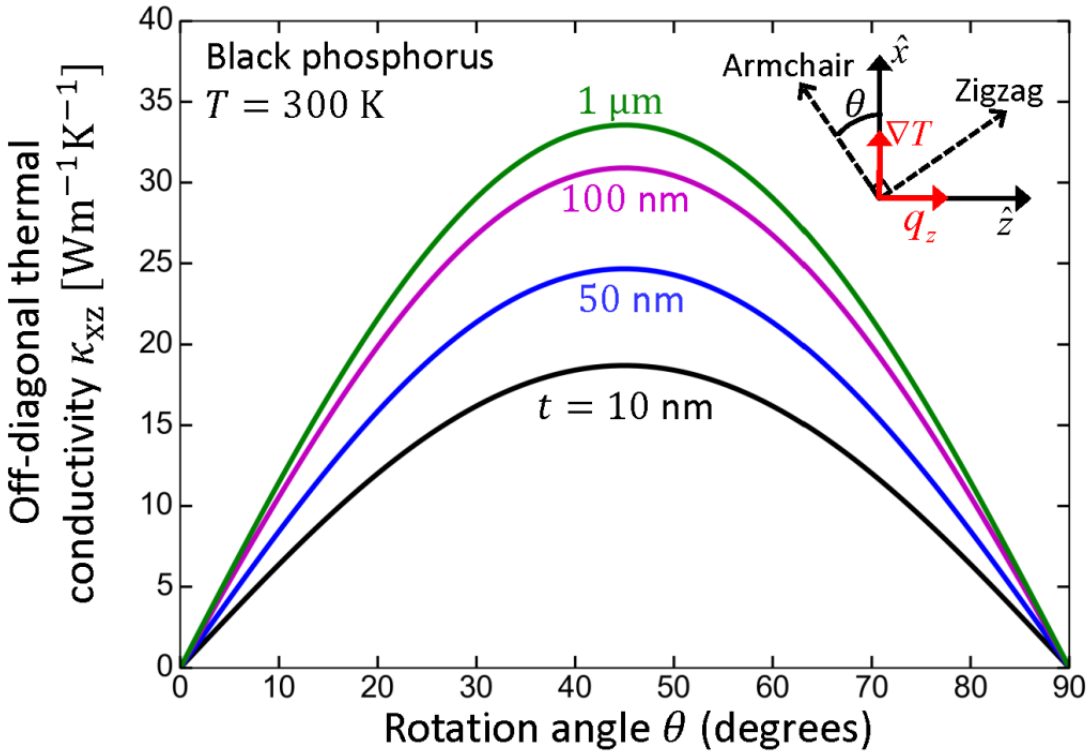

Figure 5-4: Thin-film boundary scattering reduces the off-diagonal in-plane thermal conductivity κ_{xz} of black phosphorus. The BTE solutions show that κ_{xz} can be determined for a given in-plane temperature gradient rotation angle θ using simple tensor transformation identities, even in the boundary scattering regime. We use recent first-principles calculations [146] of thickness-dependent κ along the zigzag and armchair directions at room temperature to calculate $\kappa_{xz}(\theta,t)$ for aligned black phosphorus thin films ($\Psi = 0$).

These predictions for $\kappa_{zx}(t)$ of black phosphorus thin films contain no free parameters and can be used to model the thermal dissipation performance of electronic and optoelectronics devices of any in-plane orientation, enabling improved thermal design of black phosphorus photodetectors, thermoelectric devices, or transistors. The tensor rotation relation derived here can also be readily applied to study thermal transport in other materials of recent interest with anisotropic in-plane thermal conductivities, including ReS_2 [152] and black arsenic [177].

5.3.4 Discussion: Connection to recent experimental methods

The BTE solutions and Onsager proof presented here support recently developed experimental tools to measure the off-diagonal terms of the thermal conductivity tensor. Feser, Liu, and Cahill [178] developed new "beam offset" time-domain thermoreflectance (TDTR) measurement techniques to measure the full $\boldsymbol{\kappa}$ tensor of thin films and bulk materials. The analysis in Ref. [178] implicitly assumed that the Onsager relation holds even for thin films, an assumption which our BTE solution shows

to be rigorously justified. This beam offset method has recently been used to measure the diagonal components of the $\boldsymbol{\kappa}$ tensor of bulk black phosphorus as a function of rotation angle θ [172], and it should be straightforward to extend such measurements to a thin film sample to measure $\kappa_{xz}(\theta,t)$ as suggested here in Figure 5-4. In another class of measurements, Mishra *et al*.[179] used an electrothermal technique to measure the off-diagonal conductivity of arbitrarily aligned bulk mica. This off-diagonal measurement technique could plausibly be extended to thin films by adapting elements of the multiple-sensor "two-omega" method of Ramu and Bowers [180] or of the anisotropic thin film measurements of Ju, Kurabayashi, and Goodson [181]. Lastly, the zigzag and armchair thermal conductivities of black phosphorus nanoribbons have been measured using suspended heater/thermometer platforms [170] and suspended beams[146]. By measuring multiple samples of different alignments, these suspended device measurements could also be used to determine the in-plane off-diagonal component κ_{xz} and κ_{zx} of arbitrarily aligned nanostructures. Thus, several optical and/or electrothermal microscale thermal measurement techniques could be used to test the thin film Onsager relation predicted by the BTE theory, and the Onsager relation can likewise be used to simplify the analysis and measurement of systems containing anisotropic thin films.

5.4 Summary and future directions

To summarize, we identified an Onsager reciprocity relation for ballistic phonon transport in thin films. This reciprocity relation states that the thermal conductivity tensor is symmetric from the diffusive regime through the thin film boundary scattering regime, extending Onsager's original reciprocity relation for anisotropic heat conduction to capture ballistic phonon transport effects. We illustrated the boundary scattering suppression and reciprocity relation using a simple model for anisotropic materials, compared the BTE solutions to atomistic simulations[166] of arbitrarily aligned graphite, and modeled thin-film size effects on the off-diagonal thermal conductivity of rotated black phosphorus using previous first-principles calculations of only the principal components[146]. This thermal conductivity reciprocity relation reduces the number of independent measurements that are required to fully characterize thermal transport in anisotropic thin films.

Future work modeling anisotropic nanostructures could further develop the Boltzmann transport equation solutions described here. One main assumption made in this work is the relaxation time approximation (RTA). Extending the Onsager proof beyond the RTA would further illustrate the fundamental symmetries of heat transport in anisotropic nanostructures. Another area of recent modeling interest is phonon hydrodynamic heat transfer[182], which occurs when the momentum-conserving "normal" phonon-phonon collision scattering dominate over the Umklapp scattering rates[183]. Boltzmann equation modeling and analytical solutions of the hydrodynamic heat transfer in arbitrarily aligned anisotropic thin films could further elucidate this novel heat transfer mechanism.

Chapter 6 : Summary and future directions

6.1 Summary

This dissertation has made contributions to the measurement and theory of heat conduction in complicated nanostructures, as summarized below.

Chapter 2 describes the development of a non-contact nanothermometry technique in the scanning transmission electron microscope (STEM). Unlike previous STEM temperature mapping techniques which measure small thermal strains or phase-change events, we instead measure temperature-dependent thermal diffuse scattering (TDS). TDS is a promising technique because all materials display temperature dependent TDS, and the diffuse scattering is an inherently local temperature indicator. We demonstrate STEM diffraction pattern thermometry by obtaining a diffraction pattern at different locations of an isothermal sample. In post-processing, we calculate the diffuse counts in the background of the diffraction pattern. Carefully choosing the imaging conditions and using energy filters allows diffuse count measurements to be performed even for weakly scattering samples. By comparing the diffuse counts from a gold foil at $\mathrm{T} = 300\ \mathrm{K}$ and $\mathrm{T} = 100\ \mathrm{K}$, we find a position-averaged TDS temperature coefficient of 2400 ± 400 ppm/K. This measurement is in order-of-magnitude agreement with a simple Debye-Waller estimate. This diffraction pattern nanothermometry technique is most easily applied for single crystal materials which have relatively simple diffraction patterns.

Chapter 3 discusses a second STEM TDS measurement technique that uses the annular dark field (ADF) detector. This ADF technique is readily applied to polycrystalline materials, and small changes in the ADF signal can be measured with a lock-in amplifier to improve the temperature sensitivity. We implement a lock-in technique by time-periodically Joule heating a MEMS *in-situ* device and measuring the small periodic changes in the ADF signal due to the temperature rise. We find that continually scanning the beam over a 100 by 100 nanometer region during the Joule heating substantially reduces thermal drift artifacts on the ADF signal. We calibrate the ADF response as a function of temperature rise $\Delta\mathrm{T}$ above 500$^{\mathrm{o}}$C for silicon carbide and tungsten, and find that the ADF temperature coefficient varies by <10% at different sample positions. The lock-in detection enables improved temperature sensitivities of $12\ \mathrm{K\ Hz}^{-1/2}$ at each sample location. This improved sensitivity allows us to use the calibrated ADF signal to obtain an *in-situ* temperature rise map of a Joule-heated silicon carbide device. We compare this experimental result with finite-element method electrothermal simulations, and also show that the ADF technique can be used to map temperature rises around a Joule-heated metallic line at room temperature.

Chapter 4 uses ray tracing simulations to quantify boundary scattering in geometrically complicated nanostructures known as silicon nanomeshes. Several mechanisms have been proposed to explain measured k reductions in nanomeshes, but it was not known whether incoherent phonon boundary scattering effects or coherent phonon wave interference effects dominate the transport. To compare the boundary

scattering theory with experimental measurements, we develop ray tracing simulations to provide rigorous calculations of the boundary scattering mean free path in complicated geometries. We describe the computational implementation of the ray tracing, and validate the simulations against previous numerical BTE solutions and experiments, observing excellent agreement. We then use the simulation results to model silicon nanomesh experiments. The good agreement between the ray tracing results and experiments indicates that that coherent phonon effects are not important for nanomesh pitches greater than 100 nm or temperatures above 14 K. The ray tracing results also indicate that phonon backscattering, an incoherent boundary scattering effect, leads to the further reduction of k in short pitch nanomeshes.

Chapter 5 focuses on analytical modeling of heat transfer in arbitrarily aligned anisotropic thin films. We solved the governing Boltzmann Transport Equation (BTE) for both in-plane and cross-plane heat transfer, quantifying the prediction of boundary scattering theory in anisotropic nanostructures. We used the BTE solutions to identify an Onsager reciprocity relation for ballistic phonon transport in thin films, showing that the thermal conductivity tensor is symmetric from the diffusive regime through the thin film boundary scattering regime. We illustrated the boundary scattering suppression and reciprocity relation using a simple model for anisotropic materials, compared the BTE solutions to atomistic simulations[166] of arbitrarily aligned graphite thin films, and modeled thin-film size effects on the off-diagonal thermal conductivity of rotated black phosphorus using previous first-principles calculations of only the principal components[146]. This thermal conductivity reciprocity relation reduces the number of independent measurements that are required to fully characterize thermal transport in anisotropic thin films.

6.2 Future directions

Certainly, much work still needs to be done to implement nanoscale temperature mapping of complicated nanostructures, and to further the theory of boundary scattering in complex geometries. Many of these concepts were summarized at the end of each chapter. Thinking beyond these immediate goals, the work of this dissertation also motivates the long-term research directions described below

6.2.1 Nanothermometry spatial resolution quantification

A key parameter of any nanothermometry technique is the spatial resolution. Although best-case limits on the spatial resolution can often be inferred from physical arguments (*i.e.* the spatial resolution of the ADF STEM technique is certainly no better than the 100 by 100 nm scan window), experimental quantification of the resolution is not straightforward. Rigorous spatial resolution requires knowledge of the point spread function (PSF) of the thermometry probe. This PSF is convolved with the true temperature to produce the measured temperature profile. The sharper the true temperature profile is, the easier it will be to experimentally determine the PSF from the measured profile. A standardized sample with a known nanoscale temperature profile would enable direct measurement of the thermal spread function and comparison of nanothermometry techniques. Potentially appealing samples could

leverage small ion-milled gaps between hot and cold regions; localized heating due to interfacial resistances (or cooling due to Peltier effects); or Joule-heated nanowires. Unfortunately, some technique-specific limitations may impede the development of a single universal thermal spread function standard. For example, thick and inflexible samples which are desirable for scanning thermal microscopy cannot be imaged in the STEM because they are not electron transparent. Long-term work to develop appropriate nanothermometry standard samples would prove useful for engineers and scientists measuring temperature in complicated nanostructures.

6.2.2 Combining high spatial and temporal resolution thermometry

Nanoscale systems often display a rapid thermal response because of their small sizes. For example, the thermal diffusion time τ_d for heat flow through a silicon nanowire with a $10\ \mu\text{m}$ length is $\tau_d \sim L^2/\alpha = 3\ \mu s$ for an estimated thermal diffusivity $\alpha = (50\ \text{Wm}^{-1}\text{K}^{-1})/(1.6 * 10^6\ \text{J m}^{-3}\text{K}^{-1})$. Even more dramatically, the ballistic heat propagation time across a $d = 100\ \text{nm}$ thin silicon film is $\tau_b \sim \frac{d}{v_s} = 12.5\ \text{ps}$ for a sound velocity of $v_s = 8000\ \text{ms}^{-1}$. A frontier research challenge is developing techniques that can resolve both the time evolution and the spatial dependence of these nanoscale temperature gradients near room temperature. This combined spatial and temporal resolution would enable improved thermal design of HAMR devices and microelectronics, both of which operate under transient conditions. Time-resolved or ultrafast electron microscopy[184], [185] may be promising pathways forward for transient nanothermometry, but careful studies of beam heating artifacts distorting the temperature profile will also be important.

6.2.3 Simulating the crossover from coherent to incoherent phonon transport

Many existing simulation tools for phonon transport in nanostructures are only valid in either the incoherent regime or the coherent regime, and cannot quantitatively model experiments in this crossover regime[98]. For example, incoherent BTE models are not easily modified to include coherent phonon wave effects, while the majority of atomistic Green's function [186] methods are fully coherent and do not include phase-randomizing interactions. Molecular dynamics simulations can capture both regimes, but this atomistic technique is computationally limited to relatively small samples, and is inapplicable at the temperatures where coherent effects are important because classical occupation statistics do not apply at low temperatures. Developing new mesoscopic simulations that apply in the crossover regime would enable more accurate comparison with experiment and qualitative understanding of coherent thermal phonon effects. Theories developed to describe thermal photon transport in optical multilayers[118] are likely source of inspiration for phonon coherence. Lastly, it may be worthwhile to investigate whether incoherent ray tracing techniques can be modified to include coherence effects by tracking the phonon phase. Potential advantages of coherent ray tracing simulations include the ability to handle specular or diffuse interface scattering in complicated geometries with larger sample sizes than can be considered using atomistic methods.

References

[1] G. Chen, *Nanoscale Energy Transport and Conversion*. 2005.

[2] C. Dames and L. M. Jiji, “Microscale conduction,” in *Heat Conduction*, 2009.

[3] F. Yang and C. Dames, “Mean free path spectra as a tool to understand thermal conductivity in bulk and nanostructures,” *Phys. Rev. B*, vol. 87, no. 3, p. 035437, Jan. 2013.

[4] K. Fuchs and N. F. Mott, “The conductivity of thin metallic films according to the electron theory of metals,” *Math. Proc. Cambridge Philos. Soc.*, vol. 34, no. 01, p. 100, Oct. 1938.

[5] E. H. Sondheimer, “The mean free path of electrons in metals,” *Adv. Phys.*, vol. 1, no. 1, pp. 1–42, 1952.

[6] D. G. Cahill, “Analysis of heat flow in layered structures for time-domain thermoreflectance,” *Rev. Sci. Instrum.*, vol. 75, no. 12, p. 5119, 2004.

[7] A. J. Schmidt, R. Cheaito, and M. Chiesa, “A frequency-domain thermoreflectance method for the characterization of thermal properties.,” *Rev. Sci. Instrum.*, vol. 80, no. 9, p. 094901, Sep. 2009.

[8] C. Dames, “Measuring the thermal conductivity of thin films: 3 omega and related electrothermal methods,” in *Annual Review of Heat Transfer*, 2013, pp. 7–49.

[9] J. Kim, E. Ou, D. P. Sellan, and L. Shi, “A four-probe thermal transport measurement method for nanostructures,” *Rev. Sci. Instrum.*, vol. 86, no. 4, p. 044901, 2015.

[10] A. M. Marconnet, M. Asheghi, and K. E. Goodson, “From the Casimir Limit to Phononic Crystals: 20 Years of Phonon Transport Studies Using Silicon-on-Insulator Technology,” *J. Heat Transfer*, vol. 135, no. 6, p. 061601, 2013.

[11] J.-K. Yu, S. Mitrovic, D. Tham, J. Varghese, and J. R. Heath, “Reduction of thermal conductivity in phononic nanomesh structures.,” *Nat. Nanotechnol.*, vol. 5, no. 10, pp. 718–721, 2010.

[12] P. E. Hopkins, C. M. Reinke, M. F. Su, R. H. Olsson, E. a. Shaner, Z. C. Leseman, J. R. Serrano, L. M. Phinney, and I. El-Kady, “Reduction in the thermal conductivity of single crystalline silicon by phononic crystal patterning,” *Nano Lett.*, vol. 11, no. 1, pp. 107–112, 2011.

[13] S. Alaie, D. F. Goettler, M. Su, Z. C. Leseman, C. M. Reinke, and I. El-Kady, “Thermal transport in phononic crystals and the observation of coherent phonon scattering at room temperature,” *Nat. Commun.*, vol. 6, p. 7228, 2015.

[14] L.-D. Zhao, S.-H. Lo, Y. Zhang, H. Sun, G. Tan, C. Uher, C. Wolverton, V. P. Dravid,

and M. G. Kanatzidis, “Ultralow thermal conductivity and high thermoelectric figure of merit in SnSe crystals.,” *Nature*, vol. 508, no. 7496, pp. 373–377, Apr. 2014.

[15] S. Lee, K. Hippalgaonkar, F. Yang, J. Hong, C. Ko, J. Suh, K. Liu, K. Wang, J. J. Urban, X. Zhang, C. Dames, S. A. Hartnoll, O. Delaire, and J. Wu, “Anomalously low electronic thermal conductivity in metallic vanadium dioxide,” *Science*, vol. 355, no. 6323, pp. 371–374, 2016.

[16] X. Ling, H. Wang, S. Huang, F. Xia, and M. S. Dresselhaus, “The renaissance of black phosphorus,” *Proc. Natl. Acad. Sci.*, vol. 112, no. 15, pp. 4523–4530, 2015.

[17] L. Onsager, “Reciprocal relations in irreversible processes (I),” *Phys. Rev.*, vol. 37, pp. 405–426, 1931.

[18] C. Monachon, L. Weber, and C. Dames, “Thermal Boundary Conductance :A Materials Science Perspective,” *Annu. Rev. Mater. Res.*, 2016.

[19] M. N. Luckyanova, J. Garg, K. Esfarjani, A. Jandl, M. T. Bulsara, A. J. Schmidt, A. J. Minnich, S. Chen, M. S. Dresselhaus, Z. Ren, E. A. Fitzgerald, and G. Chen, “Coherent phonon heat conduction in superlattices.,” *Science*, vol. 338, no. 6109, pp. 936–9, Nov. 2012.

[20] Y. Wang, H. Huang, and X. Ruan, “Decomposition of coherent and incoherent phonon conduction in superlattices and random multilayers,” *Phys. Rev. B*, vol. 90, no. 16, p. 165406, Oct. 2014.

[21] Z. Yang, C. Ko, and S. Ramanathan, “Oxide Electronics Utilizing Ultrafast Metal-Insulator Transitions,” *Annu. Rev. Mater. Res.*, vol. 41, no. 1, pp. 337–367, Aug. 2011.

[22] A. L. Pergament, G. B. Stefanovich, and A. A. Velichko, “Oxide Electronics and Vanadium Dioxide Perspective : A Review,” *J. Sel. Top. Nano Electron. Comput.*, vol. 1, no. 1, pp. 24–43, 2013.

[23] E. Freeman, G. Stone, N. Shukla, H. Paik, J. a. Moyer, Z. Cai, H. Wen, R. Engel-Herbert, D. G. Schlom, V. Gopalan, and S. Datta, “Nanoscale structural evolution of electrically driven insulator to metal transition in vanadium dioxide,” *Appl. Phys. Lett.*, vol. 103, no. 26, p. 263109, Dec. 2013.

[24] L. Shi, C. Dames, J. R. Lukes, P. Reddy, J. Duda, D. G. Cahill, J. Lee, A. Marconnet, K. E. Goodson, J.-H. Bahk, A. Shakouri, R. S. Prasher, J. Felts, W. P. King, B. Han, and J. C. Bischof, “Evaluating Broader Impacts of Nanoscale Thermal Transport Research,” *Nanoscale Microscale Thermophys. Eng.*, vol. 19, no. 2, pp. 127–165, 2015.

[25] D. G. Cahill, W. K. Ford, K. E. Goodson, G. D. Mahan, A. Majumdar, H. J. Maris, R.

Merlin, and S. R. Phillpot, “Nanoscale thermal transport,” *J. Appl. Phys.*, vol. 93, no. 2, p. 793, 2003.

[26] D. G. Cahill, P. V Braun, G. Chen, D. R. Clarke, S. Fan, K. E. Goodson, W. P. King, G. D. Mahan, A. Majumdar, H. J. Maris, S. R. Phillpot, E. Pop, P. Keblinski, and L. Shi, “Nanoscale thermal transport . II . 2003 – 2012,” *Appl. Phys. Rev.*, vol. 011305, no. 1, pp. 0–45, 2014.

[27] E. Pop, “Energy dissipation and transport in nanoscale devices,” *Nano Res.*, vol. 3, no. 3, pp. 147–169, 2010.

[28] J. A. Bain, J. A. Malen, M. Jeong, and T. Ganapathy, “Nanoscale thermal transport aspects of heat-assisted magnetic recording devices and materials,” *MRS Bull.*, vol. 43, no. 02, pp. 112–118, 2018.

[29] W. A. Challener, C. Peng, A. V Itagi, D. Karns, W. Peng, Y. Peng, X. Yang, X. Zhu, N. J. Gokemeijer, Y. Hsia, G. Ju, R. E. Rottmayer, M. A. Seigler, and E. C. Gage, “Heat-assisted Magnetic Recording by a near-field transducer with efficient optical energy transfer,” *Nat. Photonics*, vol. 3, no. 4, pp. 220–224, 2009.

[30] G. T. Hohensee, T. Nguyen, E. Pek, W. Kuang, O. Suzer, and M. Finot, “Nanoscale temperature of plasmonic HAMR heads by polymer imprint thermal mapping,” *MRS Adv.*, vol. 2, no. 58–59, p. 3607, 2017.

[31] G. T. Hohensee, D. Kendig, E. Pek, W. Kuang, K. Yazawa, and A. Shakouri, “Calibrated sub-micron temperature mapping of an operating plasmonic HAMR device by thermoreflectance imaging,” *MRS Adv.*, vol. 2, no. 58–59, p. 3613, 2017.

[32] Z. Su, L. Huang, F. Liu, J. P. Freedman, L. M. Porter, R. F. Davis, and J. A. Malen, “Layer-by-layer thermal conductivities of the Group III nitride films in blue/green light emitting diodes,” *Appl. Phys. Lett.*, vol. 100, no. 20, p. 201106, 2012.

[33] M. H. Chang, D. Das, P. V. Varde, and M. Pecht, “Light emitting diodes reliability review,” *Microelectron. Reliab.*, vol. 52, no. 5, pp. 762–782, 2012.

[34] J. Schleeh, J. Mateos, I. Íñiguez-De-La-Torre, N. Wadefalk, P. A. Nilsson, J. Grahn, and A. J. Minnich, “Phonon black-body radiation limit for heat dissipation in electronics,” *Nat. Mater.*, vol. 14, no. 2, pp. 187–192, 2015.

[35] C. D. S. Brites, P. P. Lima, N. J. O. Silva, A. Millán, V. S. Amaral, F. Palacio, and L. D. Carlos, “Thermometry at the nanoscale.,” *Nanoscale*, vol. 4, no. 16, pp. 4799–829, Aug. 2012.

[36] J. Christofferson, K. Maize, Y. Ezzahri, J. Shabani, X. Wang, and A. Shakouri, “Microscale and nanoscale thermal characterization techniques,” *J. Electron. Packag.*, vol. 130, p. 041101, 2008.

[37] Y. Yue and X. Wang, “Nanoscale thermal probing,” *Nano Rev.*, vol. 3, no. 1, p.

11586, 2012.

[38] A. Majumdar, “Scanning thermal microscopy,” *Annu. Rev. Mater. Sci.*, vol. 29, no. 1, pp. 505–85, 1999.

[39] K. Kim, W. Jeong, W. Lee, and P. Reddy, “Ultra-high vacuum scanning thermal microscopy for nanometer resolution quantitative thermometry.,” *ACS Nano*, vol. 6, no. 5, pp. 4248–57, May 2012.

[40] W. Jeong, S. Hur, E. Meyhofer, and P. Reddy, “Scanning Probe Microscopy for Thermal Transport Measurements,” *Nanoscale Microscale Thermophys. Eng.*, vol. 19, no. 4, pp. 279–302, 2015.

[41] J. Varesi and a. Majumdar, “Scanning Joule expansion microscopy at nanometer scales,” *Appl. Phys. Lett.*, vol. 72, no. 1, pp. 37–39, 1998.

[42] A. Vertikov, M. Kuball, A. V. Nurmikko, and H. J. Maris, “Time-resolved pump-probe experiments with subwavelength lateral resolution,” *Appl. Phys. Lett.*, vol. 69, no. 17, pp. 2465–2467, 1996.

[43] K. E. Goodson and M. Asheghi, “Near-field optical thermometry,” *Microscale Thermophys. Eng.*, vol. 1, no. 3, pp. 225–235, 1997.

[44] B. Desiatov, I. Goykhman, and U. Levy, “Direct temperature mapping of nanoscale plasmonic devices,” *Nano Lett.*, vol. 14, no. 2, pp. 648–652, 2014.

[45] Q. Weng, S. Komiyama, L. Yang, Z. Zn, P. Chen, S.-A. Biehs, Y. Kajihara, and W. Lu, “Imaging of nonlocal hot-electron energy dissipation via shot noise,” *Science*, vol. 360, no. May, p. 775, 2018.

[46] D. Halbertal, J. Cuppens, M. Ben Shalom, L. Embon, N. Shadmi, Y. Anahory, H. R. Naren, J. Sarkar, A. Uri, R. Y, Y. Myasoedov, L. S. Levitov, E. Joselevich, A. K. Geim, and E. Zeldov, “Nanoscale thermal imaging of dissipation in quantum systems,” *Nature*, vol. 539, no. 7629, p. 407, 2016.

[47] D. Halbertal, M. Ben Shalom, A. Uri, K. Bagani, A. Y. Meltzer, I. Marcus, Y. Myasoedov, J. Birkbeck, L. S. Levitov, A. K. Geim, and E. Zeldov, “Imaging resonant dissipation from individual atomic defects in graphene,” *Science*, vol. 358, no. 6368, pp. 1303–1306, 2017.

[48] S. Li, K. Zhang, J.-M. Yang, L. Lin, and H. Yang, “Single Quantum Dots as Local Temperature Markers,” *Nano Lett.*, vol. 7, no. 10, pp. 3102–3105, 2007.

[49] T. Plakhotnik and D. Gruber, “Luminescence of nitrogen-vacancy centers in nanodiamonds at temperatures between 300 and 700 K: perspectives on nanothermometry,” *Phys. Chem. Chem. Phys.*, vol. 12, no. 33, p. 9751, 2010.

[50] J. D. Kilbane, E. M. Chan, C. Monachon, N. J. Borys, E. S. Levy, A. D. Pickel, J. J.

Urban, P. J. Schuck, and C. Dames, “Far-field optical nanothermometry using individual sub-50 nm upconverting nanoparticles,” *Nanoscale*, vol. 8, no. 22, pp. 11611–11616, 2016.

[51] M. A. Caldwell, B. Haynor, S. Aloni, D. F. Ogletree, H.-S. P. Wong, J. J. Urban, and D. J. Milliron, “Spectroscopic Evidence for Exceptional Thermal Contribution to Electron Beam-Induced Fragmentation,” *J. Phys. Chem. C*, vol. 114, no. 50, pp. 22064–22068, Dec. 2010.

[52] T. Brintlinger, Y. Qi, K. H. Baloch, D. Goldhaber-Gordon, and J. Cumings, “Electron thermal microscopy.,” *Nano Lett.*, vol. 8, no. 2, pp. 582–5, Feb. 2008.

[53] K. H. Baloch, N. Voskanian, M. Bronsgeest, and J. Cumings, “Remote Joule heating by a carbon nanotube,” *Nat. Nanotechnol.*, vol. 7, no. 5, pp. 316–9, May 2012.

[54] A. Reguer, F. Bedu, S. Nitsche, D. Chaudanson, B. Detailleur, and H. Dallaporta, “Probing the local temperature by in situ electron microscopy on a heated Si(3)N(4) membrane.,” *Ultramicroscopy*, vol. 110, no. 1, pp. 61–6, Dec. 2009.

[55] H. Guo, M. I. Khan, C. Cheng, W. Fan, C. Dames, J. Wu, and A. M. Minor, “Vanadium dioxide nanowire-based microthermometer for quantitative evaluation of electron beam heating,” *Nat Commun*, vol. 5, 2014.

[56] R. K. and M. T. H. Abe, M. Terauchi, “Temperature Dependence of the Volume-Plasmon Energy in Aluminum,” *J. Electron. Mater.*, vol. 41, no. May, pp. 465–468, 1992.

[57] M. Mecklenburg, W. A. Hubbard, E. R. White, R. Dhall, S. B. Cronin, S. Aloni, and B. C. Regan, “Nanoscale temperature mapping in operating microelectronic devices,” *Science*, vol. 347, no. 6222, pp. 629–632, Feb. 2015.

[58] X. Hu, P. Yasaei, J. Jokisaari, S. Öğüt, A. Salehi-Khojin, and R. F. Klie, “Mapping Thermal Expansion Coefficients in Freestanding 2D Materials at the Nanometer Scale,” *Phys. Rev. Lett.*, vol. 120, no. 5, p. 055902, 2018.

[59] M. Mecklenburg, B. Zutter, and B. C. Regan, “Thermometry of Silicon Nanoparticles,” *Phys. Rev. Appl.*, vol. 9, no. 1, p. 14005, 2018.

[60] D. R. Cremons and D. J. Flannigan, “Direct in situ thermometry: Variations in reciprocal-lattice vectors and challenges with the Debye-Waller effect,” *Ultramicroscopy*, vol. 161, pp. 10–16, 2016.

[61] F. Niekiel, S. M. Kraschewski, J. Müller, B. Butz, and E. Spiecker, “Local Temperature Measurement in TEM by Parallel Beam Electron Diffraction,” *Ultramicroscopy*, vol. 176, no. August 2016, pp. 161–169, 2017.

[62] M. Hayashida, K. Cui, M. Malac, and R. Egerton, “Thermal expansion coefficient measurement from electron diffraction of amorphous films in a TEM,”

Ultramicroscopy, vol. 188, pp. 8–12, 2018.

[63] W. Kleinn, “Electron transmission observations of self-supporting thin gold films at high temperatures,” *Thin Solid Films*, vol. 34, pp. 125–129, 1976.

[64] Y. Gao and Y. Bando, “Carbon nanothermometer containing gallium,” *Nature*, vol. 415, no. 6872, p. 599, 2002.

[65] J. C. Idrobo, A. R. Lupini, T. Feng, R. R. Unocic, F. S. Walden, D. S. Gardiner, T. C. Lovejoy, N. Dellby, S. Pantelides, and O. L. Krivanek, “Temperature Measurement by a Nanoscale Electron Probe Using Energy Gain and Loss Spectroscopy,” *Phys. Rev. Lett.*, vol. 120, no. 9, p. 95901, 2018.

[66] C. R. Hall and P. B. Hirsch, “Effect of Thermal Diffuse Scattering on Propagation of High Energy Electrons Through Crystals,” *Proc. R. Soc. A Math. Phys. Eng. Sci.*, vol. 286, no. 1405, pp. 158–177, Jun. 1965.

[67] Z. L. Wang, *Elastic and Inelastic Scattering in Electron Diffraction and Imaging*. Plenum Press, 1995.

[68] A. Takaoka and K. Ura, “Temperature Measurement on Micro-Area of Specimen in TEM by Using Thermal Diffuse Scattering Effect,” *J. Electron Microsc. (Tokyo).*, vol. 70, pp. 69–70, 1990.

[69] A. Takaoka and K. Ura, “Accuracy of temperature measurement in micro-areas of polycrystalline film with transmission electron microscope,” *Meas. Sci. Technol.*, vol. 105, 1994.

[70] Z. L. Wang and A. T. Fisher, “Electron energy-loss spectroscopy of high-angle thermal-diffuse-scattered electrons in TEM,” *Ultramicroscopy*, vol. 48, pp. 183–196, 1993.

[71] N. Kitamura, “Temperature Dependence of Diffuse Streaks in Single-Crystal Silicon Electron-Diffraction Patterns,” *J. Appl. Phys.*, vol. 37, no. 5, p. 2187, 1966.

[72] T. Ohishi, D. Shindo, K. Hiraga, and J. Kudoh, “Evaluation of Thermal Diffuse Electron Scattering in Au with the Imaging Plate,” *Mater. Trans.*, vol. 36, no. 5, pp. 686–688, 1995.

[73] W. Nüchter, a. L. Weickenmeier, and J. Mayer, “High-Precision Measurement of Temperature Factors for NiAl by Convergent-Beam Electron Diffraction,” *Acta Crystallogr. Sect. A Found. Crystallogr.*, vol. 54, no. 2, pp. 147–157, Mar. 1998.

[74] L. He and R. Hull, “Quantification of electron-phonon scattering for determination of temperature variations at high spatial resolution in the transmission electron microscope.,” *Nanotechnology*, vol. 23, no. 20, p. 205705, May 2012.

[75] M. Libera, J. A. Ott, and K. Siangchaew, “Temperature-dependent high-angle

electron scattering from a phase-separated amorphous Ge-Te thin film," *Ultramicroscopy*, vol. 63, no. 2, pp. 81–91, 1996.

[76] T. Mehrtens, M. Schowalter, D. Tytko, P. Choi, D. Raabe, L. Hoffmann, H. Jönen, U. Rossow, a Hangleiter, and a Rosenauer, "Measuring composition in InGaN from HAADF-STEM images and studying the temperature dependence of Z-contrast," *J. Phys. Conf. Ser.*, vol. 471, p. 012009, Nov. 2013.

[77] E. Abe, S. J. Pennycook, and a P. Tsai, "Direct observation of a local thermal vibration anomaly in a quasicrystal.," *Nature*, vol. 421, no. 6921, pp. 347–50, Jan. 2003.

[78] C. Gammer, V. Burak Ozdol, C. H. Liebscher, and A. M. Minor, "Diffraction contrast imaging using virtual apertures," *Ultramicroscopy*, vol. 155, pp. 1–10, 2015.

[79] V. B. Ozdol, C. Gammer, X. G. Jin, P. Ercius, C. Ophus, J. Ciston, and A. M. Minor, "Strain mapping at nanometer resolution using advanced nano-beam electron diffraction," *Appl. Phys. Lett.*, vol. 106, no. 25, 2015.

[80] T. C. Pekin, C. Gammer, J. Ciston, C. Ophus, and A. M. Minor, "In situ nanobeam electron diffraction strain mapping of planar slip in stainless steel," *Scr. Mater.*, vol. 146, pp. 87–90, 2018.

[81] P. Xu, R. F. Loane, and J. Silcox, "Energy-filtered convergent-beam electron diffraction in STEM," *Ultramicroscopy*, vol. 38, pp. 127–133, 1991.

[82] K. L. Chopra, L. C. Bobb, and M. H. Francombe, "Electrical Resistivity of Thin Single-Crystal Gold Films," *J. Appl. Phys.*, vol. 34, no. 6, pp. 1699–1702, 1963.

[83] R. F. Egerton, P. Li, and M. Malac, "Radiation damage in the TEM and SEM," *Micron*, vol. 35, no. 6, pp. 399–409, Jan. 2004.

[84] K. Iakoubovskii, K. Mitsuishi, Y. Nakayama, and K. Furuya, "Mean free path of inelastic electron scattering in elemental solids and oxides using transmission electron microscopy: Atomic number dependent oscillatory behavior," *Phys. Rev. B - Condens. Matter Mater. Phys.*, vol. 77, no. 10, pp. 1–7, 2008.

[85] N. Ashcroft and D. Mermin, *Solid State Physics*. Holt, Rinehart and Winston, 1976, pp. 5–8.

[86] M. D. Croitoru, D. Van Dyck, S. Van Aert, S. Bals, and J. Verbeeck, "An efficient way of including thermal diffuse scattering in simulation of scanning transmission electron microscopic images.," *Ultramicroscopy*, vol. 106, no. 10, pp. 933–40, 2006.

[87] A. V. Crewe, J. Wall, and J. Langmore, "Visibility of Single Atoms," *Science*, vol. 168, no. 3937, pp. 1338–1340, 1970.

[88] S. Hillyard and J. Silcox, “Detector geometry, thermal diffuse scattering and strain effects in ADF STEM imaging,” *Ultramicroscopy*, vol. 58, pp. 6–17, 1995.

[89] S. J. Pennycook and D. E. Jesson, “High-resolution Z-contrast imaging of crystals,” *Ultramicroscopy*, vol. 37, no. 1–4, pp. 14–38, Aug. 1991.

[90] F. P. Incropera, D. P. DeWitt, T. L. Bergman, and A. S. Lavine, *Fundamentals of Heat and Mass Transfer*, 6th ed. John Wiley & Sons, 2007, p. 747.

[91] R. J. Price, “Thermal conductivity of neutron-irradiated pyrolytic beta-silicon carbide,” *J. Nucl. Mater.*, vol. 46, pp. 268–272, 1973.

[92] E. López-Honorato, C. Chiritescu, P. Xiao, D. G. Cahill, G. Marsh, and T. J. Abram, “Thermal conductivity mapping of pyrolytic carbon and silicon carbide coatings on simulated fuel particles by time-domain thermoreflectance,” *J. Nucl. Mater.*, vol. 378, no. 1, pp. 35–39, 2008.

[93] D. G. Cahill, “Thermal Conductivity Measurements from 30 to 750K: the 3-Omega Method,” *Rev. Sci. Instrum.*, vol. 2501, no. September 1989, pp. 802–808, 1990.

[94] A. J. Angstrom, “New method of determining the thermal conductibility of bodies.,” *London, Edinburgh, Dublin Philos. Mag. J. Sci.*, vol. 25, no. 166, pp. 130–142, 1863.

[95] M. Asheghi, Y. K. Leung, S. S. Wong, and K. E. Goodson, “Phonon-boundary scattering in thin silicon layers,” *Appl. Phys. Lett.*, vol. 71, no. September, pp. 1798–1800, 1997.

[96] D. Li, Y. Wu, P. Kim, L. Shi, P. Yang, and A. Majumdar, “Thermal conductivity of individual silicon nanowires,” *Appl. Phys. Lett.*, vol. 83, no. 14, pp. 2934–2936, 2003.

[97] J. Lee, W. Lee, J. Lim, Y. Yu, Q. Kong, J. J. Urban, and P. Yang, “Thermal Transport in Silicon Nanowires at High Temperature up to 700 K,” *Nano Lett.*, vol. 16, no. 7, pp. 4133–4140, 2016.

[98] J. Ravichandran, A. K. Yadav, R. Cheaito, P. B. Rossen, A. Soukiassian, S. J. Suresha, J. C. Duda, B. M. Foley, C.-H. Lee, Y. Zhu, A. W. Lichtenberger, J. E. Moore, D. A. Muller, D. G. Schlom, P. E. Hopkins, A. Majumdar, R. Ramesh, and M. A. Zurbuchen, “Crossover from incoherent to coherent phonon scattering in epitaxial oxide superlattices,” *Nat Mater*, vol. 13, no. 2, pp. 168–172, 2014.

[99] J. Tang, H. T. Wang, D. H. Lee, M. Fardy, Z. Huo, T. P. Russell, and P. Yang, “Holey silicon as an efficient thermoelectric material,” *Nano Lett.*, vol. 10, no. 10, pp. 4279–4283, 2010.

[100] J. Lee, J. Lim, and P. Yang, “Ballistic Phonon Transport in Holey Silicon,” *Nano Lett.*, vol. 15, no. 5, pp. 3273–3279, 2015.

[101] E. Yablonovitch, “Inhibited spontaneous emission in solid-state physics and electronics,” *Phys. Rev. Lett.*, vol. 58, no. 20, pp. 2059–2062, 1987.

[102] J. Ma, J. S. Sadhu, D. Ganta, H. Tian, and S. Sinha, “Thermal transport in 2- and 3-dimensional periodic ‘ holey ’ nanostructures,” *AIP Adv.*, vol. 124502, no. 4, pp. 1–17, 2014.

[103] M. Maldovan, “Sound and heat revolutions in phononics,” *Nature*, vol. 503, no. 7475, pp. 209–217, Nov. 2013.

[104] N. Li, J. Ren, L. Wang, G. Zhang, P. Hänggi, and B. Li, “*Colloquium* : Phononics: Manipulating heat flow with electronic analogs and beyond,” *Rev. Mod. Phys.*, vol. 84, no. 3, pp. 1045–1066, 2012.

[105] A. M. Marconnet, T. Kodama, M. Asheghi, and K. E. Goodson, “Phonon Conduction in Periodically Porous Silicon Nanobridges,” *Nanoscale Microscale Thermophys. Eng.*, vol. 16, no. 4, pp. 199–219, Dec. 2012.

[106] M. Nomura, Y. Kage, D. Muller, D. Moser, and O. Paul, “Electrical and thermal properties of polycrystalline Si thin films with phononic crystal nanopatterning for thermoelectric applications,” *Appl. Phys. Lett.*, vol. 106, no. 22, p. 223106, 2015.

[107] D. Song and G. Chen, “Thermal conductivity of periodic microporous silicon films,” *Appl. Phys. Lett.*, vol. 84, no. 5, p. 687, 2004.

[108] E. Dechaumphai and R. Chen, “Thermal transport in phononic crystals: The role of zone folding effect,” *J. Appl. Phys.*, vol. 111, no. 7, p. 073508, 2012.

[109] A. Jain, Y.-J. Yu, and A. J. H. McGaughey, “Phonon transport in periodic silicon nanoporous films with feature sizes greater than 100 nm,” *Phys. Rev. B*, vol. 87, no. 19, p. 195301, May 2013.

[110] N. K. Ravichandran and A. J. Minnich, “Coherent and incoherent thermal transport in nanomeshes,” *Phys. Rev. B*, vol. 89, no. 20, p. 205432, May 2014.

[111] C. Dames and G. Chen, “Thermal Conductivity of Nanostructured Thermoelectric Materials,” in *Thermoelectrics Handbook Macro to Nano*, vol. 80, no. 10, 2005, p. 1014.

[112] M. Maldovan, “Phonon wave interference and thermal bandgap materials,” *Nat. Mater.*, vol. 14, no. 7, pp. 667–674, 2015.

[113] Y. S. Ju and K. E. Goodson, “Phonon scattering in silicon films with thickness of order 100 nm,” *Appl. Phys. Lett.*, vol. 74, no. 20, p. 3005, 1999.

[114] A. S. Henry and G. Chen, “Spectral Phonon Transport Properties of Silicon Based on Molecular Dynamics Simulations and Lattice Dynamics,” *J. Comput. Theor. Nanosci.*, vol. 5, no. 7, pp. 1193–1204, 2008.

[115] C. Dames and G. Chen, “Theoretical phonon thermal conductivity of Si/Ge superlattice nanowires,” *J. Appl. Phys.*, vol. 95, no. 2, pp. 682–693, 2004.

[116] G. Chen, “Size and Interface Effects on Thermal Conductivity of Superlattices and Periodic Thin-Film Structures,” *J. Heat Transfer*, vol. 119, no. 2, pp. 220–229, 1997.

[117] B. Latour, S. Volz, and Y. Chalopin, “Microscopic description of thermal-phonon coherence: From coherent transport to diffuse interface scattering in superlattices,” *Phys. Rev. B*, vol. 90, no. 1, p. 014307, 2014.

[118] L. Hu, A. J. Schmidt, a. Narayanaswamy, and G. Chen, “Effects of Periodic Structures on the Coherence Properties of Blackbody Radiation,” *J. Heat Transfer*, vol. 126, no. 5, p. 786, 2004.

[119] A. L. Moore, S. K. Saha, R. S. Prasher, and L. Shi, “Phonon backscattering and thermal conductivity suppression in sawtooth nanowires,” *Appl. Phys. Lett.*, vol. 93, no. 8, p. 083112, 2008.

[120] N. Zen, T. a. Puurtinen, T. J. Isotalo, S. Chaudhuri, and I. J. Maasilta, “Engineering thermal conductance using a two-dimensional phononic crystal,” *Nat. Commun.*, vol. 5, p. 3435, Mar. 2014.

[121] F. Kargar, S. Ramirez, B. Debnath, H. Malekpour, R. K. Lake, and A. a. Balandin, “Acoustic phonon spectrum and thermal transport in nanoporous alumina arrays,” *Appl. Phys. Lett.*, vol. 107, no. 17, p. 171904, 2015.

[122] M. Nomura, J. Nakagawa, Y. Kage, J. Maire, D. Moser, and O. Paul, “Thermal phonon transport in silicon nanowires and two-dimensional phononic crystal nanostructures,” *Appl. Phys. Lett.*, vol. 106, no. 14, p. 143102, 2015.

[123] Z. Hashin and S. Shtrikman, “A Variational Approach to the Theory of the Effective Magnetic Permeability of Multiphase Materials,” *J. Appl. Phys.*, vol. 33, no. 10, p. 3125, 1962.

[124] V. Mityushev, “Conductivity of a two-dimensional composite containing elliptical inclusions,” *Proc. R. Soc. A Math. Phys. Eng. Sci.*, vol. 465, no. 2110, pp. 2991–3010, 2009.

[125] N. Mingo, “Calculation of Si nanowire thermal conductivity using complete phonon dispersion relations,” *Phys. Rev. B*, vol. 68, no. 11, p. 113308, Sep. 2003.

[126] C. Dames and G. Chen, “Theoretical phonon thermal conductivity of Si/Ge superlattice nanowires,” *J. Appl. Phys.*, vol. 95, no. 2, p. 682, 2004.

[127] E. Pop, R. W. Dutton, and K. E. Goodson, “Analytic band Monte Carlo model for electron transport in Si including acoustic and optical phonon dispersion,” *J. Appl. Phys.*, vol. 96, no. 9, pp. 4998–5005, 2004.

[128] R. B. Dingle, “The Electrical Conductivity of Thin Wires,” *Proc. R. Soc. A Math. Phys. Eng. Sci.*, vol. 201, no. 1067, pp. 545–560, May 1950.

[129] A. K. McCurdy, H. J. Maris, and C. Elbaum, “Anisotropic Heat Conduction in Cubic Crystals in the Boundary Scattering Regime,” *Phys. Rev. B*, vol. 2, no. 10, pp. 4077–4083, Nov. 1970.

[130] T. Hori, J. Shiomi, and C. Dames, “Effective phonon mean free path in polycrystalline nanostructures,” *Appl. Phys. Lett.*, vol. 106, no. 17, p. 171901, 2015.

[131] C. Jeong, S. Datta, and M. Lundstrom, “Full dispersion versus Debye model evaluation of lattice thermal conductivity with a Landauer approach,” *J. Appl. Phys.*, vol. 109, no. 7, p. 073718, 2011.

[132] S. Datta, *Electronic Transport in Mesoscopic Systems*. Cambridge University Press, 1995.

[133] W. H. Press, S. A. Teukolsky, W. T. Vettering, and B. P. Flannery, *Numerical Recipes in C: The Art of Scientific Computing, Second Edition*. 1992.

[134] M. Modest, *Radiative Heat Transfer*, 1st ed. USA: McGraw-Hill, 1993, pp. 96–98.

[135] J.-S. Heron, C. Bera, T. Fournier, N. Mingo, and O. Bourgeois, “Blocking phonons via nanoscale geometrical design,” *Phys. Rev. B*, vol. 82, no. 15, p. 155458, Oct. 2010.

[136] J. Miller, W. Jang, and C. Dames, “Thermal rectification by ballistic phonons in asymmetric nanostructures,” *Proc. HT2009*, pp. 1–10, 2009.

[137] C. J. Glassbrenner and G. a. Slack, “Thermal conductivity of silicon and germanium from 3K to the melting point,” *Phys. Rev.*, vol. 134, no. 4A, p. 1058, 1964.

[138] J. M. Ziman, *Electrons and Phonons*. Great Britain: Oxford University Press, 1960, pp. 483–523.

[139] A. D. McConnell and K. E. Goodson, “Thermal conduction in silicon micro-and nanostructures,” in *Annual review of heat transfer*, 2005, pp. 129–168.

[140] A. I. Hochbaum, D. Gargas, Y. J. Hwang, and P. Yang, “Single crystalline mesoporous silicon nanowires,” *Nano Lett.*, vol. 9, no. 10, pp. 3550–3554, 2009.

[141] Z. Wei, G. Wehmeyer, C. Dames, and Y. Chen, “Geometric tuning of thermal conductivity in three-dimensional anisotropic phononic crystals,” *Nanoscale*, vol. 8, no. 37, p. 16612, 2016.

[142] K. D. Parrish, J. R. Abel, A. Jain, J. A. Malen, and A. J. H. McGaughey, “Phonon-boundary scattering in nanoporous silicon films: Comparison of Monte Carlo

techniques," *J. Appl. Phys.*, vol. 122, no. 12, 2017.

[143] A. Majumdar, "Microscale Heat Conduction in Dielectric Thin Films," *J. Heat Transfer*, vol. 115, pp. 7–16, 1993.

[144] A. J. Minnich, "Thermal phonon boundary scattering in anisotropic thin films," *Appl. Phys. Lett.*, vol. 107, no. 18, p. 183106, 2015.

[145] B. Vermeersch, J. Carrete, and N. Mingo, "Cross-plane heat conduction in thin films with ab-initio phonon dispersions and scattering rates," *Appl. Phys. Lett.*, vol. 108, p. 193104, 2016.

[146] B. Smith, B. Vermeersch, J. Carrete, E. Ou, J. Kim, N. Mingo, D. Akinwande, and L. Shi, "Temperature and Thickness Dependences of the Anisotropic In-Plane Thermal Conductivity of Black Phosphorus," *Adv. Mater.*, vol. 29, p. 1603756, 2017.

[147] W. Prellier, M. P. Singh, and P. Murugavel, "The single-phase multiferroic oxides : from bulk to thin film," *J. Phys. Condens. Matter*, vol. 17, pp. R803–R832, 2005.

[148] M. Kang, K. Cho, S. Oh, J. Kim, C. Kang, S. Nahm, and S.-J. Yoon, "High-temperature thermoelectric properties of nanostructured Ca 3 Co 4 O 9 thin films," *Appl. Phys. Lett.*, vol. 98, p. 142102, 2011.

[149] D. M. Berg, R. Djemour, L. Gütay, G. Zoppi, S. Siebentritt, and P. J. Dale, "Thin film solar cells based on the ternary compound Cu 2 SnS 3," *Thin Solid Films*, vol. 520, no. 19, pp. 6291–6294, 2012.

[150] D. M. Hausmann and R. G. Gordon, "Surface morphology and crystallinity control in the atomic layer deposition (ALD) of hafnium and zirconium oxide thin films," *J. Cryst. Growth*, vol. 249, pp. 251–261, 2003.

[151] D. Ruzmetov and S. Ramanathan, "Metal-Insulator Transition in Thin Film Vanadium Dioxide," in *Thin Film Metal Oxides*, S. Ramanathan, Ed. Boston, MA: Springer US, 2010, pp. 51–94.

[152] H. Jang, C. R. Ryder, J. D. Wood, M. C. Hersam, and D. G. Cahill, "3D Anisotropic Thermal Conductivity of Exfoliated Rhenium Disulfide," *Adv. Mater.*, vol. 29, p. 1700650, 2017.

[153] M. D. Santia, N. Tandon, and J. D. Albrecht, "Lattice thermal conductivity in β-Ga2O3 from first principles," *Appl. Phys. Lett.*, vol. 107, no. 4, p. 041907, 2015.

[154] Z. Guo, A. Verma, X. Wu, F. Sun, A. Hickman, T. Masui, A. Kuramata, M. Higashiwaki, D. Jena, and T. Luo, "Anisotropic thermal conductivity in single crystal β-gallium oxide," *Appl. Phys. Lett.*, vol. 106, no. 11, p. 111909, 2015.

[155] J. P. Singh and R. K. Bedi, "Tin selenide films grown by hot wall epitaxy," *J. Appl.*

Phys., vol. 68, no. 6, pp. 2776–2779, 1990.

[156] O. Ambacher, "Growth and applications of Group III-nitrides," *J. Phys. D. Appl. Phys.*, vol. 31, pp. 2653–2710, 1998.

[157] F. Scholz, "Semipolar GaN grown on foreign substrates : a review," *Semicond. Sci. Technol.*, vol. 27, p. 024002, 2012.

[158] H. N. Lee, D. Hesse, H. Nyung, and D. Hesse, "Anisotropic ferroelectric properties of epitaxially twinned Ba3.25La0.75Ti3O12 thin films grown with three different orientations," *Appl. Phys. Lett.*, vol. 80, no. 6, p. 1040, 2002.

[159] L. R. Testardi, "Anomalous laser-induced thermoelectricity voltages in YBa , Cu30x and ' off-diagonal ' thermoelectricity," *Appl. Phys. Lett.*, vol. 64, p. 2347, 1994.

[160] D.-W. Oh, C. Ko, S. Ramanathan, and D. G. Cahill, "Thermal conductivity and dynamic heat capacity across the metal-insulator transition in thin film VO2," *Appl. Phys. Lett.*, vol. 96, no. 15, p. 151906, 2010.

[161] X. Yan, B. Poudel, Y. Ma, W. S. Liu, G. Joshi, H. Wang, Y. Lan, D. Wang, G. Chen, and Z. F. Ren, "Experimental studies on anisotropic thermoelectric properties and structures of n-type Bi2Te2.7Se0.3," *Nano Lett.*, vol. 10, no. 9, pp. 3373–3378, 2010.

[162] R. Fei, A. Faghaninia, R. Soklaski, J. A. Yan, C. Lo, and L. Yang, "Enhanced thermoelectric efficiency via orthogonal electrical and thermal conductances in phosphorene," *Nano Lett.*, vol. 14, no. 11, pp. 6393–6399, 2014.

[163] Y. Tang, B. Cui, C. Zhou, and M. Grayson, "p x n -Type Transverse Thermoelectrics : A Novel Type of Thermal Management Material," *J. Electron. Mater.*, vol. 44, no. 6, pp. 2095–2104, 2015.

[164] A. C. Smith, J. F. Janak, and R. V. Adler, *Electronic conduction in solids*. McGraw-Hill, 1967.

[165] M. Buttiker, "Four-Terminal Phase-Coherent Conductance," *Phys. Rev. Lett.*, vol. 57, no. 14, p. 1761, 1986.

[166] C. Liu, W. Chen, Y. Tao, J. Yang, and Y. Chen, "Transient and steady state heat transport in layered materials from molecular dynamics simulation," *Int. J. Heat Mass Transf.*, vol. 121, pp. 72–78, 2018.

[167] C. Hua and A. J. Minnich, "Analytical Green's function of the multidimensional frequency-dependent phonon Boltzmann equation," *Phys. Rev. B*, vol. 90, no. 21, p. 214306, Dec. 2014.

[168] L. D. Landau and E. M. Lifshitz, *Statistical Physics: Vol 1*. Pergamon Press, 1980, p. 427.

[169] Z. Chen, Z. Wei, Y. Chen, and C. Dames, “Anisotropic Debye model for the thermal boundary conductance,” *Phys. Rev. B*, vol. 87, no. 12, p. 125426, 2013.

[170] S. Lee, F. Yang, J. Suh, S. Yang, Y. Lee, G. Li, H. Sung Choe, A. Suslu, Y. Chen, C. Ko, J. Park, K. Liu, J. Li, K. Hippalgaonkar, J. J. Urban, S. Tongay, and J. Wu, “Anisotropic in-plane thermal conductivity of black phosphorus nanoribbons at temperatures higher than 100 K,” *Nat. Commun.*, vol. 6, p. 8573, 2015.

[171] H. Jang, J. D. Wood, C. R. Ryder, M. C. Hersam, and D. G. Cahill, “Anisotropic Thermal Conductivity of Exfoliated Black Phosphorus,” *Adv. Mater.*, vol. 27, no. 48, pp. 8017–8022, 2015.

[172] B. Sun, X. Gu, Q. Zeng, X. Huang, Y. Yan, Z. Liu, R. Yang, and Y. K. Koh, “Temperature Dependence of Anisotropic Thermal-Conductivity Tensor of Bulk Black Phosphorus,” *Adv. Mater.*, vol. 29, no. 3, p. 1603297, 2017.

[173] J. Zhu, H. Park, J. Y. Chen, X. Gu, H. Zhang, S. Karthikeyan, N. Wendel, S. A. Campbell, M. Dawber, X. Du, M. Li, J. P. Wang, R. Yang, and X. Wang, “Revealing the Origins of 3D Anisotropic Thermal Conductivities of Black Phosphorus,” *Adv. Electron. Mater.*, vol. 2, no. 5, p. 1600040, 2016.

[174] A. Jain and A. J. H. McGaughey, “Strongly anisotropic in-plane thermal transport in single-layer black phosphorene,” *Sci. Rep.*, vol. 5, p. 8501, 2015.

[175] H. Yuan, X. Liu, F. Afshinmanesh, W. Li, G. Xu, J. Sun, B. Lian, A. G. Curto, G. Ye, Y. Hikita, Z. Shen, S. C. Zhang, X. Chen, M. Brongersma, H. Y. Hwang, and Y. Cui, “Polarization-sensitive broadband photodetector using a black phosphorus vertical p-n junction,” *Nat. Nanotechnol.*, vol. 10, no. 8, pp. 707–713, 2015.

[176] M. N. Ozisik, *Boundary Value Problems of Heat Conduction*. Courier Corporation, 2013, p. 460.

[177] Y. Chen, C. Chen, R. Kealhofer, H. Liu, Z. Yuan, L. Jiang, J. Suh, J. Park, C. Ko, H. S. Choe, J. Avila, M. Zhong, Z. Wei, J. Li, S. Li, H. Gao, Y. Liu, J. Analytis, Q. Xia, M. C. Asensio, and J. Wu, “Black Arsenic: A Layered Semiconductor with Extreme in-plane Anisotropy,” *Arxiv*, vol. 1805, p. 00418v1, 2018.

[178] J. P. Feser, J. Liu, and D. G. Cahill, “Pump-probe measurements of the thermal conductivity tensor for materials lacking in-plane symmetry.,” *Rev. Sci. Instrum.*, vol. 85, no. 10, p. 104903, Oct. 2014.

[179] V. Mishra, C. L. Hardin, J. E. Garay, and C. Dames, “A 3 omega method to measure an arbitrary anisotropic thermal conductivity tensor,” *Rev. Sci. Instrum.*, vol. 86, no. 5, p. 54902, 2015.

[180] A. T. Ramu and J. E. Bowers, “A ‘2-omega’ technique for measuring anisotropy of thermal conductivity.,” *Rev. Sci. Instrum.*, vol. 83, no. 12, p. 124903, Dec. 2012.

[181] Y. S. Ju, K. Kurabayashi, and K. E. Goodson, “Thermal characterization of anisotropic thin dielectric films using harmonic Joule heating,” *Thin Solid Films*, vol. 339, pp. 160–164, 1999.

[182] A. Cepellotti, G. Fugallo, L. Paulatto, M. Lazzeri, F. Mauri, and N. Marzari, “Phonon hydrodynamics in two-dimensional materials,” *Nat. Commun.*, vol. 6, p. 6400, 2015.

[183] Z. Ding, J. Zhou, B. Song, V. Chiloyan, M. Li, T. H. Liu, and G. Chen, “Phonon Hydrodynamic Heat Conduction and Knudsen Minimum in Graphite,” *Nano Lett.*, vol. 18, no. 1, pp. 638–649, 2018.

[184] T. LaGrange, B. W. Reed, M. K. Santala, J. T. McKeown, A. Kulovits, J. M. K. Wiezorek, L. Nikolova, F. Rosei, B. J. Siwick, and G. H. Campbell, “Approaches for ultrafast imaging of transient materials processes in the transmission electron microscope.,” *Micron*, vol. 43, no. 11, pp. 1108–20, Nov. 2012.

[185] M. T. Hassan, J. S. Baskin, B. Liao, and A. H. Zewail, “High-temporal-resolution electron microscopy for imaging ultrafast electron dynamics,” *Nat. Photonics*, vol. 11, no. 7, pp. 425–430, 2017.

[186] S. Sadasivam, Y. Che, Z. Huang, L. Chen, S. Kumar, T. S. Fisher, and I. B. M. Corporation, “The atomistic Green’s function method for interfacial phonon transport,” *Annu. Rev. Heat Transf.*, pp. 89–145, 2014.